Intelligent Algorithm Based Robust and Fault Tolerant Control of Induction Machines

by

Md. Shamsul Arifin

A thesis submitted to Lakehead University
in partial fulfillment of the requirements for the
Degree of
Doctor of Philosophy in Electrical and Computer Engineering

LAKEHEAD UNIVERSITY
DEPARTMENT OF ELECTRICAL ENGINEERING

2024

Abstract

Induction machines (IMs) are the driving force in industries such as manufacturing, transportation and wind power generation. Hence, it is essential to reliably detect faults in IMs so as to enhance production quality in manufacturing and avoid operational degradation. However, it is still challenging to reliably detect faults in IMs as fault feature properties could change under variable IM operating conditions. The first objective of this thesis is to develop an enhanced empirical mode decomposition (EEMD) technique to detect an IM broken rotor bar (BRB) fault based on motor current signature analysis. In the developed EEMD technique, a phase insensitive similarity function is initially suggested to determine the representative intrinsic mode functions (IMFs). Moreover, an optimized adaptive multi-band filter is suggested to process the current spectrum and to recognize the fault characteristic features. Likewise, a modified whale optimization algorithm (MWOA) is proposed, which is utilized to optimize the parameters in adaptive multi-band filter. Finally, a reference function is recommended to enhance feature properties and IM fault detection. The effectiveness of the proposed EEMD technique is verified through experimental analysis under different IM operating conditions.

Different arrangements of IMs are predominantly used in wind energy conversion (WEC) systems as IMs can easily operate at variable wind speed and can be connected simply with the grid. However, it is challenging to control a healthy IM based WEC system due to wind speed uncertainties and nonlinearity of the IMs as well as WEC system. Among the different configurations of IMs, the doubly fed induction generator (DFIG)-based wind energy conversion (WEC) system is the mostly used configuration due to its decoupled nature of active and reactive power control. Since the traditional DFIG-based WEC systems are controlled using proportional-integral (PI) controllers, they are not always capable of coping with wind uncertainties. The second objective of this work is to propose a new adaptive neuro-fuzzy (ANF)-based direct torque and flux (DTF) control technique for grid-connected DFIG WEC systems. This new control technique has better dynamic responses to handle the uncertainties of the wind speed variation. A training algorithm is also established to adaptively optimize the ANF system parameters to accommodate system nonlinearities and wind speed uncertainties. The proposed ANF-based DTF control technique improves the dynamic performance of the WEC system compared to the conventional PI-based DTF control technique, as verified by simulation and experimental results.

Furthermore, the third objective of the thesis is to develop an integrated neuro-fuzzy (INF)-based DTF control technique for DFIG-based WEC system. Traditionally for DTF control technique, two separate neuro-fuzzy (NF) structures are utilized to control torque and flux independently. In this work, a single INF structure is developed to control torque and flux simultaneously, as these are interdependent through rotor side converter of the DFIG. A new training method based on ensemble algorithm is developed for online training of the proposed INF system parameters. The proposed INF-based DTF control technique is implemented in real time for a prototype DFIG-based WEC system in a laboratory environment using DSP board DS1104. The efficacy of the proposed INF-based DTF control technique, incorporated with the ensemble training method, is investigated and compared with the classical NF network and training method. The proposed INF-based DTF control technique improves the dynamic performance of the WEC system compared to the conventional NF-based DTF control technique . Furthermore, the INF network has less computational burden and adaptive capability compared to its counterpart. The stability of the proposed INF-based DTF control technique is also analyzed under variable wind speed conditions. The WEC system with the proposed INF-based DTF control technique is found to be stable under dynamic conditions.

The squirrel cage induction machine (SCIM) is also utilized sometimes as wind generator besides DFIG as well as used largely in industrial applications. However, different from DFIG, the BRB fault may occur in SCIM which may affect the operating performance of the machine. The broken rotor bars can cause current and torque fluctuation of IM which can adversely affect the operational condition of the machine. Hence, the fourth objective of the thesis is to develop a NF based fault tolerant control technique, which can reduce the torque ripple at the time of broken rotor bar fault of IM and improve the operational performance. The effectiveness of the proposed FTC technique is also investigated in this thesis.

Acknowledgements

At first, I want to thank the Almighty, the most merciful, the most gracious for giving me the opportunity to conduct the PhD research in Lakehead University, ON, Canada. After that, I would like to express my sincere gratitude to my supervisors, Dr. Mohammad Nasir Uddin and Dr. Wilson Wang, for their outstanding guidance, motivation, support and constant supervision. I think I am fortunate to have the best supervision from both of my supervisors considering their endless support, friendly behavior, and an exceptional way to make me realize my latent research talents. I am enthusiastically thankful for their remarkable efforts to provide financial support for my research studies.

I would like to express my gratitude and thanks towards Dr. Amir Ameli, from the Department of Electrical Engineering, Lakehead University and Dr. Hao Bai from the Department of Mechanical Engineering, Lakehead University and Dr. S. A. Saleh from the Department of Electrical and Computer Engineering, University of New Brunswick for being in my thesis committee and give their valuable time to review my thesis and give beneficial opinions. I would like to thank Dr. Salama Ikki, Department of Electrical Engineering, Lakehead University for his support. My thanks and appreciations also go to my colleagues Dr. Nima, Dr. Manzar, Dr. Yazdan, Mr. Liaq and others for their help and support.

Last but not least, I will be forever grateful to my family back in Bangladesh, my parents, A. N. M. Emdadul Huque and Hosna Ara Begum for their kindness, countless prayer for me and encouragement. I must say without any hesitation that my research would never have been in this shape without encouragement and constant support from my mother. Their strong belief and faith have always helped me to be positive in difficult times. I pray that may Almighty Allah swt. grant His mercy on my parents in this world and the hereafter, grant them Jannatul Firdaus and accept them among the people that are close to Him.

Table of Contents

List of Figures

List of Tables

List of Acronyms

ANF	Adaptive Neuro Fuzzy
BRB	Broken rotor bar
DFIG	Doubly fed induction generator
DTF	Direct torque and flix
EMD	Empirical mode decomposition
EEMD	Enhanced empirical mode decomposition
FTC	Fault tolerant control
GD	Gradient decent
IM	Induction machine
IMF	Intrinsic mode function
INF	Integrated neuro fuzzy
LSE	Least square error
MCSA	Motor current signature analysis
MF	Membership function
MWO	Modified whale optimization
NF	Neuro fuzzy
OAMF	Optimized adaptive multiband filter
PMSG	Permanent magnet induction generator

RMSE	Root mean square error
RSC	Rotor side converter
SNR	Signal-to-noise ratio
VMD	Variational mode decomposition technique
WEC	Wind energy conversion
WO	Whale optimization
WRIG	Wound rotor induction generator
WRSG	Wound rotor synchronous generator

List of Nomenclature

A	Swept area of the air flow
c_f	Novel chaotic function
C_p	Power coefficient of the WEC system
C_{wz}	Cross-correlation coefficient
$D_{ck\pm}$	Datasets contain the obtained characteristic frequencies
e_t, e_ψ	Torque and flux errors
Δe_t, Δe_ψ	Change rates of torque and flux errors
$f_{ck\pm}$	Characteristic side band frequency for the BRB fault of IM
Δf_{ck}	Bandwidth of the adaptive window
$f_{ck\pm\_U}$ and $f_{ck\pm\_L}$	Upper and lower range of sideband frequencies
f_l	Line frequency
F_P	Post-processing function
f_s	Frequency of the stator
G_r	Gearbox conversion ratio or gear ratio
i_{ds}, i_{qs}	*D*-*q*- axis comments of $\bar{\iota}_s$
i_{dr}, i_{qr}	*D*-*q*- axis comments of $\bar{\iota}_r$
i_m	Magnetizing current
$\bar{\iota}_s$, $\bar{\iota}_r$	Current vectors for stator and rotor

i_s and i_r	Stator and rotor side current
I_{s_0}	Current component of fundamental frequency
I_{s_ripple}	Current component that introduces ripples
L_{ls}, L_{lr}	Leakage inductances of stator and rotor (H)
L_m	Mutual inductance (H)
L_r	Self-inductance of the rotor (H)
L_s	Self-inductance of the stator
n_g	Generator rated speed
n_r	Rotor speed of IM
n_t	Turbine rated speed
p	Derivative operator
P	Number of pole pairs of the machine
P_m	Mechanical power of the WEC system
R	Radius of the blades
R_r and X_r	Rotor side resistance and reactance
R_s and X_s	Stator side resistance and reactance
s	Slip of the IM
S_F	Similarity function
S_{F-u}	Similarity of IMF_u with the benchmark signature

T_{em}	Torque of the WEC system
$T(s)$	Transfer function
v_{sa}, v_{sb}, v_{sc}	Phase voltages for stator (V)
v_{dr}, v_{qr}	D-q- axis comments of $\bar{v}_r$
v_{ds}, v_{qs}	D-q axis comments of $\bar{v}_s$
v_s and v_r	Stator and rotor side phase voltages
$\bar{v}_s, \bar{v}_r$	Voltage vectors for stator and rotor
v_w	Velocity of the wind
$W_{ck\pm}$	Adaptive windowing functions
X_m	Magnetizing reactance (Ω)
ρ	Air density
λ	Tip speed ration
β	Pitch angle
ω	Angular speed of the generator rotor
$\bar{\psi}_s, \bar{\psi}_r$	Flux-linkage vectors for stator and rotor
ω_r	Electrical angular speed for the rotor
ψ_{ds}, ψ_{qs}	D-q- axis comments of $\bar{\psi}_s$
ψ_{dr}, ψ_{qr}	D-q- axis comments of $\bar{\psi}_r$
$\psi_{s\alpha}$, $\psi_{s\beta}$	α-β Components of the stator flux

ζ	Damping ratio of the second order underdamped system percent
ω_n	Natural frequency of the second order underdamped system
$\%OS$	Overshoot
ω_c	Crossover frequency
$\emptyset$	Phase of the system

Chapter 1

Introduction

This chapter presents an overview of research work, a literature review related to the fault detection and control of induction machine (IM), as well as the objectives and organization of this research work.

1.1 Overview

Induction machines (IMs) play a significant role in industrial applications as well as wind energy conversion (WEC) systems, due to their specific properties such as robustness, simpler construction, easier control, and inexpensive operational costs. However, IM efficiency will degrade due to defects in IM mechanical or electrical systems. IM faults may occur due to the effects of electrical, thermal, and/or mechanical stresses. Common IM faults include broken rotor bars (BRB) defect, stator winding defects, bearing faults, unbalanced supply imperfections, etc. Reliable IM fault diagnosis is essential to avoid interruptions of continuous operation of the IM and to reduce maintenance costs. When BRB fault occurs in an IM, the faulty rotor bar may lead to damage of several rotor bars gradually because they have to carry more rotor current. Therefore, the fault propagation may cause serious torque fluctuations and extra vibration if the defect is not detected in time. However, it remains a challenging task to detect the IM fault reliably as the feature characteristic frequencies of a faulty IM change with IM operating conditions in terms of loading and speed. The classical approaches are not always reliable and accurate to detect the BRB faults [1-2]. Therefore, in this thesis firstly the IM BRB fault detection technique will be developed.

In WEC systems, IMs have been widely utilized as wind generators due to several advantages over synchronous machines such as more flexibility to operate at variable wind speed, simpler to integrate with the grid, easier operation and control. Among different types of IMs, the doubly fed induction generator (DFIG) is the most common configuration for grid connected WEC systems. However, the control of healthy IM based WEC system faces some challenges such as coping with wind speed uncertainties and nonlinearity of the IMs as well as WEC system. Consequently, this research focus on developing robust control techniques for healthy IMs based WEC system. The DFIG-based WEC system is more efficient and cost effective [3-4], because it allows decoupled system control and makes the control scheme more straightforward [5]. Furthermore, a DFIG-based WEC system can be controlled in both sub-synchronous and super synchronous modes of operation, which can facilitate its grid connection. Thus, this research focuses on developing a more robust control technique for the DFIG based WEC systems to limit the transient effects and to improve the dynamic response of WEC systems so as to cope with the wind speed uncertainties.

Besides DFIG, sometimes squirrel cage induction machine (SCIM) is also utilized as wind generator. Unlike DFIG, the SCIM suffers from BRB fault which may severely affects the operating performance of WEC system. When BRB defect occurs in an SCIM, the damaged rotor bars cannot carry rotor current, which causes an asymmetry in magnetic flux distribution of the IM [6]. Consequently, severe torque fluctuations can occur, which will cause IM performance degradation and possible mechanical damage of the machines resulting poor performance in WEC systems as well as industrial drive applications. So, it is important for the controller to cope with the torque fluctuations to some extent before proper repairs and maintenance are undertaken. Therefore, another aspect of this work is to develop a fault tolerant control (FTC) technique for SCIMs to compensate the IM performance degradation when BRB fault occurs.

1.2 Literature Review

Literature review related to the proposed three research themes will be summarized in this section.

1.2.1 Techniques for BRB Fault Detection of IMs

IMs are widely used in WEC systems to produce electric energy. Like other rotating machines, faults may occur in the Ims, which will affect adversely the operation of WEC systems. Common IM faults include BRB defects, stator winding defects, bearing faults, and unbalanced supply imperfections, etc. Fig. 1.2 outlines the distribution of different types of faults in IMs. Approximately 10% IM defects are associated with BRB faults [7]. However, the effect of BRB fault is more severe in comparison with other faults in IMs. For example, an initial BRB defect may lead to gradual damage of several adjacent rotor bars, as they that have to carry more rotor current, which may result in excessive torque fluctuations, vibration, and even sparks [1]. The propagation of BRB fault may interrupt the normal operation of IMs and cause degradation of power quality of the WEC system as discussed in previous section. Hence, it is essential to detect the BRB fault of the IM in WEC system at its earliest stage, so as to avoid operation degradation and to reduce extra maintenance costs [6]. However, it is usually challenging to detect the IM fault accurately, as BRB features could change with IM operating conditions in terms of load and speed [2, 6-8]. Therefore, this work will focus on RBR fault detection of IMs (Objective 1).

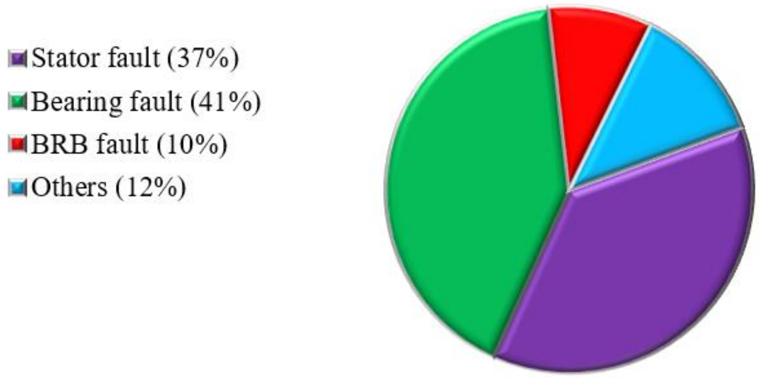

Fig. 1.1 Statistical distribution of IM faults [7].

Several signal processing techniques have been suggested in the literature to extract representative features for IM BRB fault detection. The analysis could be based on different types of information carriers such as voltage, vibration and current. The motor current signature analysis (MCSA) is a commonly used approach for detecting BRB faults due to the ease of measurement and relatively high signal-to-noise ratio [9], which will also be used in this work.

Spectrum analysis is a traditional method of detecting BRB faults [10]. In general, spectral analysis is used mainly for processing time-invariant signals. The FFT is mainly used for spectral analysis of stationary signals; however, signatures from most faulty IMs could be time-varying in nature [11]. For example, the analysis in [12] shows that the sideband frequencies are not detectable using classical FFT at no-load condition of IM having BRB faults. The time-frequency domain techniques could be used for time-varying signal analysis, such as different types of wavelet transforms [2], [13-15]. For example (a Daubechies-27 wavelet) is applied in [16] to detect BRB faults; but the effect of loading on BRB diagnostic accuracy is not discussed properly in this paper. However, it is challenging to use the wavelet amplitude decomposition for IM fault detection as it is difficult to explain its phase map information [11].

Some researchers have used the empirical mode decomposition (EMD) approach to detect BRB faults. The EMD method can extract the representative features by decomposing the frequency components into different intrinsic mode functions (IMFs) [1, 8]. This method can adaptively modify the IMFs based on signal properties in the time domain to analyze time varying signals. For example, an EMD technique is suggested in [1, 17] for BRB fault detection based on correlation analysis. However, the presented method in [17] uses only one characteristic frequency to detect the BRB fault, which can be sensitive to noise in the current signal.

A normalized frequency-domain energy operator algorithm is suggested in [18] to detect IM fault based on current signal analysis. A Walsh–Hadamard transform is used in [19] to extract representative features for BRB and bearing fault detection. In [20], a Dragon transform method is employed to improve BRB fault detection accuracy; however, its effectiveness is not fully tested over different IM BRB conditions.

Several other signal processing techniques are also introduced in the literature to detect IM faults [19-23]. For example, the time synchronous averaging method is applied to detect and analyze the eccentricity of IM faults in [21]; however, the effectiveness of that method is not studied in comparison with the existing methods in fault detection. A short-time adaptive window technique is proposed in [22] to detect the BRB fault of an inverter connected IM under the speed varying conditions. A modified Bayesian learning algorithm is proposed in [23] to recognize the weak sidebands of the rotor current signal for BRB fault diagnosis. On the other hand, many researchers have also incorporated machine learning for IM fault diagnosis [24-30]. However, it could be difficult to track processing errors due to the use of supervised machine learning and several signal processing techniques. In addition, phaselet-based analysis have also been used in BRB fault detection [31, 32]. For example, a phaselet processing technique is applied in [31] to estimate the trip signals to predict BRB faults of IMs. However, this study lacks systematic investigation of BRB fault severity diagnosis. To tackle the aforementioned problems in IM BRB fault detection, the second objective of this research is to propose an enhanced EMD (EEMD) technique to recognize representative features from current signals for IM fault detection, specifically for BRB fault detection. This work focuses only on signal processing-based IM BRB fault detection.

One of the approaches to improve diagnostic accuracy is to increase signal-to-noise ratio. Several frequency domain techniques are presented in the literature for noise reduction from different types of signals [33-37]. For example, a frequency domain averaging method is presented in [33] to detect IM faults from noisy signals. A synchronous averaging processing method is suggested in [34] to predict IM faults. A nonlinear adaptive method is proposed in [35] to suppress noise from electrocardiogram signals. An activation function dynamic averaging method is suggested in [37] to reduce noise from acoustic signals. However, very limited research has paid attention to MCSA processing to detect BRB faults in noisy environments [38].

Several optimization algorithms have been applied in signal processing to improve the performance of fault detection in IMs. Among these metaheuristic optimization algorithms, swarm intelligence-based optimization techniques are becoming popular due to their flexibility, simplicity of application and consistency. For example, the whale optimization (WO) algorithm is proposed in [39], which is consistent to optimize different benchmark functions and real time problems; it has simpler operations compared to some traditional algorithms such as grey-wolf optimization (GWO) and particle swarm optimization (PSO). Furthermore, several WO variations have been proposed in the literature to improve population diversity and convergence, for example, a Levy flight-based WO [40], and a dynamic learning-based WO [41]. Additionally, chaotic functions can be used to improve population diversity of the related WO algorithms [42] using a classical skew tent chaotic function. However, WO algorithm suffers from poor searching for global optima [39]. Consequently, another research topic is to propose a modified WO (MWO) algorithm to improve the global search capability.

1.2.2 Control Technique for DFIG Based WEC system

Among different sources of renewable energy, the WEC systems are more cost-effective and operation efficient [43-54]. Fig. 1.2 shows the annual power generation of wind and solar energy in Canada over the past two decades. It is evident that there is a huge potential of wind generation compared to solar power due to Canada’s weather conditions.

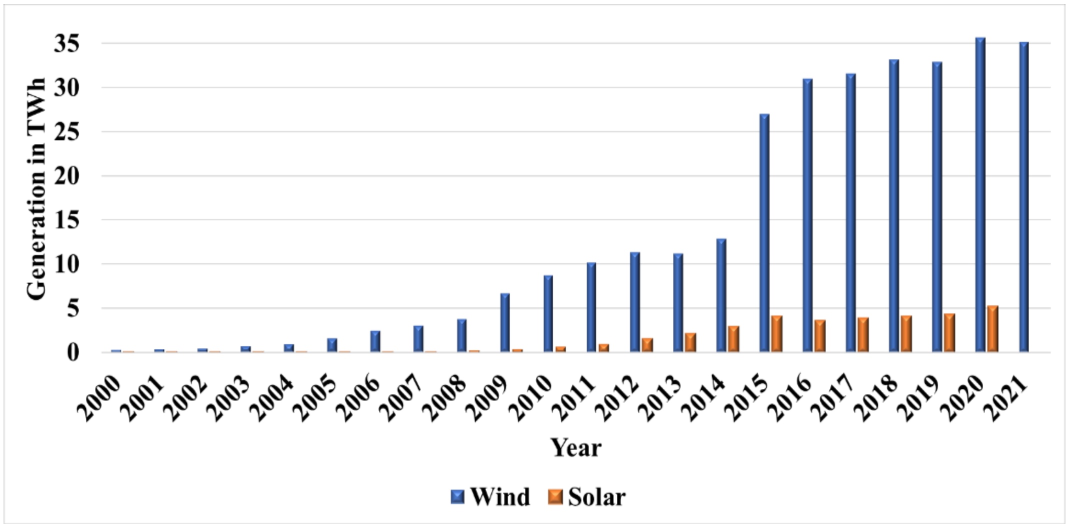

Fig. 1.2 Annual power generation of wind and solar energy in Canada [55]

As discussed in Section 1.1 the DFIG-based WEC system is the most popular way to generate electricity from wind energy among various configurations like synchronous generators or squirrel cage induction generators. In a DFIG-based WEC system the stator side of the DFIG is connected directly to the grid and the rotor side is connected to the grid using a back-to-back converter. The DFIG allows bidirectional power flow between the grid and the WEC system through a back-to-back rotor side converter. It also allows decouple control actions to manage large scale grid connected WEC systems [51]. In addition, DFIG configuration is usually more reliable as it is less dependent on power electronic equipment [51]. Different control strategies have been adopted to control the converter at the rotor side of the DFIG-based WEC system, such as field-oriented control, direct torque and flux (DTF) control technique, direct power control, and voltage-oriented control [47, 56-59]. Among them, the DTF control technique has the advantages such as less switching loss, faster dynamic response, and more robust behavior at the time of grid side fault. However, DTF control technique has some limitations such as high torque ripples and poor performance at a lower rotor speed of the WEC system [59]. The DTF control technique is usually used to manipulate the torque and flux of the DFIG by applying either a hysteresis or proportional-integral (PI) control for the rotor side converter (RSC). However, these classical hysteresis or PI based DTF control techniques are not appropriate for controlling the DFIG-based WEC system due to the system nonlinearity and wind uncertainty [59, 60].

Several researches have been conducted on reducing torque ripples, simplifying control implementation, and improving DTF control efficiency [61-69]. For example, a DTF control method is suggested in [61] based on model prediction to minimize torque ripples of the machine. Several studies have been conducted using the DTF control technique to predict the duty ratio of switching pulses considering torque and flux errors [62, 63]. However, they require extra electronic devices to control the duty ratio of a switching signal, which will also limit their real time applications. On the other hand, virtual voltage vector-based DTF control technique is adapted in [64-66] to minimize the torque ripples and improve the IM efficiency, in which multiple hysteresis bands are applied and a look up table is used to predict the possible configuration of the switches. However, the virtual vector will change the on-off configuration of the switches more frequently than the classical DTF control techniques, which will increase both the switching losses and stresses across the switch. A DTF control technique is designed in [67] using a single PI controller to determine the reference. But this study does not conduct fine tuning of the PI controller so as to improve the estimation of the reference. A deadbeat torque controller is presented in [68], which can run faster than the conventional DTF control techniques. However, this method requires past operational data, which may not always be available.

In addition, some advanced techniques are presented to control the DFIG based WEC systems [70-72]. For example, an analytical model predictive control technique is presented in [70] for controlling DFIG-based WEC systems considering grid side harmonics related non-ideal situation. However, such a model predictive control technique uses high complex algorithms and takes longer computation time, which may limit its real-time applications [73].

With the rapid advancement of soft computing technology, different intelligent tools such as fuzzy and neuro-fuzzy (NF) techniques, have been used for intelligent control of WEC systems [74-85]. For example, a NF technique is used in [75, 77] for robust control considering grid disturbance and wind speed variations. A fuzzy control system is designed in [79] to produce virtual voltage vectors in order to improve the space vector modulation switching for IM drives. Likewise, two fuzzy controllers, along with hysteresis control mechanism of DTF control technique, are designed in [81] to enhance the system performance by reducing torque and flux ripples. The fuzzy controllers are also applied to manipulate the standalone DFIG systems, using energy storage devices rather than supplying power directly to the power grid [85]. However, the parameters of these fuzzy systems are determined based on expertise and could not be adjusted to accommodate for different system conditions.

From the above literature review and analysis, it is evident that very few studies have been undertaken on the analysis and improvement of the dynamic performance of DTF control for DFIG-based WEC systems. Hence, one of the objectives of this work is to develop a new adaptive neuro fuzzy (ANF) technique for reducing the transient effects and improving the dynamic performance of WEC systems. Furthermore, an integrated neuro-fuzzy (INF) DTF control technique will be developed for the RSC of DFIG-based WEC systems. The proposed INF DTF control technique will process the torque and flux errors, as well as their changes to generate *d-q* axis control voltages from a single NF control. A new ensemble training method will be suggested to update the INF system parameters.

1.2.3 Techniques for Fault Tolerant Control of IMs

Several studies have been performed in literature to accommodate the adverse effect of IM faults in WEC systems [86-92]. For example, an FTC strategy is proposed in [90] to rearrange the converter configuration when the converter is faulty. However, such a reconfiguration may derate the converter, which is unexpected as it should run at rated conditions. A power switch open-circuit fault is considered in [91], and an FTC method is proposed to minimize hardware requirements at the time of fault; additionally, a vector control strategy is proposed to balance the capacitor voltage of the converter and minimize the torque ripples. A direct power control along with the FTC is presented in [92] to accommodate for power switch fault; however, extra converters are required to implement this control system, which increases the cost and complexity of the system.

Several papers have been published in literature on FTC corresponding to sensor defects and actuator faults [91-98]. For example, a FTC method is proposed in [93] against yaw drive system of WEC system, which is tested using online data sets from the U.S. National Renewable Energy Laboratory's National Wind Turbine Center, instead of using data from a real system. A strategy combining the model predictive control with a fuzzy system is proposed in [94] against actuator faults. In [95] an FTC is developed for WEC systems, to handle multiple current sensor faults in the stator and rotor side of the IM. A model reference adaptive fuzzy control is presented in [96], which adjusts the reference torque corresponding to an actuator fault.

Very few research has been undertaken in the literature to design FTC techniques considering the faults inside an IM. For example, a model predictive control is presented in [97] to tackle the stator inter-turn fault of the generator considering flux modulations. However, this approach requires very accurate flux modulation, which can not only increase the cost but also affect the control speed. IM faults, such as BRB defects, will degrade IM performance and efficiency as discussed earlier. However, there are no efficient methods that can be used to design the FTC control systems of an IM with BRB defect. Hence, another objective this work focus on the development of an intelligent FTC technique to cope with the adverse effect of BRB fault of an IM.

1.3 Proposed Objectives

From the discussions and analysis in the previous section, the goal of this PhD dissertation is to develop new techniques and intelligent tools to improve the performance of IMs. Specific research objectives of this thesis are outlined below:

1) An enhanced EMD (EEMD) technique will be proposed to provide a more reliable fault detection of IM BRB. A new similarity function will be suggested to compare IMFs with the benchmark signature to select the most representative IMFs for advanced analysis. The proposed similarity function is phase-insensitive and independent of the starting time of acquiring the machine current signal. An optimized adaptive multiband filter (OAMF) technique will be suggested to recognize the sidebands of the characteristic frequency of the selected IMFs. An adaptive window function will be applied to provide optimized accentuation in the MCSA's sidebands without reconstructing the original time domain signal. A new MWO technique will be proposed to enhance global search capability. Finally, a new post-processing method is proposed to enhance representative features for the BRB fault detection. The EEMD technique will be more effective to predict the severity of BRB faults for IM condition monitoring.

2) An ANF-based DTF control technique will be proposed to control the RSC of DFIG-WEC system. This proposed technique can improve the dynamic performance of WEC system by improving the torque and stator current overshoot, as well as the settling time for DFIG-WEC system. Additionally, this control technique can limit the transient peak of the torque and stator current at the initial starting period. Hence, in incorporating the grid, the proposed ANF-based

DTF control technique will cope with the wind speed variations and high starting transient quantities of DFIG.

3) ANF-based DTF control technique described in previous objective will use several ANF networks to process the torque and flux errors; hence requires more computational steps in processing. Therefore, an INF-based DTF control technique will be suggested to control the RSC of DFIG-based WEC system. The proposed INF-based DTF control technique utilizes an INF approach to process the torque and flux errors, and to generate the control signals for RSC. A new ensemble training method is proposed to train the INF system parameters. The proposed INF network should be more computationally efficient in processing for real-world applications. Therefore, the proposed INF-based DTF control technique can improve dynamic and starting performance of DFIG with better computational efficiency compared to the conventional techniques.

4) A NF based fault-tolerant control (FTC) technique will be presented to accommodate the BRB fault in IM by reducing the torque ripple at the time of fault. The current and torque of healthy and faulty IM will be analyzed considering the real time data. Furthermore, the operation of the proposed NF based FTC approach, and the NF structure will be discussed. Finally, the effectiveness of the FTC technique will be verified through simulation tests. Consequently, the proposed FTC will compensate for the possible degradation of performance of a faulty IM.

1.4 Thesis Organization

The remainder of this thesis is organized as follows:

Chapter 2 describes a comprehensive overview of the WEC system and the IMs, including the types of WEC system, dynamic models of the DFIG, the IM theories, and BRB fault.

Chapter 3 discusses the proposed EEMD technique for BRB fault detection in IMs. Its effectiveness is examined by simulation and experimental tests.

Chapter 4 presents the developed adaptive DTF control technique, including the related NF system and stability analysis. Its effectiveness is examined by experimental tests.

Chapter 5 represents the developed INF-based DTF control technique, including the INF network architecture, ensemble training technique related the INF system, and stability analysis. Its effectiveness is examined by experimental tests.

Chapter 6 discusses the operation of the proposed NF based FTC technique. The effectiveness of the proposed control technique is verified through simulation tests.

Chapter 7 summarizes concluding remarks from this research and future research topics.

Chapter 2

Modelling of WEC System and IMs

This chapter outlines the structure, operation, mathematical analysis, configurations and control of the WEC system. Furthermore, different IM structures and fault conditions are also discussed in this chapter.

2.1 Classification of WEC System

The WEC system can be classified in different ways based on their structure, operational conditions as well as applications. However, the WEVS can be primarily classified based on the axis of aerodynamic lift as well as speed of operations. The detail classifications are discussed in the subsections below.

2.1.1 Horizontal-Axis and Vertical-Axis WEC System

The WEC system can be categorized into two types based on the axis of aerodynamic lift: vertical-axis and horizontal-axis [101]. In a horizontal-axis WEC system, the orientation of the rotational axis is horizontal, or parallel to the ground as illustrated in Fig. 2.1(a). The tower has a threshold height and is required to elevate the nacelle to provide sufficient space for the rotor blade rotation and to reach stronger wind conditions. On the contrary, the rotational axis of a vertical-axis wind turbine is perpendicular to the ground as illustrated in Fig. 2.1(b). The curved vertically mounted airfoils are employed to capture wind energy in this type of WEC system. The generator and gearbox are usually placed in the base of the turbine on the ground, as illustrated in Fig. 2.1(b). The vertical-axis wind turbines usually have different blade structures.

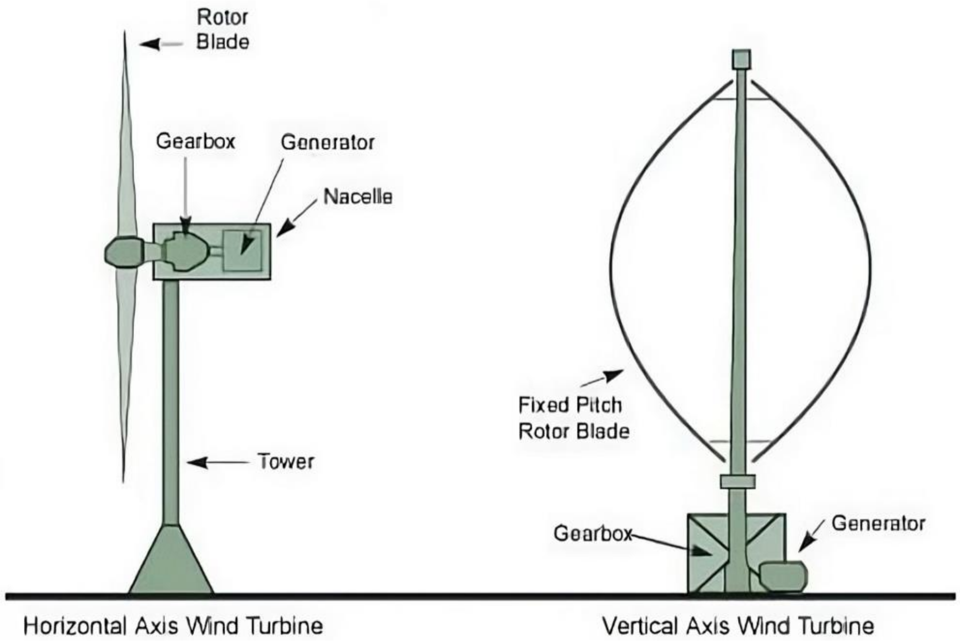

(a) (b)

Fig 2.1 Horizontal-axis and vertical-axis WEC system [102]: (a) horizontal-axis (b) vertical-axis

2.1.2 Fixed-speed and Variable-speed WEC System

The WEC system can be classified as either fixed-speed or variable-speed [102]. In a fixed-speed WEC system, the rotor speed is almost fixed regardless of the wind speed. The rotor speed can be fixed by considering the number of factors such as the gear ratio of the gearbox, the supply frequency of the grid, and the pole number of the generator. Although the fixed-speed WEC system is simpler in construction and operation, it is not suitable for large power turbines as there is no option of controlling reactive power in fixed-speed WEC system. Additionally, the fixed-speed configuration has high mechanical stress and limited power generation control; thus, the fixed-speed turbine generates highly fluctuating output power, which is not suitable for large grid integration. On the other hand, a variable-speed WEC system provides flexibility to obtain maximum aerodynamic efficiency over an operational range of wind speed. Its rotor speed can be adjusted in accordance with the wind speed. For this operation, the tip-speed ratio or the ratio of the blade tip speed and the wind speed is kept fixed at an optimal value that is related to the maximum power coefficient. Variable-speed WEC system systems have low mechanical stress, better power quality, and improved wind energy output. Consequently, they are suitable for high power application as well as grid connected operation. However, this type of WEC system generates extra power loss in power electronics devices and is more expensive in manufacturing costs because of applying power electronics devices [103]. For the research work described in the PhD dissertation the DFIG based WEC system is selected which also allows rotor speed variation as this research focus on grid connected high power WEC system. The detail of the selection criteria has been discussed in subsection 1.1 of Chapter 1.

2.2 Structure of WEC System

The application of wind energy started about 3000 years ago to lift water and to grind crops. Those primary systems can be considered as the initial WEC system, which had vertical-axis structure and ran on the drag principle to drive a wheel [103]. However, those WEC system systems had very low efficiency and were not suitable to produce electricity. In modern ages, the main objective of the WEC system is to effectively produce electricity from wind power. The current models of WEC system incorporate different modern equipment such as aerofoils to produce aerodynamic lift from incoming wind flows. The lift force acts in the perpendicular direction of the air flow and generates driving torque for the rotor coupled with the generator of the WEC system. Although WEC system can be in horizontal-axis and vertical-axis modes as discussed earlier, horizontal-axis WEC system is more commonly used to produce electricity, especially in commercial wind farms. The structure and operation of different components of a horizontal-axis WEC system is illustrated in Fig. 2.2.

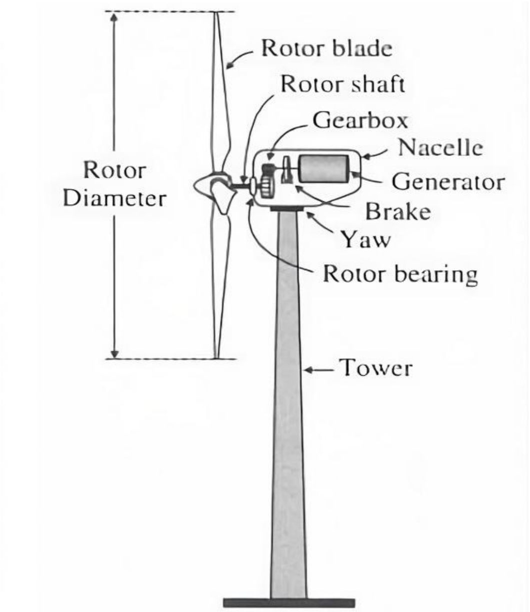

Fig 2.2 Structure and components of a typical horizontal-axis WEC system [104]

A typical horizontal-axis WEC system consists of different components such as aerodynamic blades, nacelle, gearbox, coupling and mechanical brake, yaw drive, sensors, power electronic converters, and generator. The components are described briefly in the following subsections:

2.2.1 Blades

The aerodynamic blades are the most distinctive and visible part of a WEC system, which are deployed to transform wind kinetic energy into rotational mechanical energy in a WEC system. Blades have an aerodynamic structural design and are generally made of aluminum, fiberglass, or carbon-fiber composites, which are high in weight but can still provide sufficient strength-to-weight ratio.

The rotor incorporating two-four blades is extensively used in large wind farms; however, one-bladed WEC system is not frequently used in industrial wind turbines as the single blade can cause asymmetrical mechanical load and aerodynamically unbalance. Turbines having fewer blades are cheaper in structure, but the blades generate less power to drive the turbines. They require a higher rotor speed in operation but a lower gear ratio for gearboxes (cheaper). In contrary, rotors using more blades are more expensive in structure, but the blades generate more drive torques to the turbines; and require gearboxes with a higher gear ratio (more expensive) since the speed of operation is lower compared to the WEC system with fewer blades. Therefore, the three-blade rotors are most used for industrial wind farms due to their best trade-off among mechanical vibrations, acoustic noise, cost, and rotational speed [102], which will be also considered in this work.

2.2.2 Tower and Foundation

The tower is a concrete or steel structure of a tubular or cylindrical shape. The tower and the foundation require should be designed and fabricated properly to support the weight of the nacelle and the rotor blades, as well as the mechanical turbulence associated with wind and the blades in converting wind energy to electricity.

2.2.3 Nacelle

The nacelle holds all the machinery systems associated with the WEC system such as rotor blades, gearbox, generator, and yaw mechanism. The nacelle can rotate and follow the wind speed direction with the help of a yaw mechanism.

2.2.4 Pitch Mechanism

The pitch mechanism in WEC system allows the rotation of the blades on their longitudinal axis. Thus, it can alter the aerodynamic characteristics of WEC system by adjusting the angle of attack of the blades with respect to the wind. Hence, the pitch mechanism provides control over the captured power so as to improve conversion efficiency, as well as to protect the WEC system from mechanical damage due to high-speed wind flow. When below the rated wind speed, the pitch angle is usually set to zero and the rotor speed is controlled to capture the maximum wind energy. However, when the wind speed is beyond a rated value, the pitch angle is adjusted to cut down the extra power so as to protect the WEC system from mechanical damage. The maximum pitch angle is usually between 20 and 25 degrees. Mechanical brakes are applied to shut down the power production due to excessively high wind speed.

2.2.5 Gearbox

The gearbox is used in the WEC system to match the lower rotational speed of the rotor blades and the higher rotational speed of the generator. The gearbox conversion ratio or gear ratio (G_r) can be calculated as

$$G_r = \frac{n_g}{n_t} = \frac{(1-s)60f_s}{Pn_t} \tag{2.1}$$

where s is the slip of the generator used, f_s is the frequency of the stator in Hz, P is the number of pole pairs of the generator, n_g and n_t are generator and turbine rated speed in rpm, respectively.

2.2.6 Coupling and Mechanical Brake

The mechanical brake is generally placed on the high-speed shaft in a WEC system between the gearbox and the generator. The brake is used in aerodynamic power control (stall or pitch) so as to shut down the turbine during times of excessively high winds or to keep the turbine in a parked mode for repairs and maintenance.

2.2.7 Yaw Drive

The yaw drive is used for the effective operation of the horizontal-axis WEC system. It helps to adjust the rotor facing in the direction of wind flow to produce maximum electric energy during the operation of WEC system.

2.2.8 Sensors

The pitch/stall and yaw control mechanism require the measured value of wind speed as well as wind direction. Hence, appropriate sensors are used to actuate and process different quantities in WEC system. Typical sensors used in WEC system include speed sensors, electrical voltage, current and power sensors, pitch position sensors, vibration sensors, hydraulic pressure sensors, and temperature and oil level indicators.

2.2.9 Power Electronic Converters

The power electronic converters are applied in the WEC system to process the electrical power generated from the wind turbine. The power electronic converters use electronic switches to convert AC power to DC (or vice versa), and to process and supply power to the grid or load. Different types of power converters can be used based on the configuration, rating and modes of operation, that is off-grid or grid connected operation of WEC system. The more description of converters used in WEC system will be discussed in subsection 2.9 in this chapter.

2.2.10 Generator

The generator is an essential component of WEC system and has the function of producing electric energy from wind flow. A typical WEC system uses IMs as the generator, that is, cage rotor IMs or wound rotor IMs. Permanent magnet synchronous machines are also employed in WEC system.

2.3 Power Characteristic Equations of Wind Turbines

This section discusses the power and torque generated by a WEC system by applying different mathematical models, which will be applied in system control discussed in Chapters 4 and 5. The WEC system converts kinetic energy of the wind into electrical energy. The mechanical power produced through the rotation of the blades of a wind turbine is a function of the kinetic energy of the air mass flowing through the turbine, formulated as [105]

$$P_{wind} = \frac{E_k}{t} = \frac{\frac{1}{2}m{v_w}^2}{t} = \frac{\frac{1}{2}\rho A d {v_w}^2}{t} = \frac{1}{2}\rho A {v_w}^3 = \frac{1}{2}\rho \pi R^2 {v_w}^3 \tag{2.2}$$

where ρ is air density; A represents the swept area of the air flow; R is the radius of the blades; and v_w is the velocity of the wind.

The mechanical power (P_m) converted from the wind flow can be estimated as

$$P_m = C_P P_{wind} = \frac{1}{2} C_P \rho \pi R^2 v_w^3 \tag{2.3}$$

where C_p is the power coefficient of the WEC system. The parameter C_P depends on the tip speed ration (λ) and pitch angle (β), which can be expressed as

$$C_p = c_1 \left(\frac{c_2}{\lambda_i} - c_3 \beta - c_4 \right) \mathrm{e}^{\frac{-c_5}{\lambda_i}} \tag{2.4}$$

where λ_i is related to λ through the following equation:

$$\frac{1}{\lambda_i} = \frac{1}{\lambda + 0.08\beta} - \frac{0.035}{1 + \beta^3} \tag{2.5}$$

The values of $c_1$to c_5 are estimated empirically. The term tip speed ratio can be estimated from the angular speed (ω) of the generator rotor and wind velocity v_w as [105]

$$\lambda = \frac{\omega R}{v_w} \tag{2.6}$$

The optimum limit of wind power utilization was first discovered theoretically by Betz, which is known as Betz limit [102]. According to Betz, maximum 59% of the wind power could be utilized by a WEC system; hence the maximum value of C_p can be 0.59. The usual value of C_p for a WEC system can be within the range of 0.2 to 0.5, depending on the λ and β [101]. Hence, the wind turbine electromechanical torque (T_{em}) can be calculated as [105]

$$T_{em} = \frac{P_m}{\omega} = \frac{1}{2} \frac{C_P \rho \pi R^2 v_w^3}{\lambda} \qquad (\mathrm{N.m}) \tag{2.7}$$

2.4 Configurations of Grid-connected WEC System

There are four typical types of grid-connected WEC system configurations [104]:

(1) Fixed-speed WEC system configuration;

(2) Limited speed control-based WEC system configuration;

(3) Partial scale converter-based WEC system configuration;

(4) Full capacity converter-operated WEC system configuration.

These configuration properties are discussed briefly below.

2.4.1 Fixed-Speed WEC System Configuration

Fixed-speed WEC system utilizes a squirrel cage induction generator (SCIG), which is connected to the grid through a transformer, as shown in Fig. 2.3. A soft starter is used to limit high in-rush currents at the time of starting in this configuration; however, the soft starter is bypassed after the system has started. A capacitor bank is used to provide the reactive power and voltage support for the system. Three basic control configurations are applied in fixed-speed wind turbines, namely, stall control, pitch control and active stall control. This configuration is simple and robust for low power applications. In addition, the system is also cost effective. However, there is no flexibility to control the speed of the SCIG, which limits the control of power flow to the grid. This system is also known as Type-1 configuration of WEC system.

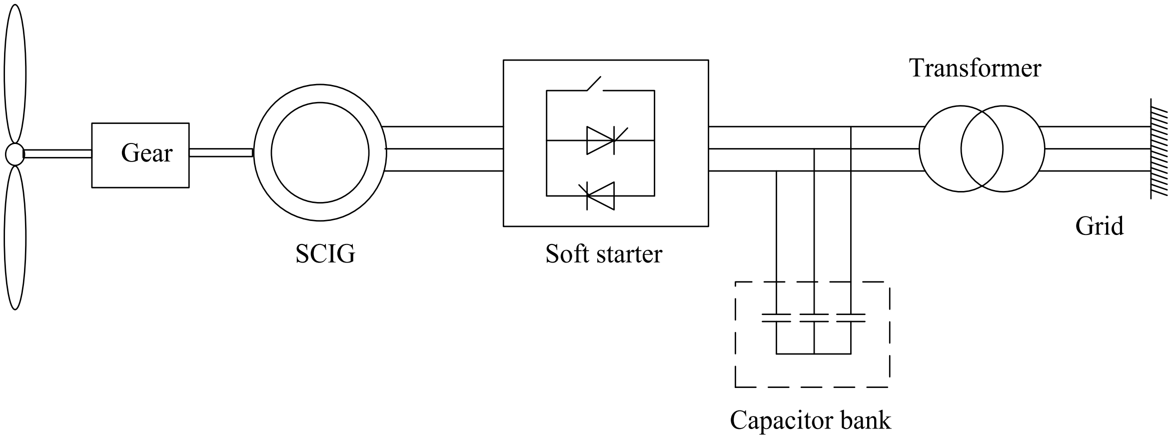

Fig. 2.3 Fixed speed WEC system configuration [104]

2.4.2 Limited-Speed Control-based WEC System Configuration

This configuration (Type-2) is mostly similar to the previous (Type-1) configuration; however, the rotor speed can be controlled in this WEC system configuration with the help of a variable resistor box as indicated in Fig. 2.4. This configuration utilizes a wound rotor induction generator (WRIG) and allows 10% variations of speed adjustment through the variable resistors [106]. Although this configuration of WEC system allows limited control of power flow to the grid, the variable resistor introduces power loss.

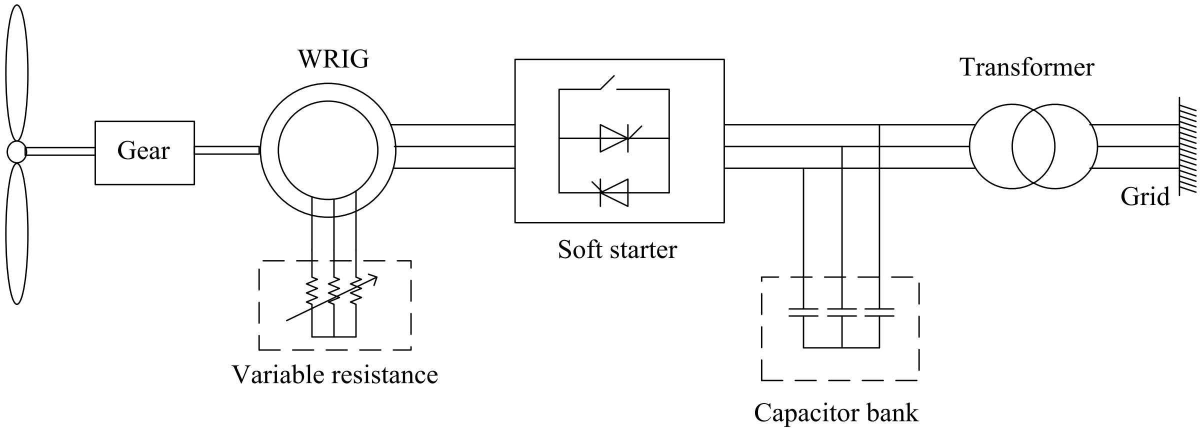

Fig. 2.4 Limited speed control-based WEC system configuration [104]

2.4.3 Partial Scale Converter based WEC System Configuration

This arrangement (Type-3) utilizes a doubly fed induction generator (DFIG) to convert wind energy to electricity, as depicted in Fig. 2.5. The stator side of the DFIG is directly connected to the grid, and the rotor side of the machine is connected through a back-to-back converter [106]. The rotor side connection allows the control of bi-directional power flow between the WEC system and the grid. This system allows 30% variations of rotor speed with an improved dynamic performance compared to Type-1 and Type-2 configurations. This configuration is more reliable and cost effective as it allows a partial-rated power converter for the operation, which is extensively used in the large wind farms. However, the Type-3 system needs a more complex control system and has high start-up costs.

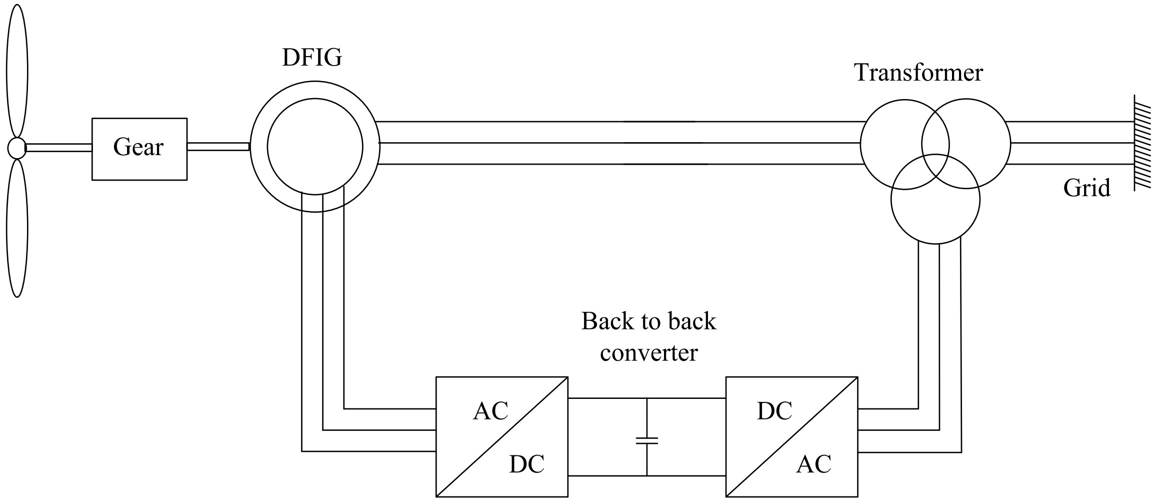

Fig. 2.5 Partial scale converter-based WEC system configuration [104]

2.4.4 Full Capacity Converter Operated WEC System Configuration

This is Type-4 WEC system configuration as demonstrated in Fig. 2.6. The WEC system converter allows 100% variation of rotor speed; hence it can be considered as a full variable speed wind turbine [106]. Moreover, this configuration can be operated by different types of generators like WRIG, wound rotor synchronous generator (WRSG), permanent magnet induction generator (PMSG), etc. This type of WEC system is connected to the grid through a converter and transformer and allows full control of power flow between WEC system and the grid. However, the full-scale power converter makes the system more vulnerable to continuous operation of WEC system and more expensive compared to other types of WEC system configurations.

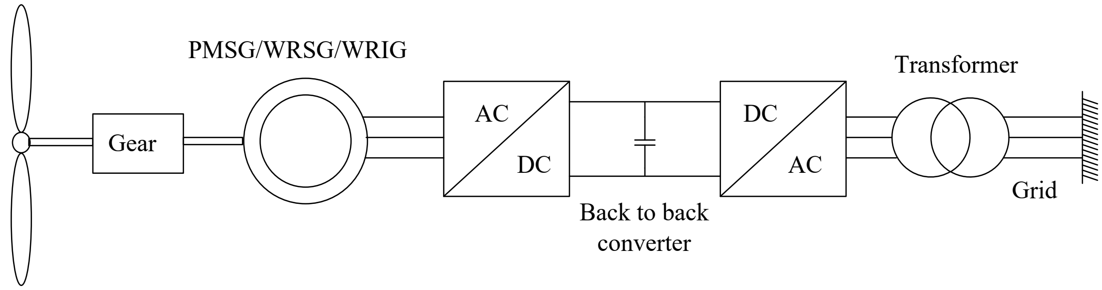

Fig. 2.6 Full capacity converter operated WEC system configuration [104]

In summary, among the aforementioned WEC system configurations, DFIG-based WEC system configuration has advantages of variable speed wind generation, fractional-sized converter, and flexible and bi-directional real and reactive power transfer capabilities. In addition, the DFIG configuration is cheap in price due to the use of fractional-sized converters, and more reliable for continuous operation of WEC system because the system is not fully dependent on power electronic devices [43], [56], [107]. Therefore, this research will focus on DFIG-based WEC system.

2.5 Mathematical Model of DFIG

The steady-state equivalent circuit, space vector model and the decoupled model of the DFIG will be discussed in this section, which will be used in the proposed DTF control techniques discussed in Chapters 4 and 5.

2.5.1 Steady State Equivalent Circuit of DFIG

The steady-state equivalent circuit of the DFIG is presented in Fig. 2.7, where the rotor quantities are referred to the stator side.

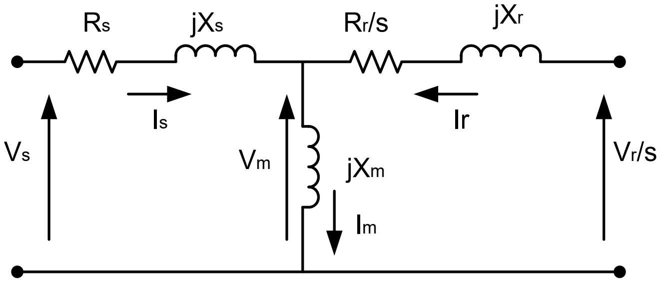

Fig. 2.7 Steady-state equivalent circuit of the DFIG

In the steady-state equivalent circuit of DFIG, the relationship between the related ?? quantities and components can be formulated as [108]

$$v_s = i_s R_s + jX_s i_s + v_m \tag{2.8}$$

$$v_r/s = i_r R_r + jX_r i_r + v_m \tag{2.9}$$

$$i_m = i_s + i_r \tag{2.10}$$

where

v_s and v_r — stator side phase voltage and rotor side phase voltage (V)

R_s and X_s — stator side resistance and reactance (Ω)

R_r and X_r — rotor side resistance and reactance (Ω)

X_m — magnetizing reactance (Ω)

s — generator slip

i_s and i_r — stator and rotor side current (A)

i_m —magnetizing current (A)

2.5.2 Space Vector Model of DFIG

The space vector model illustrates the relationship between different quantities of WEC system and the parameters of DFIG systems. The construction of the vector components depends on the reference frames selected for analysis. For example, if '*abc*' reference frame is selected, then the stator voltage vector $\bar{v}_s$ becomes [109]

$$\bar{v}_s = \begin{bmatrix} v_{sa} \\ v_{sb} \\ v_{sc} \end{bmatrix} \tag{2.11}$$

where

v_{sa}, v_{sb}, v_{sc}— phase voltages for stator (V)

Similarly, if *d*-*q*-axis reference frame is selected, then stator voltage vector will become:

$$\bar{v}_s = \begin{bmatrix} v_{sd} \\ v_{sq} \end{bmatrix} \tag{2.12}$$

where

v_{ds}, v_{qs} — *d*-*q* axis comments of $\bar{v}_s$

The other vector representations depend on the selection of reference frames. The voltage for the stator and rotor of the generator in a selected reference frame can be represented by

$$\bar{v}_s = R_s\bar{\imath}_s + p\bar{\psi}_s + j\omega\bar{\psi}_s \tag{2.13}$$

$$\bar{v}_r = R_r\bar{\imath}_r + p\bar{\psi}_r + j(\omega - \omega_r)\bar{\psi}_r \tag{2.14}$$

where

$\bar{v}_s, \bar{v}_r$— voltage vectors for stator and rotor (V)

$\bar{\imath}_s, \bar{\imath}_r$— current vectors for stator and rotor (A)

$\bar{\psi}_s, \bar{\psi}_r$ − flux-linkage vectors for stator and rotor (Wb)

R_s, R_r — winding resistances for stator and rotor (Ω)

ω — rotating speed of the selected reference frame (rad/sec)

ω_r— electrical angular speed for the rotor (rad/sec)

p — derivative operator

The equation of electromagnetic torque (T_{em}) is given by

$$T_{em} = \frac{3P}{2} Im(j\bar{\psi}_s\bar{\iota}_s) \tag{2.15}$$

P — number of pole pairs

The flux linkage vector $\bar{\psi}_s$ and $\bar{\psi}_r$ can be represented as [101]

$$\bar{\psi}_s = (L_{ls} + L_m)\bar{\iota}_s + L_m\bar{\iota}_r = L_s\bar{\iota}_s + L_m\bar{\iota}_r \tag{2.16}$$

$$\bar{\psi}_r = (L_{lr} + L_m)\bar{\iota}_r + L_m\bar{\iota}_s = L_m\bar{\iota}_s + L_r\bar{\iota}_r \tag{2.17}$$

where

$L_s = L_{ls} + L_m$ - self-inductance of the stator (H)

$L_r = L_{lr} + L_m$ - self-inductance of the rotor (H)

L_{ls}, L_{lr}- leakage inductances of stator and rotor (H)

L_m- mutual inductance (H)

Fig. 2.8 shows an equivalent circuit of DFIG in the arbitrary reference frame, rotating in space at the angular speed ω.

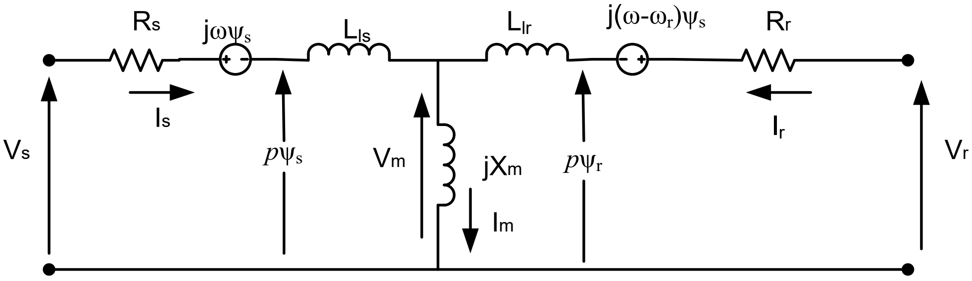

Fig. 2.8 Space vector equivalent circuit of DFIG in the arbitrary reference frame [103]

2.5.3 Decoupled Model (*d-q*-Axis Model) of DFIG

The decoupled model of the DFIG is also known as *d-q*-axis model, which can be obtained by selecting *d-q*-axis reference frame and decomposing the space vector components of the DFIG into *d*- *q*- axis comments, such as [101]

$$\bar{v}_s = v_{ds} + jv_{qs}$$

$$\bar{\iota}_s = i_{ds} + ji_{qs}$$

$$\bar{\psi}_s = \psi_{ds} + j\psi_{qs}$$

$$\bar{v}_r = v_{dr} + jv_{qr}$$

$$\bar{\imath}_r = i_{dr} + ji_{qr}$$

$$\bar{\psi}_r = \psi_{dr} + j\psi_{qr}$$

where

v_{ds}, v_{qs} — *d*-*q*- axis comments of $\bar{v}_s$

i_{ds}, i_{qs} — *d*-*q*- axis comments of $\bar{\imath}_s$

ψ_{ds}, ψ_{qs}— *d*-*q*- axis comments of $\bar{\psi}_s$

v_{dr}, v_{qr}— *d*-*q*- axis comments of $\bar{v}_r$

i_{dr}, i_{qr} — *d*-*q*- axis comments of $\bar{\imath}_r$

ψ_{dr}, ψ_{qr}—*d*-*q*- axis comments of $\bar{\psi}_r$

Substituting these *d*-*q*-axis components into Equations (2.13) and (2.14), and separating the real and imaginary parts, the following equations are established as

$$v_{ds} = R_s i_{ds} + p\psi_{ds} - \omega\psi_{qs} \tag{2.18}$$

$$v_{dr} = R_r i_{dr} + p\psi_{qs} + \omega\psi_{ds} \tag{2.19}$$

$$v_{dr} = R_r i_{dr} + p\psi_{dr} - (\omega - \omega_r)\psi_{qr} \tag{2.20}$$

$$v_{qr} = R_r i_{qr} + p\psi_{qr} + (\omega - \omega_r)\psi_{dr} \tag{2.21}$$

The *d*-*q*-axis flux linkages are obtained from Equations (2.16) and (2.17) as follows

$$\psi_{ds} = (L_{ls} + L_m)i_{ds} + L_m i_{dr} = L_s i_{ds} + L_m i_{dr} \tag{2.22}$$

$$\psi_{qs} = (L_{ls} + L_m)i_{qs} + L_m i_{qr} = L_s i_{qs} + L_m i_{qr} \tag{2.23}$$

$$\psi_{dr} = (L_{lr} + L_m)i_{dr} + L_m i_{ds} = L_r i_{dr} + L_m i_{ds} \tag{2.24}$$

$$\psi_{qr} = (L_{lr} + L_m)i_{qr} + L_m i_{qs} = L_r i_{qr} + L_m i_{qs} \tag{2.25}$$

where

L_{ls}— Self-inductance related to stator

L_{lr}— Self-inductance related to rotor

L_m— mutual inductance between stator and rotor winding

Hence, the electromagnetic torque T_{em} can be formulated as

$$T_{em} = \frac{3P}{2}\left(i_{qs}\psi_{ds} - i_{ds}\psi_{qs}\right) = \frac{3PL_m}{2}\left(i_{qs}i_{dr} - i_{ds}i_{qr}\right) = \frac{3PL_m}{2\left(L_sL_r - L_m^2\right)}\left(\psi_{dr}\psi_{qs} - \psi_{ds}\psi_{qr}\right) \quad (2.26)$$

Fig. 2.9 shows the *d-q* axis equivalent circuit of DFIG in the arbitrary reference frame, rotating in space at the angular speed ω.

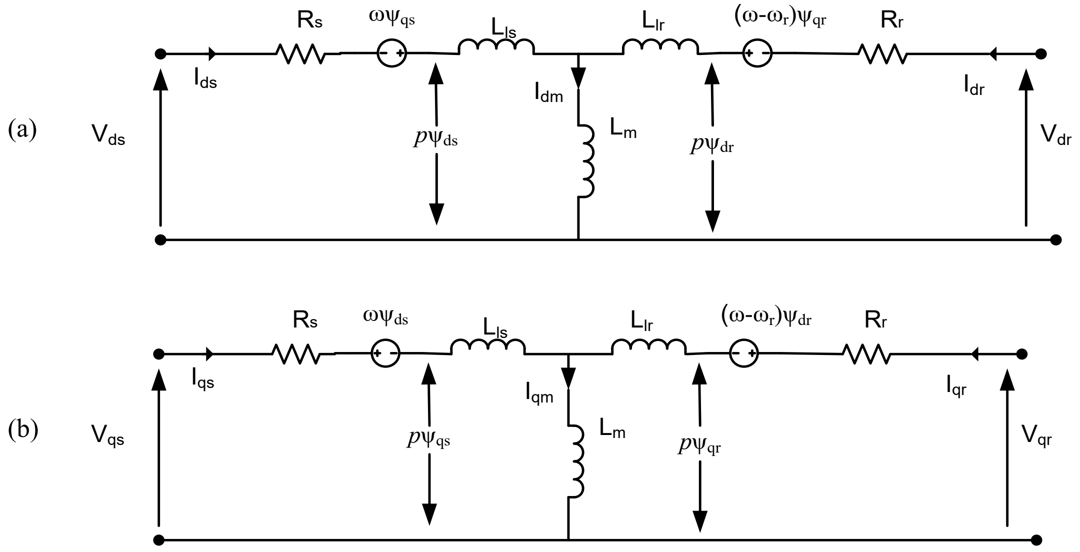

Fig. 2.9 The *d-q* axis equivalent circuits of DFIG: (a) *d*-axis, (b) *q*-axis.

2.6 Operation and Control of WEC System

The WEC system incorporates wind turbine blades, drive train, IM, converters, and other supplementary components to generate electric power. WEC system operation can be separated into four operating regions based on the wind speed variation, as illustrated in Fig. 2.10.

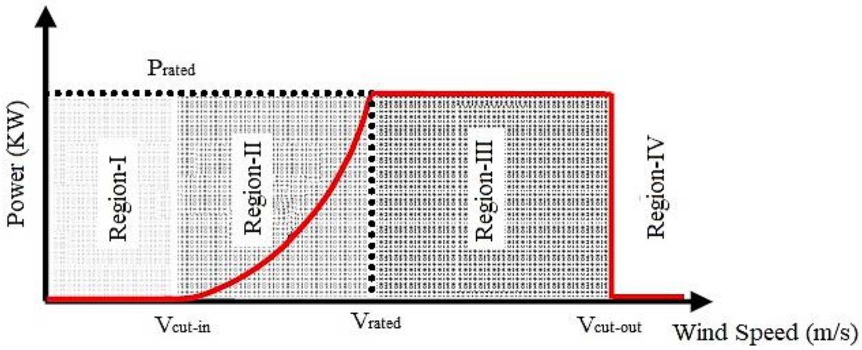

Fig. 2.10 Regions of WEC system operations [86]

In Region-I, the wind speed is very low and is not favorable to generate electric power. Region-II is a partial load region whereby power production begins when the wind speed is higher than the threshold cut-in speed ($V_{cut\text{-}in}$). Power production increases with the rise in wind speed until the rated velocity V_{rated}, whereby the rated power production is obtained. Region-III begins at the rated speed V_{rated} and the WEC system operates at full load with the rated power production. If the wind speed goes higher than the cut-out speed (V_{cut_out}), the system will shut down to prevent mechanical damage to the WEC system. Therefore, the power production will be terminated as indicated in Region-IV.

A conventional wind turbine control system is illustrated in Fig. 2.11. The torque controller operates in Region-II to generate maximum power from the wind at variable speeds. The pitch controller is applied to manipulate the blade pitch when the wind speed is greater than V_{rated}. The system continues to run in Region-III at the rated speed up to the wind speed $V_{cut\text{-}out}$. The objective of the pitch control is to reduce extra wind power and maintain the rated power production at full load operation in Region-III. The yaw control is used to set the wind turbine towards the direction of wind. The proposed ANF and INF based DTF control techniques in this work aim to control the WEC systems operating in Region-II.

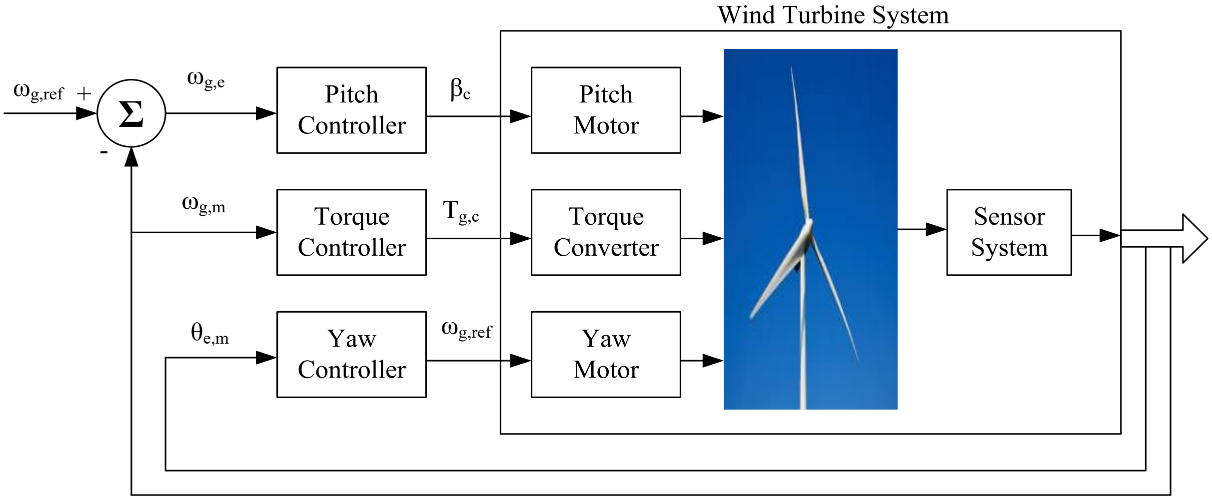

Fig. 2.11 Conventional wind turbine control system [86]

2.7 Power Converters

Several types of power converters can be used in WEC system considering the configuration, size and rating of the WEC system, as well as the cost. The power converters basically process the current, voltage and system frequency to make them compatible with load or grid side supply. Some commonly used power converters for WEC system are briefly discussed below.

2.7.1 Soft Starter

Soft starter-based power converters are used in Type-1 and Type-2 configurations of WEC system. This converter uses two back-to-back thyristor structures to process the AC power using the firing angle control of the thyristors. This converter ensures smooth operation at low power applications [103].

2.7.2 Diode Rectifier

The three-phase full bridge diode rectifiers are occasionally used in WEC system for power processing because the rectifier is cost effective and requires no additional control operations. Diode rectifiers are commercially available and can easily be connected to the DC bus system [103].

2.7.3 The Back-to-back Voltage Source Converter

The back-to-back pulse width modulation (PWM) voltage source inverter allows bi-directional power flow between WEC system and grid side. Hence, they are frequently used in WEC system of high-power applications. The Type-3 and Type-4 configurations predominantly use this configuration, which has a major advantage of capacitor decoupling. This capacitor decoupling allows independent control of both converters considering the requirements of grid and WEC system sides. However, the configuration introduces more switching losses as they require more power electronic switches on both sides of rotor and grid side. As the research focuses on DFIG based configurations of WEC systems, the back-to-back converters are selected for the WEC system (described in Chapters 4-5).

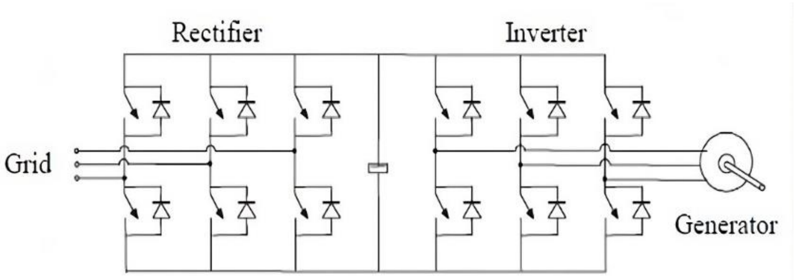

Fig. 2.12 Configuration of back-to-back PWM-VSI converter topology [110]

2.7.4 Matrix Converter

The matrix converter can provide robust performance by connecting the desired input current and voltage to the output terminals of the converter using the switching frequency. This converter has a higher operation efficiency compared to the back-to-back voltage source inverters due to having no decoupling through capacitor [101].

2.7.5 Multilevel Converter

The multilevel converter has the advantages of higher voltage capability and lower harmonic in output voltage. Hence, it has a good potential to be used in large-scale WEC system. However, a multilevel converter has higher switching losses, inequal curt stress among the switches used, etc. Fig. 2.13 shows a typical arrangement of the multilevel converter [110].

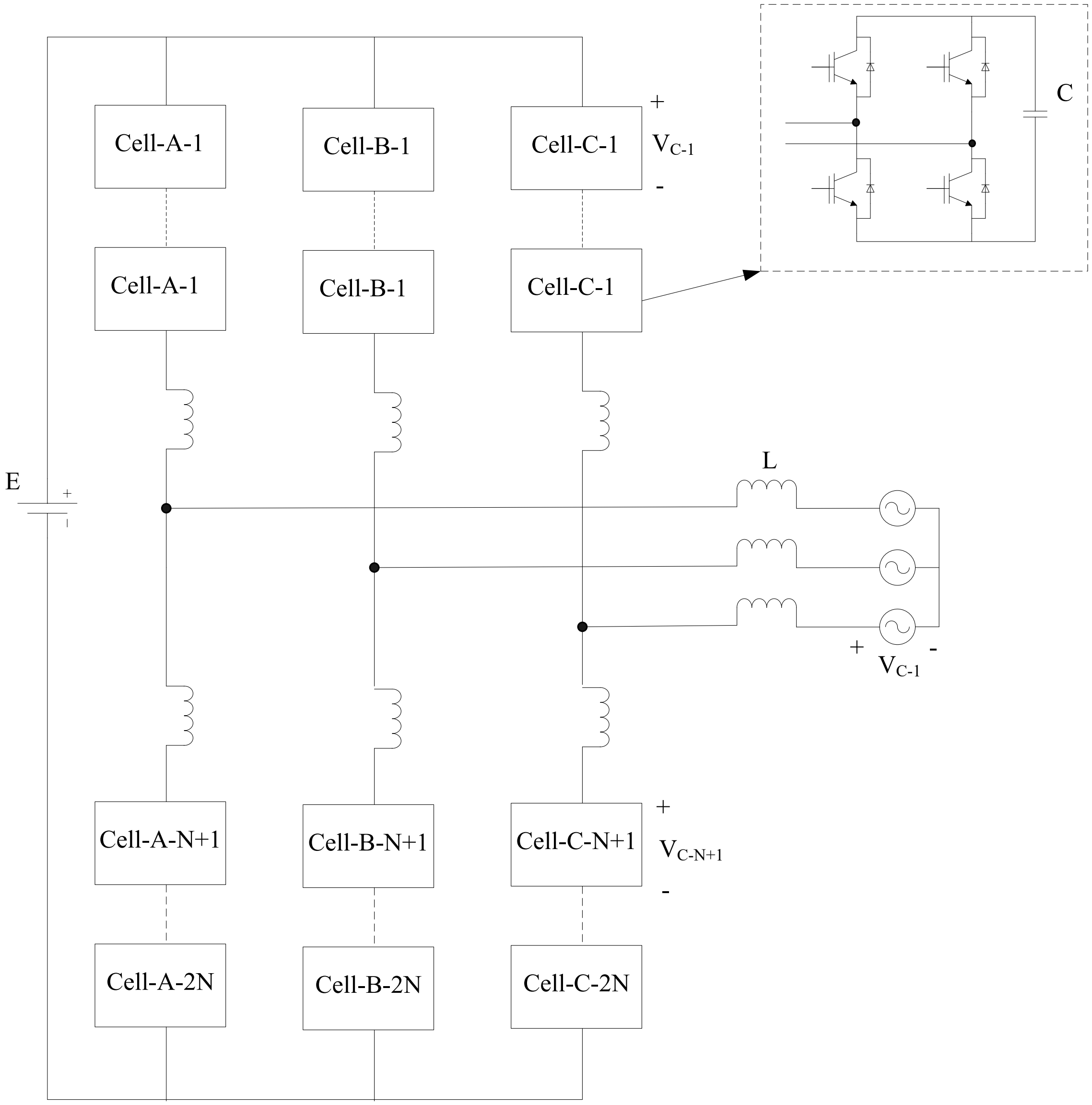

Fig. 2.13 Configuration of multilevel converter topology

2.8 Construction and Operation of IMs

IMs convert electrical energy into mechanical energy through the principles of electromagnetic induction [111]. An IM has two main parts of operation: the stator and the rotor. The stator is a stationary part consisting of stator windings placed systematically in the slots of the IMs. The stator slots are made of steel or cast-iron frames and have high permeable steel lamination inside the frame. On the other hand, the rotor of the IM is a rotating part, which can be a cage rotor or wound rotor by construction. The cage rotor structure applies copper or aluminium conductor bars that are embedded in semi-closed slots of a laminated rotor core. To form a closed path for the current flow, both ends of the rotor bars are shorted using end rings. The current flowing through this short path causes a magnetic field in the rotor, which makes the rotor rotate by interacting with the stator's magnetic field.

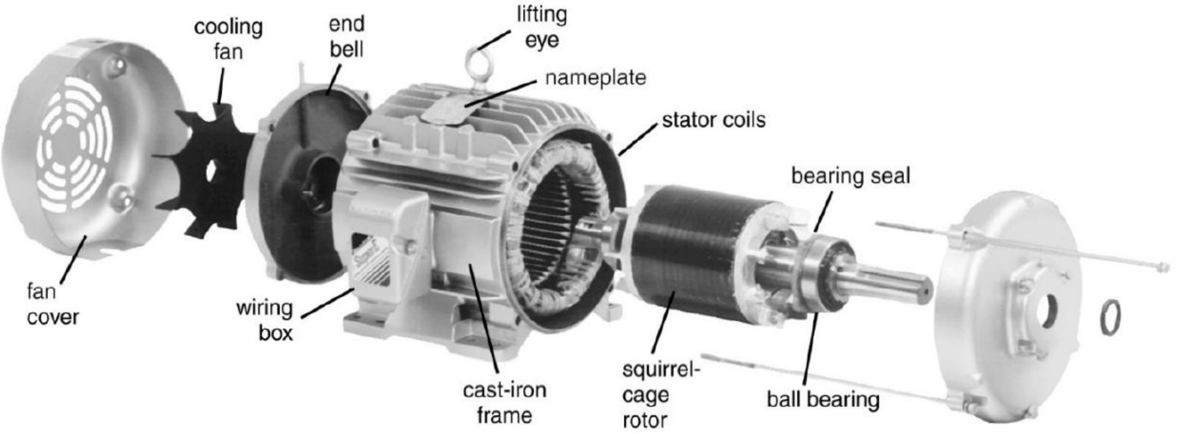

Fig. 2.14 Structure of an IM [111]

In an IM, a rotating magnetic field is created from a three-phase power supply when the IM is in operation. The speed of the rotating field is known as synchronous speed. When the rotor bars of the cage rotor are placed into the rotating field, an electromotive force (EMF) is induced in the rotor slots according to the law of electromagnetic induction [112]. The induced EMF causes a current flow through the rotor bars, as the bars are shorted through a slip ring. The current carrying conductors placed in rotating field created by stator causes the production of a mechanical force, which cause the rotor to rotate. Thus, the electric energy propagates through a magnetic medium to the rotor and is converted to mechanical energy or rotation.

In practical and industrial applications, an IM is characterized by two terms: slip and synchronous speed. The synchronous speed (n_s) is the speed of the rotation field, which depends on supply line frequency (f_l) and number of poles (P) of the IM, or

$$n_s = 120 \times \frac{f_l}{P} \tag{2.27}$$

The rotor always tries to catch the synchronous speed; however, it can never reach it. Hence, the slip of an IM can be estimated, considering the difference between the rotor speed and synchronous speed, such that

$$s = \frac{n_s - n_r}{n_s} \tag{2.28}$$

where n_r is the rotor speed and s is the slip of the IM.

2.9 Faults in IMs

It is essential to detect the faults reliably at the early stage of IM's operation to ensure the production accuracy, reliability and safety of the machine. The common IM defects can occur are in stators, rolling element bearings and rotors bars [113]. However, as discussed in Section 1.2.1 of Chapter 1, the BRB fault can cause severe damage of the IM if not being detected properly at the early stage. In addition, it is challenging to detect the BRB fault reliably as the RBR fault characteristic features could be time-varying in nature. Hence, this work will focus on fault detection in IM rotor bars.

2.9.1 BRB Faults of IMs

BRB faults can significantly affect the IM's performance. A BRB fault may cause imperfection such as unbalanced currents, fluctuation of torque, extra power loss, sparks, and reduction of average torque. BRB faults also increase vibration and acoustic noise and cause extra stress on IMs. When a rotor bar breaks, the adjacent bars have to carry more current, which can cause extra thermal and mechanical stress on those bars. Consequently, these adjacent rotor bars may also be damaged quickly. Thus, early recognition of rotor bar faults can prevent IM performance degradation or even catastrophic failures [17]. Fig. 2.15 shows a typical scenario of BRB fault, which can be caused by several reasons such as:

(1) manufacturing defects
(2) thermal stresses
(3) mechanical stress caused by bearing faults
(4) frequent starts of the motor at rated voltage
(5) metal fatigue of the rotor bar.

Fig. 2.15 A BRB fault [114]

BRB fault detection can be undertaken using different information carriers. However, MCSA could be the most commonly used technique to detect BRB faults due to its relative ease of measurement and higher signal-to-noise ratio for BRB fault detection [17]. This work will be based on MCSA for IM BRB fault detection. The characteristic frequency of the BRB fault f_k can be computed by

$$f_k = (1 \pm 2ks) \times f_0 \tag{2.29}$$

where f_0 is the power line frequency in Hz, and s is the slip and $k=0, \pm 1, \pm 2\ldots\ldots$

2.9.2 Other Faults of IMs

(1) Rolling element bearing faults

Rolling element bearing faults could be the most common defects in IMs. Rolling element bearings have three principal components: inner race, outer race and rolling balls. Hence, defects can occur in any of these bearing elements. Bearing faults can cause extra vibration and increase wear and tear [115].

(2) Stator short circuit turns

Stator winding faults usually occur due to damage to the insulation in stator winding [14]. This fault starts within a coil by an inter-turns short circuit. This type of fault can result in extra heating and destruction of the surroundings due to the asymmetry among the three phases of the stator of IM.

(3) Air gap eccentricity

Air gap eccentricity is a defect in IMs, which is caused by the asymmetric distance between a rotor and a stator. This type of defect can increase mechanical vibration, insulation degradation and unbalanced magnetic pull rotor-stator rubbing [14].

2.10 Chapter Conclusion

This chapter discusses the mathematical modeling, configurations and control of the WEC systems. The decoupled mathematical model of DFIG is presented in detail, which will be utilized to design and implement the intelligent controller for WEC systems as discussed in the following chapters. Different IM structures and fault conditions are also discussed in this chapter, including the cause and effect of BRB faults, as well as the motivations of fault tolerant control.

Chapter 3

An Enhanced EMD Technique for Broken Rotor Bar Fault Detection in Induction Machines

In order to improve the accuracy of signal processing-based broken rotor bar (BRB) fault detection of IM, an enhanced EMD (EEMD) technique is proposed in this chapter to recognize representative features from current signals for IM fault detection, specifically for BRB fault detection. The effectiveness of the proposed EEMD technique is verified experimentally.

3.1 Theoretical Analysis of the Proposed EEMD Technique

The proposed EEMD technique consists of the following processing steps: selection of targeted IMFs, OAMF-based spectral analysis, and postprocessing for IM BRB fault detection. Fig. 3.1 presents the processing block diagram of the proposed EEMD technique. The relevant theories are discussed in this section. Additionally, the proposed MWOA technique is also systematically outlined in this section.

3.1.1. Overview of EMD-based BRB Fault Detection

As discussed in the introduction, BRB faults can be detected using different information carriers, and this work will be based on MCSA. If one or more IM rotor bars are broken, the symmetry of the cage winding rotor will be affected as the BRBs are unable to carry the original current. Consequently, a backward rotating field is created in the IM. Additionally, extra sidebands would be formed on the MCSA spectrum because extra vibration can be induced in the stator current. As a result, the characteristic frequency of the BRB fault f_c can be computed by [17].

$$f_c = f_B \times (1 \pm 2ks) \tag{3.1}$$

where and s is the slip of the rotor calculated as

$$s = \frac{n_s - n_r}{n_s} \tag{3.2}$$

where n_s and n_r represent the synchronous and the rotor speed in rpm, f_B is the fundamental/basic line frequency in Hz, $k = 0, 1, 2 \ldots$ is the harmonic integer. IM BRB fault detection is a process to recognize f_c related representative features.

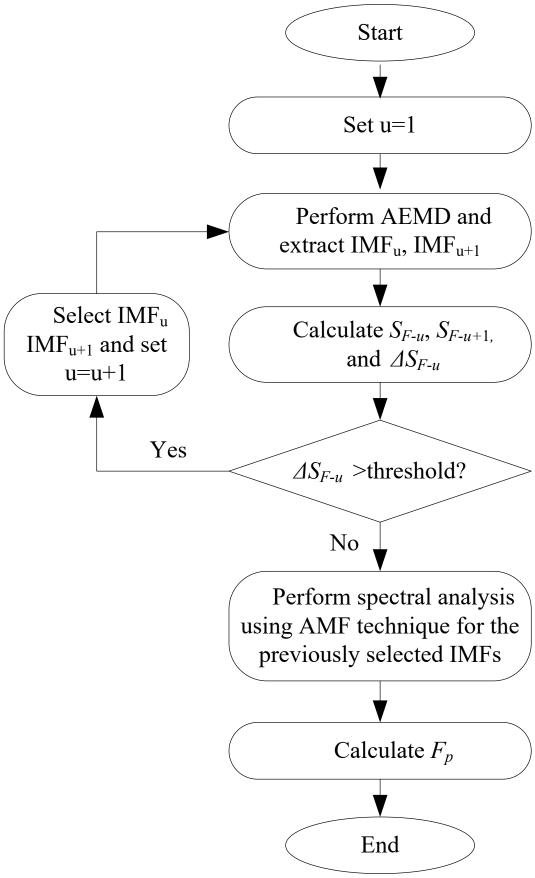

Fig 3.1 Operation flowchart of the proposed EEMD technique.

The EMD algorithm decomposes the original signal $x(t)$ into N IMFs and a residual or

$$x(t) = \sum_{i=1}^{N} y_i(t) + r(t) \tag{3.3}$$

where $y_i(t)$ is the i^{th} IMF and $r(t)$ is the residue. The processing starts from the identification of upper and lower value envelopes E_{max} and E_{min} from local maxima and minima of the original signal. The computation of the IMF starts by calculating the mean value $\bar{x}$:

$$\bar{x}(t) = \frac{E_{max} + E_{min}}{2} \tag{3.4}$$

This mean value $\bar{x}(t)$ is subtracted from the original signal $x(t)$ to get a new signal g_1

$$g_1 = x(t) - \bar{x}(t) \tag{3.5}$$

To become an IMF, g_1 must satisfy the following two conditions:

(1) The difference between the number of extrema and the number of zero-crossings points is either 0 or 1.

(2) The mean value of the envelope due to the local maxima and local minima is zero.

If g_1 cannot satisfy these two criteria for an IMF, then $x(t)$ is replaced by g_1 and the same processes are repeated until the first IMF, IMF_1, is found, and then $\mathrm{IMF}_1 := g_1$ and residual $r(t) = x(t) - g_1$. This residual is further used as an input signal to calculate the following IMFs. The above procedures are repeated until the required number of IMFs are produced [1].

3.1.2 Proposed Similarity Function Analysis

The phase of a real-time signal is dependent on initial switching time of the measuring unit, as the signal is time-varying in nature. Hence, it is difficult to estimate the similarity between a fixed benchmark signal and a real-time signal using classical correlation function since the classical correlation function is sensitive to phase difference (or phase) of the two signals [116]. Hence, a new similarity function (S_F) is proposed, which is insensitive to the phase difference (or phase) between two signals. The proposed S_F can estimate the similarity between a fixed benchmark signal and a real-time signal without considering the initial switching time. The proposed similarity function (S_F) to assess the spectral component similarities between the signal of interest and the benchmark signature as

$$S_F = \frac{r_{wz}}{\sqrt{r_{ww} \cdot r_{zz}}} \tag{3.6}$$

where

$$r_{wz} = \sqrt{\left(\sum_{n=-l}^{l} \sum_{l=-N_T}^{N_T} [w(n) \times z(n-l)]^2\right)}$$

$$r_{ww} = \sqrt{\left(\sum_{n=-l}^{l} \sum_{l=-N_T}^{N_T} [w(n) \times w(n-l)]^2\right)}$$

$$r_{zz} = \sqrt{\left(\sum_{n=-l}^{l} \sum_{l=-N_T}^{N_T} [x(n) \times z(n-l)]^2\right)}$$

where $w(n)$ and z(n) are the two signals to be compared; $l = \pm 1, \pm 2, \ldots \pm N_T$; N_T is the total number of samples in $w(n)$ and z(n). For example, assume a benchmark monotonic current signal $w(n)$ having power line frequency, expressed as $w(n) = W cos(2\pi qn + \varphi)$, where W is the amplitude of $w(n)$; $q = f/f_s$, $f = 60$ Hz and f_s is the sampling frequency; $z(n)$ is the measured current signal; C_{wz} denotes the cross-correlation between $w(n)$ and $z(n)$; φ is the phase difference between $w(n)$; and $z(n)$. Fig. 3.2 illustrates the proposed similarity function S_F and C_{wz} corresponding to phase differences between the $w(n)$ and $z(n)$. It is evident that the proposed S_F is not sensitive to the phase variations between the two signals, or S_F is independent of the starting time of measured current signal, which makes it more efficient for correlation analysis.

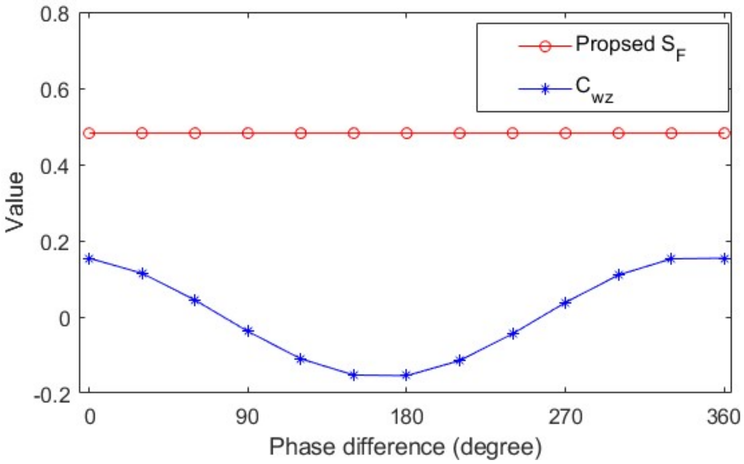

Fig. 3.2 S_F and C_{wz} in terms of phase differences (φ).

3.1.3 Implementation of the Proposed EEMD Technique

The selection of the representative IMFs and the termination procedure of the proposed EEMD technique is performed considering the value of ΔS_{F-u}, which can be calculated as

$$\Delta S_{F-u} = S_{F-u} - S_{F-u+1} \tag{3.7}$$

where S_{F-u} and S_{F-u+1} indicate the similarity of IMF_u and IMF_{u+1} with the benchmark signature, respectively, which will be calculated using Equation (3.6), u indicates the order of IMF. If the value of ΔS_{F-u} is less than a threshold, the IMF generation process will be terminated. The selection of threshold value for ΔS_{F-u} will be discussed in the next section. The operation of OAMF and post-processing function F_P will be discussed systematically in the next subsections.

3.1.4 Proposed Adaptive Multiband Filter Technique

When one or more IM rotor bars is broken, it may result in sideband spectral components around the basic frequency f_B on the MCSA spectrum due to asymmetric magnetic field distribution. These sidebands could contain characteristic frequency components, as specified in Equation (3.1). However, these sideband spectral components are usually sensitive to loading and speed of the machine. Consequently, an OAMF technique is proposed in this section to recognize the characteristic spectral components to detect IM fault without reconstructing the original signal. This filter operation applies an adaptive bandwidth windowing function to process the data associated with characteristic spectral components. The bandwidth of the adaptive window for OAMF is determined based on the slip and the order of the characteristic frequency to enhance the characteristic spectral peaks.

To facilitate analysis, represent f_c in Equation (3.1) by $f_{ck\pm}$. Consequently Equation (3.1) can be expressed as

$$f_{ck\pm} = f_B(1 \pm 2ks) \tag{3.8}$$

where $f_{ck\pm}$ characteristic sideband frequency; k = 1, 2,...., N, and N is the order of sideband; '±' denote the upper and lower sidebands, respectively. The bandwidth (Δf_{ck}) of the adaptive window can be estimated by

$$\Delta f_{ck} = \frac{s \times \beta}{2^{(k-1)}} \tag{3.9}$$

where β is a constant relevant to current spectrums at different speed and fault levels of IM, which will be discussed in Section 3.3.3. It is seen from Equation (3.9) that Δf_{ck} can alter its value adaptively based on the value of slip s and sideband k. The upper and lower range of frequencies ($f_{ck\pm\_U}$ and $f_{ck\pm\_L}$) for the windowing can be determined by

$$f_{ck\pm\_U} = f_{ck\pm} + \Delta f_{ck} \tag{3.10}$$

$$f_{ck\pm\_L} = f_{ck\pm} - \Delta f_{ck} \tag{3.11}$$

For example, for the first upper characteristic side-band frequency (k = 2), the lower and upper windowing functions are

$$f_{c2+\_U} = f_{c2+} + \Delta f_{c2} = f_{c2+} + \frac{(s \times \beta)}{2}$$

$$f_{c1+\_L} = f_{c2+} - \Delta f_{c2} = f_{2+} - \frac{(s \times \beta)}{2}$$

So, the proposed adaptive windowing functions $W_{ck\pm}$ are formulated as

$$W_{ck\pm}{=}\alpha\left(\left[1{+}e^{-a(f-f_{ck\pm\_L})}\right]^{-1}{-}\left[1{+}e^{-a(f-f_{ck\pm\_U})}\right]^{-1}\right) \tag{3.12}$$

where α is the accentuation factor which indicates the amount of accentuation applied to the spectral values under the window. For example, for the first upper characteristic sideband (k=1) the adaptive window functions will be

$$W_{c1+}{=}\left[1{+}e^{-a(f\text{-}f_{c1+\_L})}\right]^{-1}{-}\left[1{+}e^{-a(f\text{-}f_{c1+\_U})}\right]^{-1}$$

For this analysis the value of α will be optimized using the proposed modified WOA (MWOA) algorithm which will be discussed systematically in the following subsection. Additionally, the selection of optimized value α will be discussed in Section 3.3.3. Fig. 3.3 graphically illustrates the window function ($W_{ck\pm}$). $W_{ck\pm}$ can changed adaptively based on Δf_{ck}, as well as s and k.

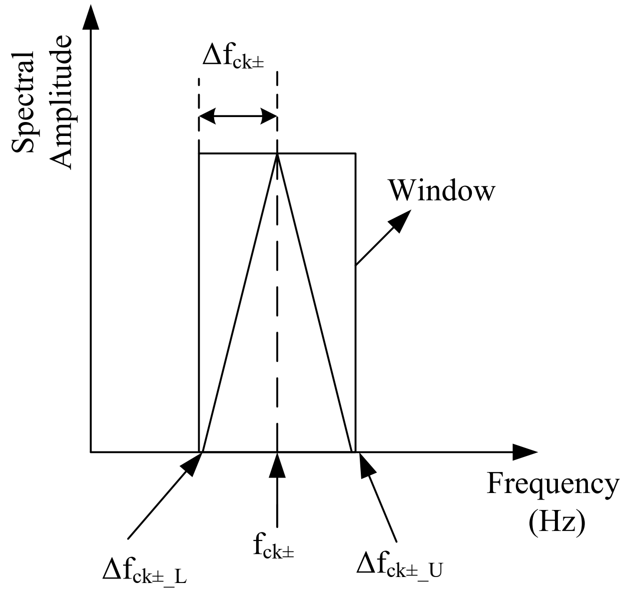

Fig. 3.3 Proposed window function

The spectral dataset (D_S) from the MCSA can be considered mathematically as,

$$D_S = ⊎(y_n, f_n) \tag{3.13}$$

where the operator '⊎' represents the combination of data points in $D_S \in \mathbb{R}^2$, which contains two-dimensional data; y_n is the spectral value of frequency f_n on the spectrum, $n \in \mathbb{N}$, $\mathbb{N} = \{0, 1, 2, \ldots.\}$ is the set of natural number. Incorporating the basic line frequency (f_B), database D_B can be represented as

$$D_B = ⊎\left(y_{m_1}, f_{m_1}\right) \tag{3.14}$$

where $D_B \epsilon \mathbb{R}^2, m_1 \epsilon \mathbb{N}$; y_{m1} is the spectral value of frequency f_{m_1} on D_B.

The following spectral operation is performed to construct D_B as

$$y_{m_1} := y_n\,, \qquad f_{m_1} \epsilon [f_B - \delta\,, f_B + \delta] \tag{3.15}$$

where the selection of value of δ will be discussed in Section 3.2.3.

The datasets ($D_{ck\pm}$) will contain the obtained characteristic frequencies, on D_S such that

$$D_{ck\pm} = ⊎\left(y_{m_2}, f_{m_2}\right) \tag{3.16}$$

where $D_{ck\pm} \epsilon \mathbb{R}^2$ and $m_2 \epsilon \mathbb{N}$; and

$$y_{m_2} = y_n W_{ck\pm}, \;\; f_{m_2} \epsilon \left[f_{ck\pm_L}, f_{ck\pm_U}\right] \tag{3.17}$$

The dataset that does not contain $f_{ck\pm}$, are represented as $D_{rk\pm}$ or

$$D_{rk\pm} = ⊎\left(y_{m_3}, f_{m_3}\right) \tag{3.18}$$

where $D_{rk\pm} \epsilon \mathbb{R}^2$ and $m_3 \epsilon \mathbb{N}$. A moving average operation is undertaken to construct $D_{rk\pm}$ such that

$$y_{m3} = \frac{1}{n}\sum_{i=0}^{n-1} y_{n-i}, \qquad f_{m3} \epsilon \left[f_{c(k-1)\pm\_U}, f_{ck\pm\_L}\right] \tag{3.19}$$

where y_n is the spectral value of frequency f_n on D_S as described in Equation (3.13).

The modified dataset D_M is constructed by

$$D_M = D_B \oplus D_{ck\pm} \oplus D_{rk\pm} \tag{3.20}$$

where '$\oplus$' represents the combination operation of the datasets. The steps of OAMF operation can be summarized as follows.

1) Calculate slip s using Equation (3.2).

2) Determine $f_{ck\pm}$ and Δf_{ck} using Equation (3.8) and (3.9).

3) Compute the frequency ranges $f_{ck\pm\_U}$, $f_{ck\pm\_L}$ using Equation (3.10) and (3.11).

4) Construct adaptive window $W_{ck\pm}$ using Equation (3.12).

5) Construct the datasets D_B, $D_{ck\pm}$, and $D_{rk\pm}$ using Equation (3.13) to (3.19).

6) Formulate D_M using Equation (3.20).

3.1.5 Chaotic Function-based Modified Whale Optimization Algorithm (MWOA)

The aim of the proposed MWO method is to enhance searching capability of the global optima, by applying a novel chaotic function (c_f) for processing, presented as

$$c_f^{t_i+1} = \begin{cases} \emptyset_f^{t_i+1}, & -1 \le \emptyset_f^{t_i+1} \le 1 \\ \emptyset_f^{t_i+1} - 1, & \emptyset_f^{t_i+1} \ge 1 \\ \emptyset_f^{t_i+1} + 1, & \emptyset_f^{t_i+1} \le -1 \end{cases} \tag{3.21}$$

where

$\emptyset_f^{t_i+1} = 0.5\left[sin\left(t_i * cos^{-1}\left(\emptyset_f^{t_i}\right)\right)\right] + 0.5\left[\frac{a}{4} * cos\left(\pi\emptyset_f^{t_i}\right)\right]$; and t_i indicates the number of iterations. The presented function in Eq. (3.21) has two independent chaotic state generation terms to generate random states. It generates states randomly between [-1, 1], which is different from general chaotic functions over [0, 1]. In MWO method the position of the population is updated using either encircling prey or spiral bubble net attacking strategy. For the encircling prey strategy, the updating of the population is given as

$$x_i^{t_i+1} = x^{*t_i} - 2c_f^{t_i+1}.D \tag{3.22}$$

where D represents the distance between the population x^t and the beat solution x^{*t} at t^{th} iteration, and $r \in [0, 1]$ is a random number.

$$D = |C \times x^{*t_i} - x^{t_i}| \tag{3.23}$$

$$C = 2 \times r \tag{3.24}$$

Additionally, using the spiral bubble net attacking strategy, the population is updated by

$$D' = |x^{*t_i} - x^{t_i}| \tag{3.25}$$

$$x^{t_i+1} = D' e^{bc_f^{t_i+1}} \times \cos\left(2\pi c_f^{t_i+1}\right) + x^{*t_i} \tag{3.26}$$

where D' represents the distance between the population x^t and the beat solution x^{*t} at t^{th} iteration. Hence the mathematical model is formulated as

$$x^{t+1} = \begin{cases} x^{*t_i} - 2c_f^{t_i+1}.D\,, \ p < 0.5 \\ D' e^{bc_f} \times \cos\left(2\pi c_f^{t+1}\right) + \ x^{*t_i}, \ p \geq 0.5 \end{cases} \tag{3.27}$$

where $p \in [0, 1]$ is a random number.

3.1.6 Proposed Post-processing Operation

A new post-processing function F_P is proposed to enhance feature characteristics and derive a fault index for automatic fault detection, defined as

$$F_P = \sum_{u=1}^{U} \theta_u \sum_{\substack{k=-n \\ k \neq 0}}^{n} \rho_k \frac{y_{ck} - y_{avg,k}}{y_f - y_{ck}} \tag{3.28}$$

where

y_{ck} is the mean spectral value at $f_{ck\pm} = \frac{y_{ck+} + y_{ck-}}{2}$,

y_f is the spectral value at fundamental frequency 60 or 50 Hz,

$y_{avg,k}$ is average spectral value associated with f_{ck}.

ρ_k is the scaling factor. The selection of value for ρ_k is discussed in Section 3.2.3.

θ_u represents the coefficients related to the selected IMFs estimated as

$$\theta_u = \frac{S_{F-u}}{\sum_{u=1}^{U} S_{F-u}} \tag{3.29}$$

u=1, 2, …., U; U represents the number of IMFs considered for analysis.

3.2 Experimental Tests and Performance Analysis

3.2.1 Effectiveness Analysis for the Proposed MWOA

The effectiveness of the proposed MWOA is investigated comparing this algorithm to the classical schemes related to WOA [39] as

Scheme 1: Classical WOA

Scheme 2: Chebyshev chaotic function based WOA

Scheme 3: Sine chaotic function based WOA

Scheme 4: Logistic chaotic function based WOA.

Fifteen benchmark unimodal and multimodal functions [117] are used to investigate the effectiveness in terms of mean and standard deviation (SD) of optima obtained from 20 trials. Table 3.1 shows the details of benchmark functions with their details; Table 3.2 shows the numerical representation of the comparative study. From the numerical analysis presented in Table 3.2, it can be concluded that the proposed MWOA is able to reach global minima more effectively compared to the traditional schemes. For example, in case of function 6 (Michalewics function) the proposed MWO algorithm has the average minima of -1.807, which is closer to the global minima 1.8013, in comparison with the other related methods that have the respective average minima of -1.538, -1.732, -1.484, -1.24 for Schemes 1 to 4 respectively. Additionally, MOWA is more consistent compared to the other schemes in terms of reaching global optima of the benchmark functions, which is reflected from the lower value of SD in each case. For example, for the function F6 and proposed MWO algorithm the SD is 2.22×10^{-2} whereas the values of SD for other related methods are 0.377, 0.083, 0.352, 0.689, respectively. Hence, the MOW method is more consistent compared to the other related schemes in global optimum searching.

Table 3.1 Details of 15 benchmark functions

F. No.	**Function Details**
F1	Branin function: $$g(x) = \left(x_1 - \frac{5}{4\pi^2}x_1^2 + \frac{5}{\pi}x_1 - 6\right)^2 + 10\left(1 - \frac{1}{8\pi}\right) cos\, x_1 + 10$$ Search Domain: $-5 < x_1 < 10$ and $0 < x_2 < 15$ No: of local minima: No local minima. Value of Global minima: $g^*(x) = 0.397887$
F2	Trid function: $$g(x) = \sum_{i=1}^{n}(x_i - 1)^2 - \sum_{i=2}^{n} x_i x_{i-1}$$ Search Domain: $-n^2 < x_i < n^2\ ; i = 1, 2, \dots, n\ ; n = 6$ No: of local minima: No local minima. Value of Global minima: $g^*(x) = -30$
F3	Zakharov function: $$g(x) = \sum_{i=1}^{n} x_i^2 + \left(\sum_{i=1}^{n} 0.5ix_i^2\right)^2 + \left(\sum_{i=1}^{n} 0.5ix_i^2\right)^4$$ Search Domain: $-5 < x_i < 10\ ; i = 1, 2, \dots, n\ ; n = 4$ No: of local minima: No local minima. Value of Global minima: $g^*(x) = 0$
F4	Sum Squares function: $$g(x) = \sum_{i=1}^{n} ix_i^2$$

	Search Domain: $-10 < x_i < 10\,; i = 1, 2, \ldots., n\,; n = 10$ No: of local minima: No local minima. Value of Global minima: $g^*(x) = 0$
F5	Sphere function: $$g(x) = \sum_{i=1}^{n} x_i^2$$ Search Domain: $-5.12 < x_i < 5.12\,; i = 1, 2, \ldots., n\,; n = 10$ No: of local minima: No local minima. Value of Global minima: $g^*(x) = 0$
F6	Michalewics function: $$g(x) = -\sum_{i=1}^{2} sin(x_i)\, sin^2\left(\frac{ix_i^2}{\pi}\right)^{2m}\,; m = 10$$ Search Domain: $0 < x_i < \pi\,; i = 1, 2$ No: of local minima: several local minima. Value of Global minima: $g^*(x) = -1.8013$
F7	Shubert function: $$g(x) = \left(\sum_{i=1}^{5} \mathrm{i}\cos((i+1)x_1 + i)\right)\left(\sum_{i=1}^{5} \mathrm{i}\cos((i+1)x_2 + i)\right)$$ Search Domain: $-10 < x_1 < 10 \text{ and } -10 < x_2 < 10$ No: of local minima: several local minima. Value of Global minima: $g^*(x) = -186.7309$

F8	Goldstein and Price function: $g(x) = \left(1 + (x_1 + x_2 + 1)^2(19 - 14x_1 + 13x_1^2 - 14x_2 + 6x_1x_2 + 3x_2^2)\right)(30 + (2x_1 - 3x_2)^2(18 - 32x_1 + 12x_1^2 - 48x_2 - 36x_1x_2 + 27x_2^2))$ Search Domain: $-2 < x_1 < 2$ and $-2 < x_2 < 2$ No: of local minima: several local minima. Value of Global minima: $g^*(x) = 3$
F9	Beale function: $g(x) = (1.5 - x_1 + x_1x_2)^2 + (2.25 - x_1 + x_1x_2^2)^2 + (2.625 - x_1 + x_1x_2^3)^2$ Search Domain: $-4.5 < x_1 < 4.5$ and $-4.5 < x_2 < 4.5$ No: of local minima: several local minima. Value of Global minima: $g^*(x) = 0$
F10	Perm function: $g(x) = \sum_{k=1}^{n}\left(\sum_{i=1}^{n}(i^k + b) \times \left(\frac{x_i}{i}\right)^k - 1\right)^2$ Search Domain: $-2 < x_i < 2\,; i = 1,2\,; n = 2$ No: of local minima: several local minima. Value of Global minima: $g^*(x) = 0$
F11	Ackley function: $g(x) = 20 + e - 20e^{-\frac{1}{5}\sqrt{\frac{1}{n}\sum_{i=1}^{n} x_i^2}} - e^{\frac{1}{n}\sum_{i=1}^{n}\cos(2\pi x_i)}$ Search Domain: $-15 < x_i < 15\,; i = 1,2\,; n = 2$ No: of local minima: several local minima. Value of Global minima: $g^*(x) = 0$

F12	Rastrigin function: $g(x) = 10n - \sum_{i=1}^{n}(x_i^2 - 10cos(2\pi x_i))$ Search Domain: $-5.12 < x_i < 5.12\,; i = 1,2\,; n = 2$ No: of local minima: several local minima. Value of Global minima: $g^*(x) = 0$
F13	Levy function: $g(x) = \sin^2(\pi y_i) + \sum_{i=1}^{n-1}[(y_i - 1)^2(1 + 10\sin^2(\pi y_i + 1))] + (y_n - 1)^2(1 + 10\sin^2(2\pi y_n)) \;\; ; y_i = 1 + \frac{x_i - 1}{4}$ Search Domain: $-10 < x_i < 10\,; i = 1,2,3\,; n = 3$ No: of local minima: several local minima. Value of Global minima: $g^*(x) = 0$
F14	Hartmann function: $g(x) = -\sum_{i=1}^{4} a\, e^{\left(-\sum_{j=1}^{3} B_{ij}\left(x_i - Q_{ij}\right)^2\right)}$ $a = [1 \quad 1.2 \quad 3 \quad 3.2]$ $B = \begin{bmatrix} 3 & 10 & 30 \\ 0.1 & 10 & 35 \\ 3 & 10 & 30 \\ 0.1 & 10 & 35 \end{bmatrix}, Q = 10^{-4}\begin{bmatrix} 6890 & 1170 & 2673 \\ 4699 & 4387 & 7470 \\ 1091 & 8732 & 5547 \\ 381 & 5743 & 8828 \end{bmatrix}$ Search Domain: $0 < x_i < 1\,; j = 1,2,3$ No: of local minima: several local minima. Value of Global minima: $g^*(x) = -3.86278$

F15	Dixon and Price function: $g(x) = (x_1 - 1)^2 + \sum_{i=2}^{n} i\left(2x_i^2 - x_{(i-1)}\right)^2$ Search Domain: $-10 < x_i < 10\,; i = 1,2,\dots,5$ No: of local minima: several local minima. Value of Global minima: $g^*(x) = 0$

Table 3.2 Numerical comparison of the study

Function		**Proposed MWOA**	**Scheme 1**	**Scheme 2**	**Scheme 3**	**Scheme 4**
F1	Mean	0.398	0.504	0.449	0.679	0.578
	SD	29.18×10^{-3}	19.37×10^{-2}	10.7×10^{-2}	0.206	0.347
F2	Mean	-29.762	-25.034	-5.658	-20.04	-16.04
	SD	0.293	12.72	7.96	7.077	10.35
F3	Mean	3.5×10^{-4}	3.55	0.27	4.311	3.38
	SD	1.106×10^{-3}	2.543	0.748	2.420	2.74
F4	Mean	1.98×10^{-4}	2.219	2.72	5.637	5.24
	SD	2.3×10^{-4}	3.353	3.4	4.697	5.12
F5	Mean	3.81×10^{-4}	0.28	8.75	20.42	18.3
	SD	2.1×10^{-4}	0.302	3.35	7.217	11.32
F6	Mean	-1.807	-1.538	-1.725	-1.484	-1.24

	SD	2.22×10^{-2}	0.377	0.083	0.352	0.689
F7	Mean	-186.72	-181.45	-174.92	-153.26	-131.34
	SD	4.46×10^{-2}	15.56	8.97	33.95	74.701
F8	Mean	3.002	8.512	3.717	6.266	5.245
	SD	3.3×10^{-3}	9.682	1.189	4.328	5.184
F9	Mean	9.59×10^{-6}	0.334	0.307	0.490	0.311
	SD	2.03×10^{-5}	0.588	0.436	0.609	0.540
F10	Mean	5.51×10^{-13}	0.102	8.47×10^{-13}	-0.062	0.067
	SD	1.69×10^{-12}	0.191	2.86×10^{-12}	0.137	0.158
F11	Mean	1.06×10^{-6}	0.238	1.265	0.314	0.2916
	SD	4.61×10^{-6}	0.488	1.203	0.361	0.391
F12	Mean	2.27×10^{-11}	0.061	1.930	1.135	0.967
	SD	9.87×10^{-11}	0.745	1.763	0.504	0.6015
F13	Mean	2.7×10^{-4}	$9.5*10^{-2}$	0.802	2.64	2.4576
	SD	2.79×10^{-4}	0.108	0.441	1.82	2.0736
F14	Mean	-3.844	-3.492	-3.545	-3.29	-2.8137
	SD	0.022	0.380	0.224	0.405	1.5017
F15	Mean	9.4×10^{-5}	0.485	3.31	3.949	2.8512
	SD	1.53×10^{-4}	0.474	2.109	3.138	3.004

3.2.2. Experimental Setup

The effectiveness of the proposed EEMD technique will be examined in this section by systematic experimental tests corresponding to different IM BRB and operating conditions. Fig. 3.4 shows the experimental setup used in this test. The tested IMs (Marathon Electric, model 056T34F5301) are rated at 1/2HP (0.372KW). These three-phase IMs have 34 rotor bars and 24 stator slots. The experimental data for analysis is collected at line frequencies of 50 Hz and 60 Hz. A variable frequency drive (VFD) with a switching frequency of 15 kHz is used to control and change the line frequency and the speed of the IM from 300 rpm to 3600 rpm. A dynamometer is used to apply load torque on the IM. Three split-core current transformers (Nidec Copal Electronics, model C-CT-16) based smart sensors are used to collect the line current data. The collected current signals are wirelessly transmitted to the receiver and the processing computer.

There are four tested IM conditions: healthy, one broken bar, two broken bars, and three broken bars. The tests are undertaken under four load conditions: no load when the IM shaft is decoupled from the gearbox, light load, medium load, and full load, as summarized in Table 3.3.

Fig. 3.4 Experimental setup [2]: (1) Smart current sensors; (2) IM; (3) Vibration sensor; (4) Power supply with VFD; (5) Elastic coupling; (6) Gearbox; (7) Dynamometer; (8) DC supply for dynamometer; and (9) Enclosure.

Table 3.3 Speed and Slip of IMs at Different Operational Conditions

Loading	60 Hz (3600 rpm) operation		50 Hz (3000 rpm) operation	
	Speed (rpm)	Slip (%)	Speed (rpm)	Slip (%)
No load (0% of full load)	3586	0.4	2988	0.4
Light load (33% of full load)	3546	1.5	2946	1.8
Medium load (67% of full load)	3520	2.2	2928	2.4
Full load (100% of full load)	3499	2.8	2910	3.0

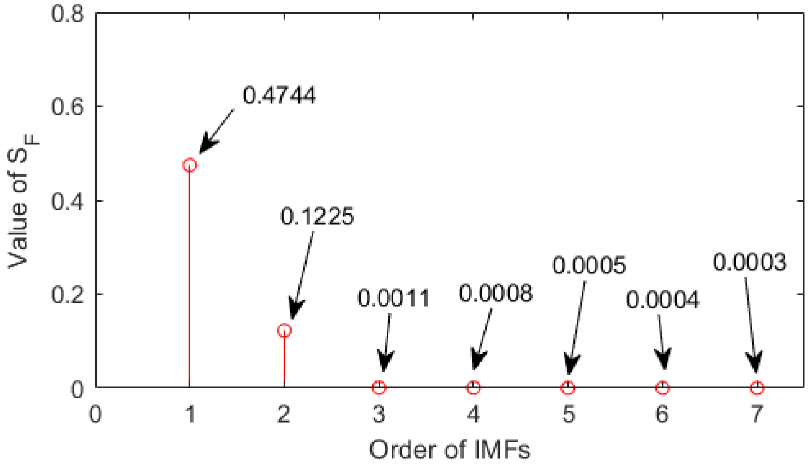

Fig. 3.5 S_F between benchmark signals and IMFs of the collected current signals at rated load for healthy condition

3.2.3 Experimental Results and Analysis

To implement the proposed EEMD technique, it is necessary to estimate the threshold value of $\Delta S_{F\text{-}u}$ in Equation (3.7). To estimate the threshold value of $\Delta S_{F\text{-}u}$, the first seven IMFs are determined and analyzed for the rated loading and different health states of IMs. For example, Fig. 3.5 indicates the values of S_F for the first seven IMFs for an IM with the slip of 2.8% and healthy condition. It is seen that the value of S_F is maximum for IMF_1 in each case, and the value of S_F decreases with the increase in IMF order. This signifies that IMF_1 has incorporated the fundamental line frequency, the corresponding sidebands, and their associated energy. It is also observed that the values of S_F, as well as differences of S_F between two adjacent IMFs, have decreased significantly after IMF_3. Hence, the value of $\Delta S_{F\text{-}u}$ in Equation (3.7) is selected as 7.55×10^{-3} which terminates the EEMD process after selecting IMF_3. Consequently, IMF_1, IMF_2 and IMF_3 will be selected for the spectral analysis and feature extraction to detect the faults in IMs.

In the current spectrum, the separation between two adjacent sidebands can be estimated from Equation (3.8) as $2sf_B$. Hence, this separation is minimum (0.48 Hz) for no load operation and maximum (3.36 Hz) for full load operation in this study. The value of constant β at Equation (3.9) can be over [25, 35]. However, in this study the value of β is selected considering two opposite effects. For example, if β is too high, the value of adaptive bandwidth (Δf_{ck}) is high enough (Equation (3.9)) to cross the limit of separation between two adjacent bands. Consequently, two adjacent bands will overlap. Oppositely, if β is too low the Δf_{ck} will be very low to extract the faulty features from the spectral peak of that adaptive band. As a result, the constant β at Equation (3.9) is set to 30, which gives the value of Δf_{ck} as 0.12 and 0.84 for no load and full load, respectively. Consequently, the frequency range for OAMF operation can be calculated using Equation (3.10) and (3.11) as $2 \times \Delta f_{ck}$, which is 0.24 for no load and 1.68 for full load, to avoid frequency band overlapping and extracting faulty features sufficiently from the adaptive bands in the proposed OAMF operation.

Additionally, the value of δ at Equation (3.14) and (3.15) can be over [0.05, 0.2]. In this study, the value of δ is considered as 0.1 Hz., which is less than one fourth of the minimum separation of two adjacent frequencies (0.48 Hz.) so as to avoid frequency band overlapping. Hence, the value of δ is set as 0.1. The accentuation factor α is also set considering two counter effects associated with calculating post-processing function F_P in Equation (3.28). If α is too high, the spectral peaks at sideband frequencies ($f_{ck\pm}$) may be greater than the spectral peak at f_B. On the other hand, if α is too low, the value F_P cannot represent the healthy and faulty conditions effectively since F_P is estimated considering the spectral peaks at $f_{ck\pm}$ and f_B, respectively

(Equation (3.28)). Considering the factor discussed here, the optimized value of α is selected for this study. The proposed MWOA technique is applied to optimize the post-processing function F_P in Equation (3.28) in terms of the value of α. Hence, the optimized value of α is found as approximately 1.2, which signifies 20% accentuation is applied. When analyzing the spectra collected at different loading and BRB fault condition, it is found that at a specific loading condition, the BRB fault has a stronger effect on the spectral peak at first characteristic frequency ($f_{c1\pm}$). However, the effect of the BRB fault is less clearly visible on the other sideband characteristic frequencies ($f_{c2\pm}$ and $f_{c3\pm}$), and the effect decreases with the increase of order (k) of $f_{ck\pm}$. Hence, the scaling factor (ρ_k) is adjusted adaptively, which is set as 1.0, 0.5 and 0.2, respectively, for $k = 1$, 2 and 3 to detect the fault more effectively from the post-processing fault function, as described in Equation (3.28).

Fig. 3.6 shows the spectra of the MCSA of IM at the speed of 3546 rpm ($s = 1.5\%$), both before and after applying the OAMF operation. It is observed from Fig. 3.6 that the fault representative features and the characteristic sidebands can be clearly identified due to the use of an adaptive spectral window to select the sideband characteristic frequencies.

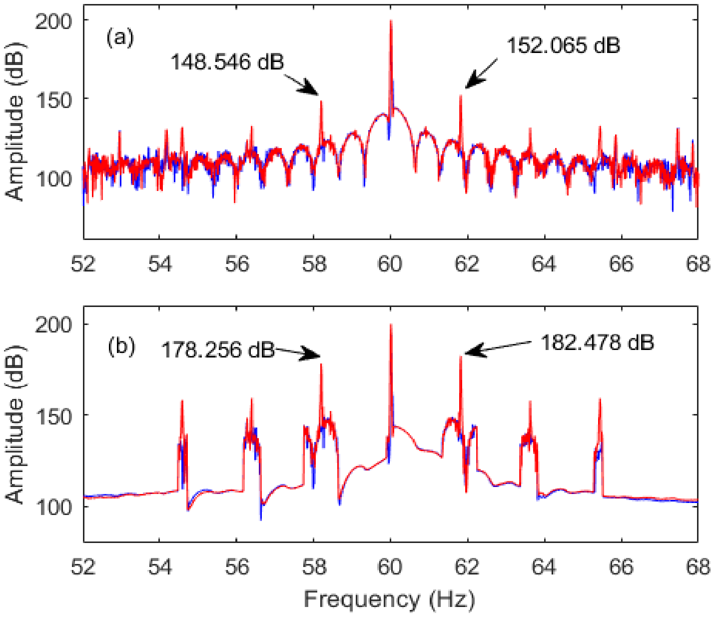

Fig. 3.6 Stator current spectra of IM with healthy and 3 BRB conditions: (a) without applying OAMF operation; (b) applying OAMF operation (Blue line: healthy; Red line: 3 BRB).

Fig. 3.7 represents the spectra of MCSA of IM considering healthy and 3 BRB conditions at different speed conditions, which is represented by the value of slip (s), as presented in Table 3.3. Analyzing Fig. 3.7, it is evident that the proposed EEMD technique can distinguish the BRB fault at different speed conditions. Likewise, the performance of the EEMD technique is also justified at different fault conditions, keeping the speed of IMs fixed at different levels.

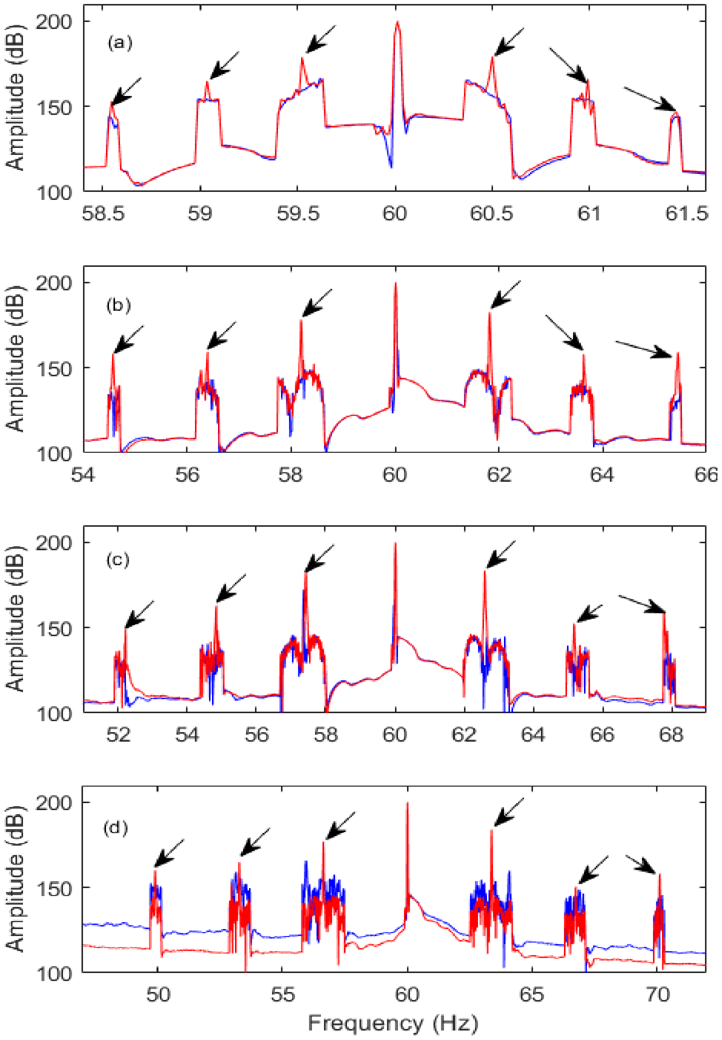

Fig. 3.7 Spectra for IMs for healthy and 3 BRB conditions applying proposed EEMD technique at different loading (or slip) conditions: (a) no load (slip= 0.4%); (b) light load (slip=1.5%); (c) medium load (slip=2.2%); (d) full load (slip (2.8%) operating at 60 Hz line frequency (Blue line: healthy; Red line: 3 BRB).

Fig. 3.8 represents the corresponding spectra of current at 3546 rpm of operational speed (slip = 1.5%) for different IM BRB conditions. It is evident that the spectral magnitude at the fault characteristic frequencies increases with the increasing of BRB in IMs, which also indicates, increased , fault severity. Thus, the proposed EEMD technique is effective in estimating the fault severity because the increase of BRB will affect more operating cycles in the machine. For example, the IMs used in this experimental analysis have 34 rotor bars. Therefore, one broken bar in IMs affects 1/34 of an operating cycle, whereas three broken bars affect 3/34 of an operating cycle. Accordingly, the spectral magnitudes at fault characteristic frequencies are also anticipated to increase with the increased number of BRBs or the severity of fault in the IM.

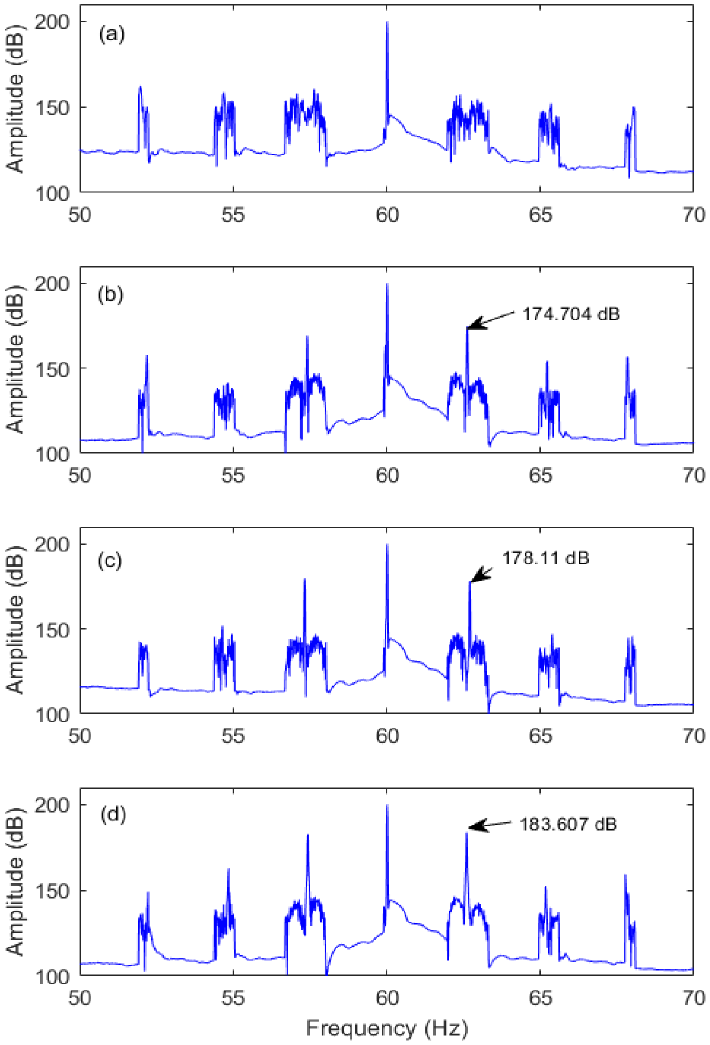

Fig. 3.8 Current spectra for IMs for (a) healthy; (b) 1 BRB; (c) 2 BRB; (d) 3 BRB conditions at slip=1.5%

The spectra of MCSA of IMs for healthy and 3 BRB conditions applying EEMD technique at 60 Hz and 50 Hz line frequencies for full load (3499 rpm vs 2910 rpm) is shown in Fig. 3.9. It is clear that the proposed EEMD technique can also effectively detect the BRB fault at 50 Hz operating frequency of IMs.

Furthermore, as the EMD-based decomposition technique is used to generate the selective IMFs for further processing in the proposed EEMD technique, the efficacy of the proposed technique is investigated in comparison with three related techniques in the literature as:

Technique 1 (T_1): This technique applies the classical EMD technique and no spectral operations on IMFs generated from classical EMD [8].

Technique 2 (T_2): This technique applies variance based spectral processing technique on selected IMFs generated from EMD technique. The selection of IMFs are based on classical correlation analysis [1].

Technique 3 (T_3): This technique applies variational mode decomposition technique (VMD), which decomposes a signal into several IMFs having specific bandwidth around a central frequency [118].

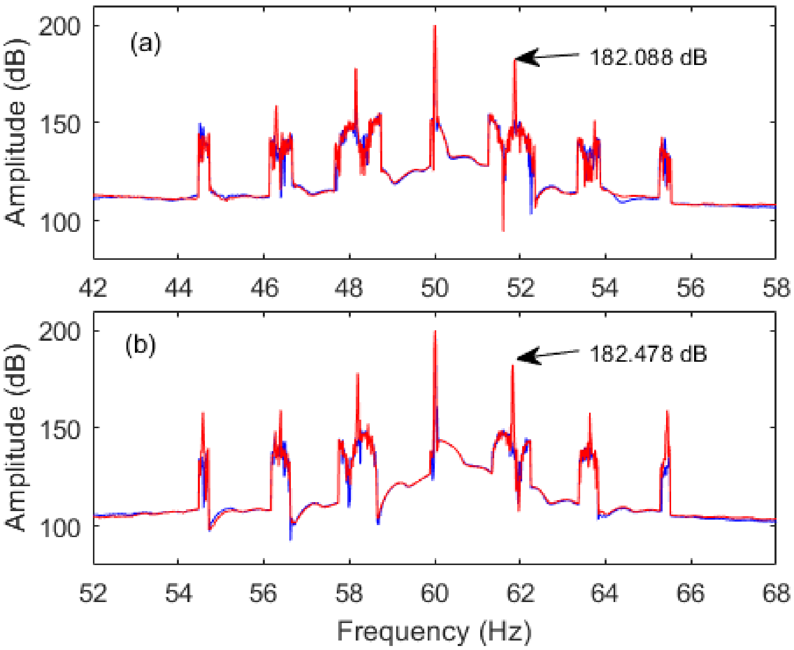

Fig. 3.9 Stator current spectra for IMs for healthy and 3 RBR conditions applying proposed EEMD technique at: (a) 50 Hz line frequency and slip=1.8%; (b) 60 Hz line frequency and slip=1.5% (Blue line: healthy; Red line: 3 BRB).

The comparative performance analysis of the related techniques in terms of the post-processing function (F_P and F_I) at different speed conditions and 60 Hz operational frequency is presented in Fig. 3.10. The higher values of F_P and F_I will specify more severe faults and vice versa. Observing Fig. 10(a), it is evident that T_1 cannot correctly recognize differences between 1 BRB and 2 BRB faults at low, medium or full load. Additionally, T_2 cannot clearly differentiate 1BRB and 2 BRB faults at medium or full load (Fig. 3.10(b)). Similarly, T_3 cannot accurately distinguish the 1 BRB and 2 BRB faults at no load or medium load (Fig. 3.10(c)). On the contrary, the proposed EEMD technique can distinguish all types of faults clearly at different load conditions, which is evident from Fig. 3.10 (d). Fig. 3.11 presents the comparative performance analysis among these techniques while the IMS are operating at 50 Hz of line frequency. It is observed from Fig. 3.11(a) that T_1 cannot clearly separate the faults of 1 BRB, 2 BRB or 3 BRB at low load, nor the faults of 1 BRB or 2 BRB while operating at medium load. Furthermore, T_2 cannot distinguish 1 BRB and 2 BRB faults effectively at low load (Fig 3.11(b)). In addition, T_3 cannot effectively differentiate 1 BRB or 2 BRB faults at no load, nor at low load (Fig. 3.11(c)). However, as presented in Fig. 3.11(d), the proposed EEMD technique can clearly differentiate the faults and severity in all conditions.

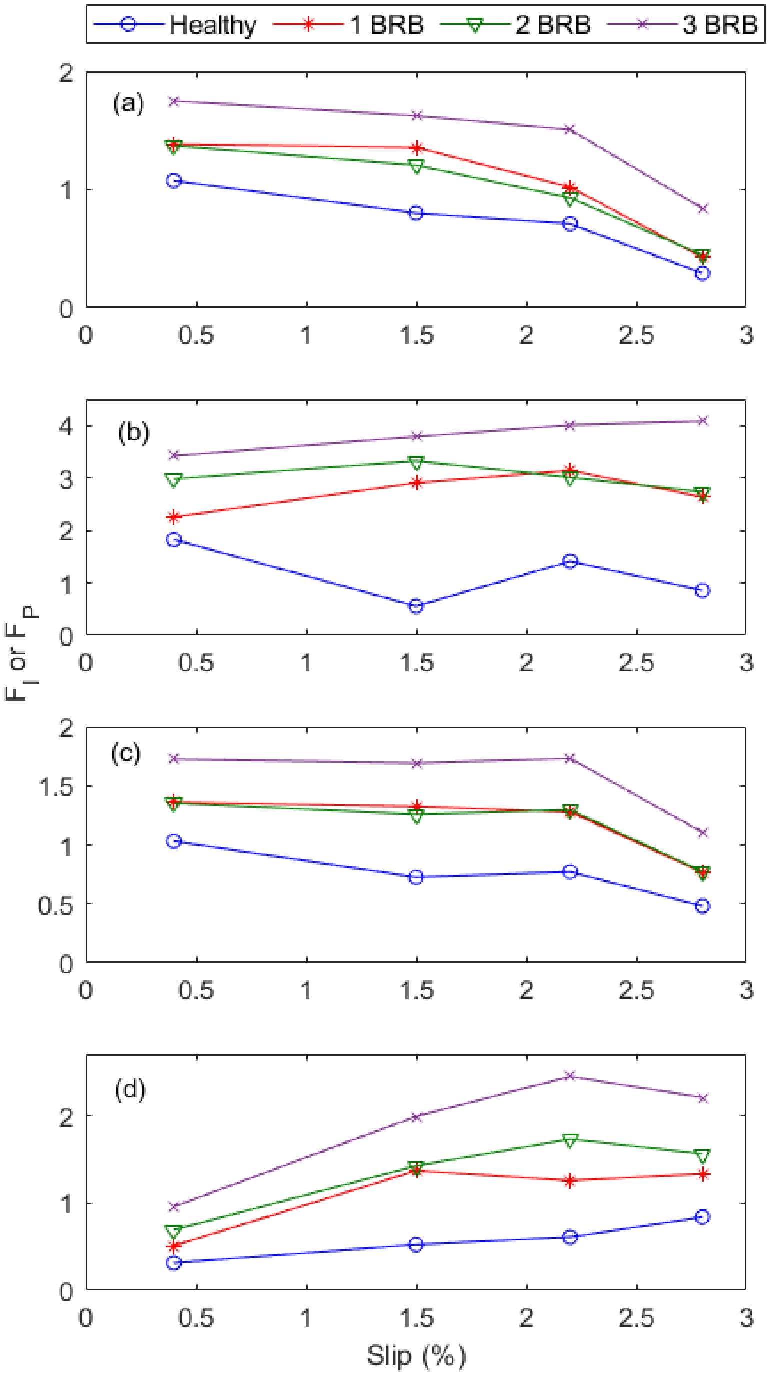

Fig. 3.10 Performance comparison of the related techniques at 60 Hz: (a) T_1; (b) T_2; (c) T_3; (d) proposed EEMD under different speed and fault conditions.

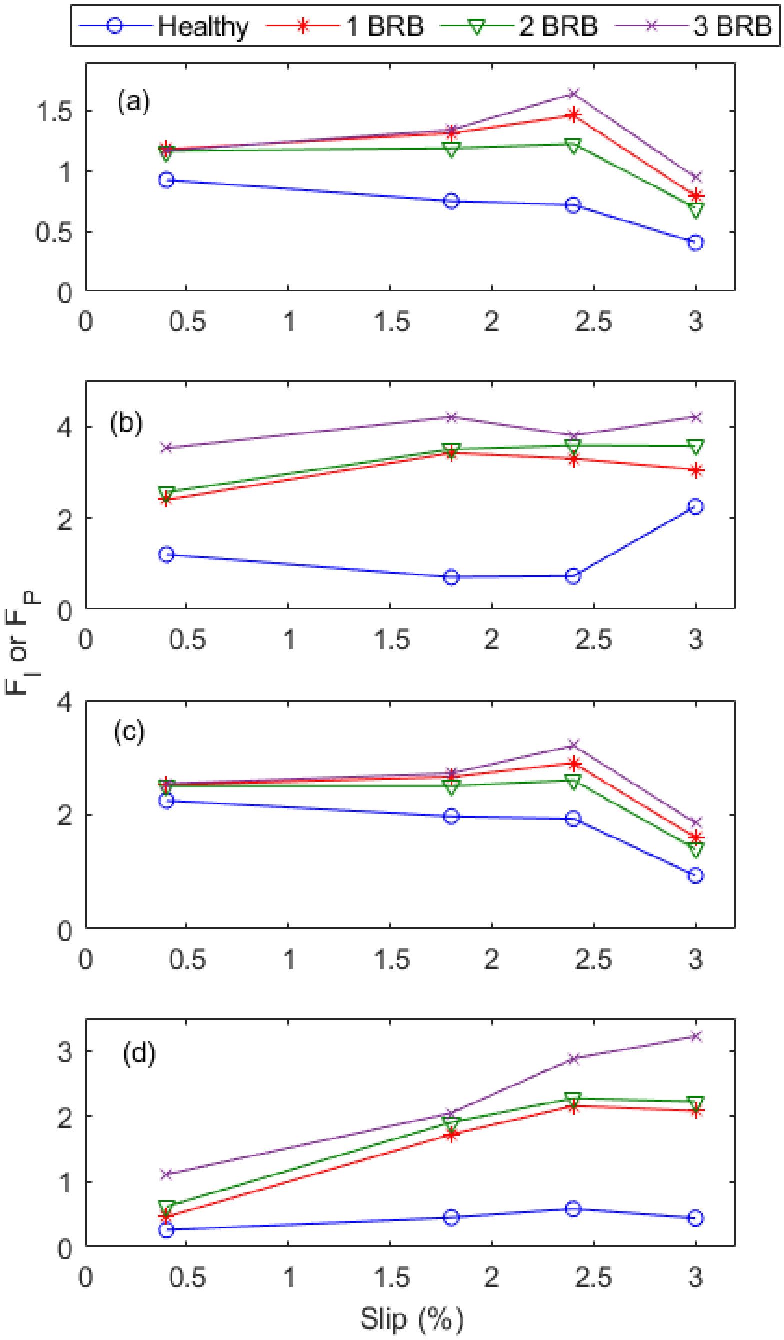

Fig. 3.11 Performance comparison at 50 Hz applying the related techniques: (a) T_1; (b) T_2; (c) T_3; (d) proposed EEMD under different speed and fault conditions

Table 3.4 summarizes the average computational time of EEMD and the related EMD techniques considering different IM load states and at healthy and 3 BRB conditions. From Table 3.4 it is evident that the proposed EEMD technique is more efficient in computation than the related EMD techniques. The classical EMD technique uses more time in computation as it continues generating IMFs until a monotonic residue is achieved, whereas the proposed EEMD technique uses the selective IMFs for processing only, which makes it suitable for real-time IM condition monitoring and fault diagnosis.

Table 3.4. Average Computational Time for EEMD and Classical EMD Technique

Loading condition	Health states	Computational time (millisecond) for EEMD	computational time (millisecond) for EMD
No load (slip=0.4%)	Healthy	12.78	37.72
	3BRB	13.24	38.62
Light load (slip=1.5%)	Healthy	14.21	36.12
	3BRB	14.26	37.54
Medium load (slip=2.2%)	Healthy	13.82	43.06
	3BRB	14.65	43.17
Full load (slip=2.8%)	Healthy	16.87	46.91
	3BRB	17.04	47.58

The effectiveness of the F_P is also investigated in comparison of the generally used F_I in the literature [1], [6]. The comparative analysis of the F_P versus F_I at 60 Hz is presented in Fig. 3.12. It is evident from Fig. 3.12 that the F_I cannot effectively distinguish 1 BRB or 2 BRB faults at low, medium and full load conditions, whereas the suggested F_P can distinguish the faulty condition effectively at all speeds (or slip) conditions. Additionally, Fig. 3.13 presents the test results at 50 Hz operating condition of IMs. From Fig. 3.13 it can be concluded that the F_P can successfully detect faults at all speed or slip conditions (Fig. 3.13(b)), however the F_I cannot accurately predict faulty conditions at low, medium and full load conditions (Fig. 3.13(a)).

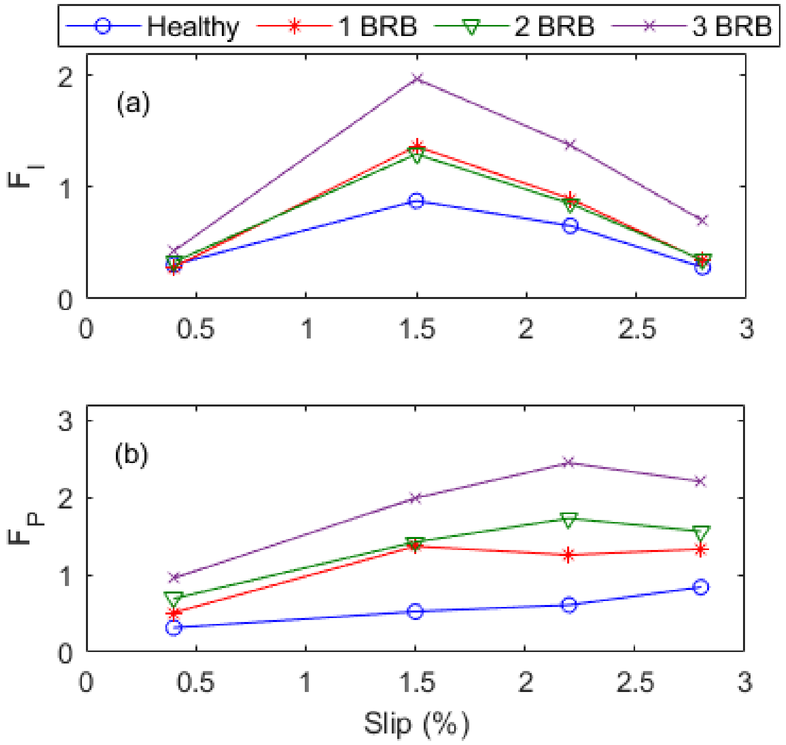

Fig. 3.12 Effectiveness analysis of F_P and F_I at different speed and fault conditions while operating at 60 Hz: (a) F_I; (b) F_P

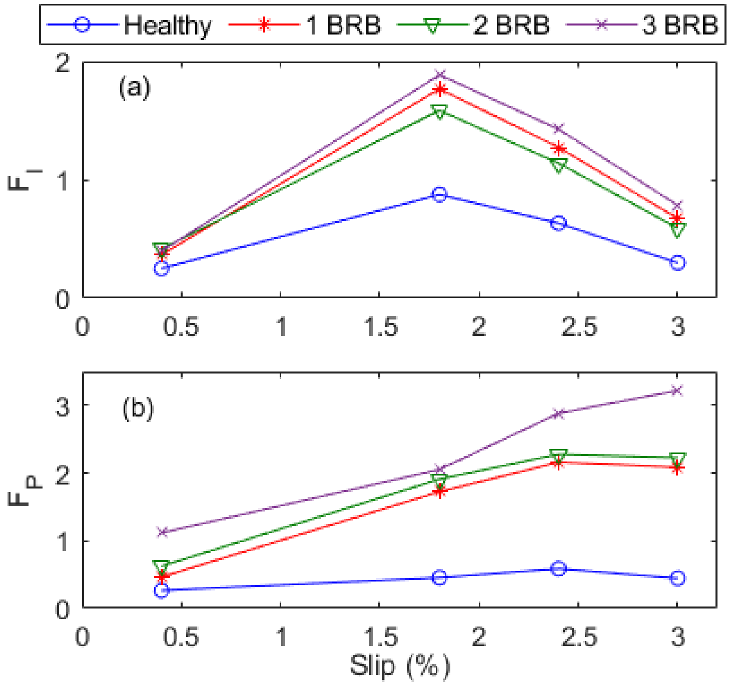

Fig. 3.13 Effectiveness analysis of F_P and F_I at different speed and fault conditions while operating at 50 Hz: (a) F_I; (b) F_P

3.2.4 Test Analysis in Different Noisy Conditions

To investigate the effectiveness of the proposed EEMD technique at noisy conditions, white gaussian noise is added to the collected current data considering two different levels of signal-to-noise ratio (*SNR*) as SNR_1= 45 dB and SNR_2= 30 dB.

Furthermore, the value of F_P is calculated for the noisy current signals after applying proposed EEMD technique on the datasets. Figs. 3.14 and 3.15 represent the value of F_P in different loading and BRB conditions at 60 Hz and 50 Hz of line frequency at noisy conditions. From Fig. 3.14, it is observed that at 60 Hz, the proposed technique can clearly detect the fault in all loading and faulty situations for the noisy current signal having SNR_1=45 dB and SNR_2=30 dB, respectively. Similarly, at 50 Hz operational condition (Fig. 3.15), although the values of F_P are closer to one another at no load (slip = 0.04%) condition, the value of F_P increases systematically with the increasing number of BRB (fault severity). However, in other operating conditions (slip or speed) the proposed technique can detect the fault effectively at both levels (SNR_1 and SNR_2), respectively. Therefore, it can be concluded that the proposed EEMD is also effective in detecting the BRB fault in noisy conditions.

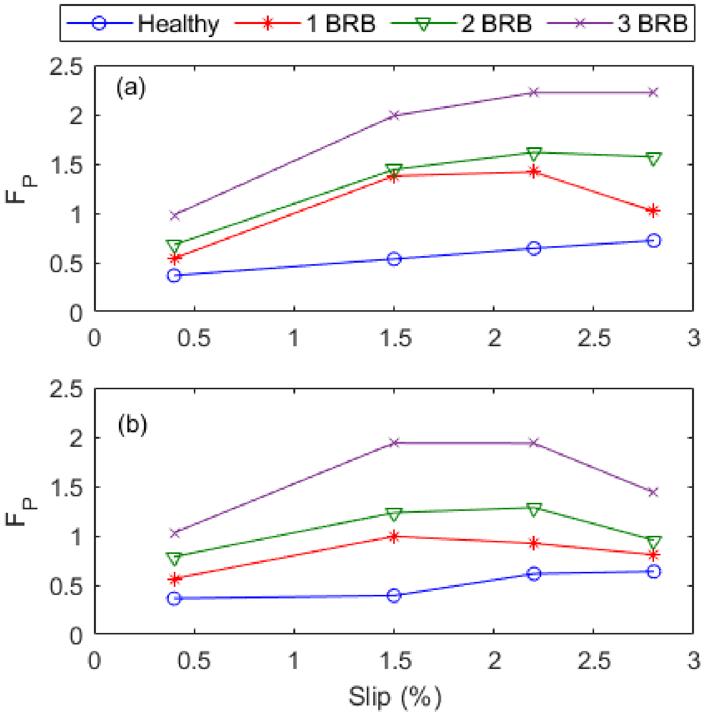

Fig. 3.14 The value of F_P at 60 Hz applying EEMD of IM at (a) SNR_1 (b) SNR_2

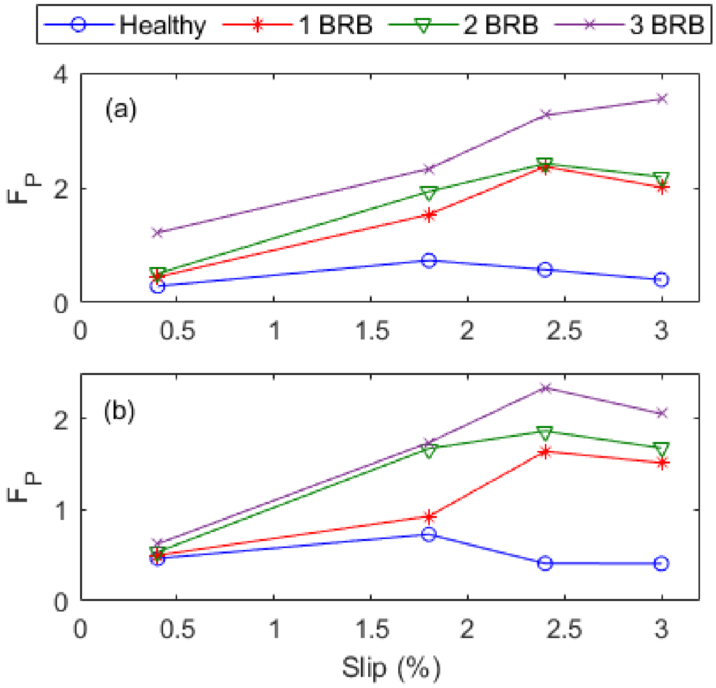

Fig. 3.15 The value of F_P at 50 Hz applying EEMD on MCSA of IM at (a) SNR_1 (b) SNR_2

3.3 Chapter Conclusion

An OAMF-based EMD technique has been presented and analyzed in this chapter considering the MCSA of the IM. This proposed technique can effectively detect the BRB fault by identifying the sideband frequencies more clearly in the current spectrum. This method applies a new similarity function (S_F) to select the targeted IMF for spectral analysis. Furthermore, the proposed OAMF operation has been applied, which can alter its bandwidth considering the speed and order of the sidebands and can detect the characteristic sidebands around the fundamental frequency more distinctly. As the OAMF operation has been conducted on spectrum of current signal, it has not been required to reconstruct the time domain signal. Moreover, a MWOA optimization algorithm has been proposed and utilized with the OAMF operation, which makes the OAMF capable of applying optimized accentuation to the characteristic sidebands around the fundamental frequency. The effectiveness of the MWOA has been investigated considering 15 different benchmark functions, as presented in the chapter. Furthermore, the effectiveness of the proposed OAMF-based EEMD technique has been justified considering three related techniques that incorporates EMD- and VMD-based processing techniques. The proposed post-processing function (F_P) can also effectively distinguish healthy and faulty conditions, as well as fault severity compared to the classical one, which has been verified through experimental investigation. In addition, the proposed EEMD is effective in detecting the BRB fault from noisy line current signals, which has also been verified in the chapter. From the above evidence, it can be concluded that the proposed technique is a good candidate to be applied in real-time IM health condition monitoring.

Chapter 4

Proposed Adaptive Direct Torque and Flux Control Technique

In a grid-connected DFIG WEC system, both the stator side and the rotor side of the DFIG are connected to the grid line. The stator side is directly connected to the grid, whereas the rotor side is connected through back-to-back converters, which provide the flexibility to control the system. To implement the proposed adaptive direct torque and flux (DTF) control technique for DFIG WEC system, the stator side voltages and currents are applied to determine the actual torque and flux, which are further compared to respective reference torque and flux to generate error signals. These error signals are processed to create the switching signals for RSC. Moreover, the GSC has its usual functions to control the DC link voltage and grid-reactive power using classical control schemes developed in [51].

To estimate the torque and flux of the DFIG system, first the α-β components of the stator voltages ($v_{s\alpha}$, $v_{s\beta}$) and currents ($i_{s\alpha}$, $i_{s\beta}$) are calculated from the respective a-b-c components (v_{sa}, v_{sb}, v_{sc}) and (i_{sa}, i_{sb}, i_{sc}) using Park's transformation. The α-β components of the stator flux ($\psi_{s\alpha}$, $\psi_{s\beta}$), the magnitude (ψ_s) and angle (θ_s) of the stator flux are calculated using Equation (4.1) to (4.3).

$$\psi_{s\alpha} = \int (v_{s\alpha} - R_s i_{s\alpha}) dt \tag{4.1}$$

$$\psi_{s\beta} = \int (v_{s\beta} - R_s i_{s\beta}) dt \tag{4.2}$$

$$\psi_s = \sqrt{{\psi_{s\alpha}}^2 + {\psi_{s\beta}}^2} \text{ and } \theta_s = \tan^{-1} \frac{\psi_{s\beta}}{\psi_{s\alpha}} \tag{4.3}$$

The torque can be computed by

$$T_{em} = \frac{3P}{2} \left(i_{s\beta} \psi_{s\alpha} - i_{s\alpha} \psi_{s\beta} \right) \tag{4.4}$$

where P is the number of pole pairs in the machine.

4.1 Structure of the Proposed Adaptive DTF Control Technique

Fig. 4.1 illustrates the structure of the proposed ANF-based adaptive DTF control scheme. The grid side voltages and currents are used to calculate the torque and flux for the DFIG system. Two ANF systems and a selector are designed to process the error between reference and calculated torques. The selector chooses the appropriate ANF controller considering the operational time (t_S). Firstly, the ANF system 1 (ANF-1) is chosen, which is trained to reduce the transient effects at the initial starting moment. ANF system 2 (ANF-2) is chosen and operates continuously to improve the dynamic performance of the DFIG WEC system in coping with wind speed variations. The third ANF-based system (ANF-3) is designed to process the error between the actual flux and the reference. The parameters of the DFIG, wind turbine and grid used for simulation are listed in Table 4.1.

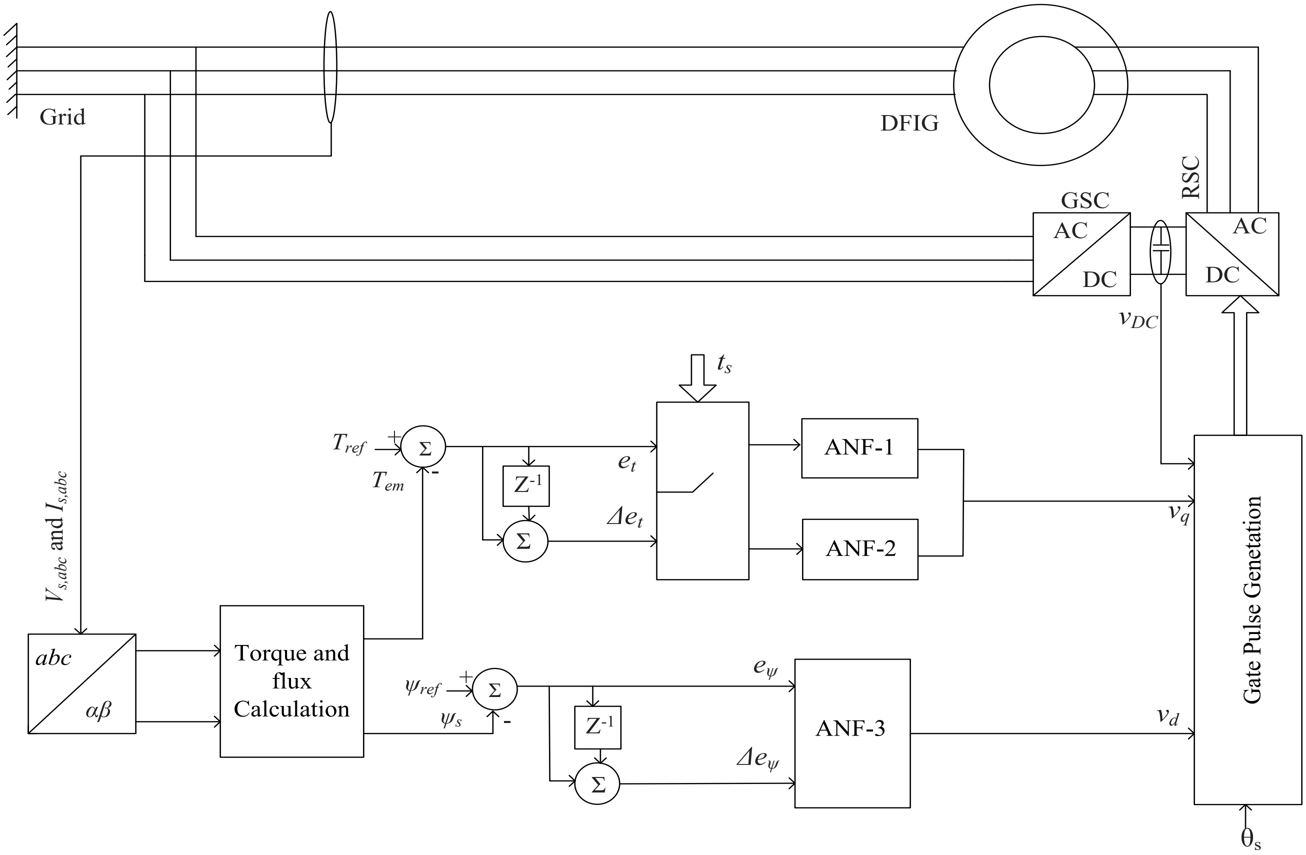

Fig. 4.1 Structure of the proposed ANF-based adaptive DTF control scheme.

Table 4.1 Simulation parameters of DFIG WEC system

Parameters	Value
Rated turbine power	1.0 MW
Pitch angle	0°
Rated generator power	1.0 MW
Grid voltage (rms)	690 V
Grid frequency	60 Hz.
Number of pole pairs	2
Leakage resistance	2.9 mΩ
Leakage inductance	0.08 mH
Magnetizing inductance	2.5 mH
Dc bus capacitance	150 mF

4.2 Configuration of the ANF Systems

The ANF system is a fuzzy inference system, except that its system parameters and output functions can be selected and updated using the training dataset. It offers more compatibility and reliability compared to traditional fuzzy systems. The configuration of the proposed ANF system is shown in Fig. 4.2. Its nonlinear membership function (MF) parameters will be optimized using the back propagation method, whereas linear consequent parameters will be updated by using the recursive least square error (LSE) technique.

The functionality of different layers of the ANF system is discussed briefly as follows:

Layer 1: This layer is the fuzzification layer. The error signal between the actual torque or flux and reference values, as well as the difference of error, are selected as inputs. Both inputs have triangular MF:

$$\mu_{Ai}(x) = \begin{cases} 0, & x \leq a_i \\ \dfrac{x - a_i}{b_i - a_i}, & a_i < x < b_i \\ \dfrac{c_i - x}{c_i - b_i}, & b_i < x < c_i \end{cases} \tag{4.5}$$

$$\mu_{Bj}(y) = \begin{cases} 0, & y \le a_j \\ \dfrac{y - a_j}{b_j - a_j}, & a_j < y < b_j \\ \dfrac{c_j - y}{c_j - b_j}, & b_j < y < c_j \end{cases} \tag{4.6}$$

where i =1, 2, 3 and j =1, 2, 3.

Layer 2: In this layer, the entering signals are processed, and individual firing strength (μ_m) is computed for each rule:

$$\mu_m = \mu_{Ai}(x)\mu_{Bj}(y) \tag{4.7}$$

where m =1, 2,……, 9

Layer 3: The rule firing strengths will be normalized in this layer, such that:

$$\bar{\mu}_m = \frac{\mu_m}{\mu_1 + \mu_2 + \cdots + \mu_9} \tag{4.8}$$

Layer 4: In this layer, the functional output is calculated as

$$f_m = \gamma_0^m + \gamma_1^m x_i + \gamma_2^m y_j, \tag{4.9}$$

The training of the consequent parameters γ_0^m, γ_1^m and γ_2^m will be discussed in the following subsection.

Layer 5: It is the output layer. The final output is calculated as

$$f_T = \bar{\mu}_1 f_1 + \bar{\mu}_2 f_2 + \cdots + \bar{\mu}_9 f_9 \tag{4.10}$$

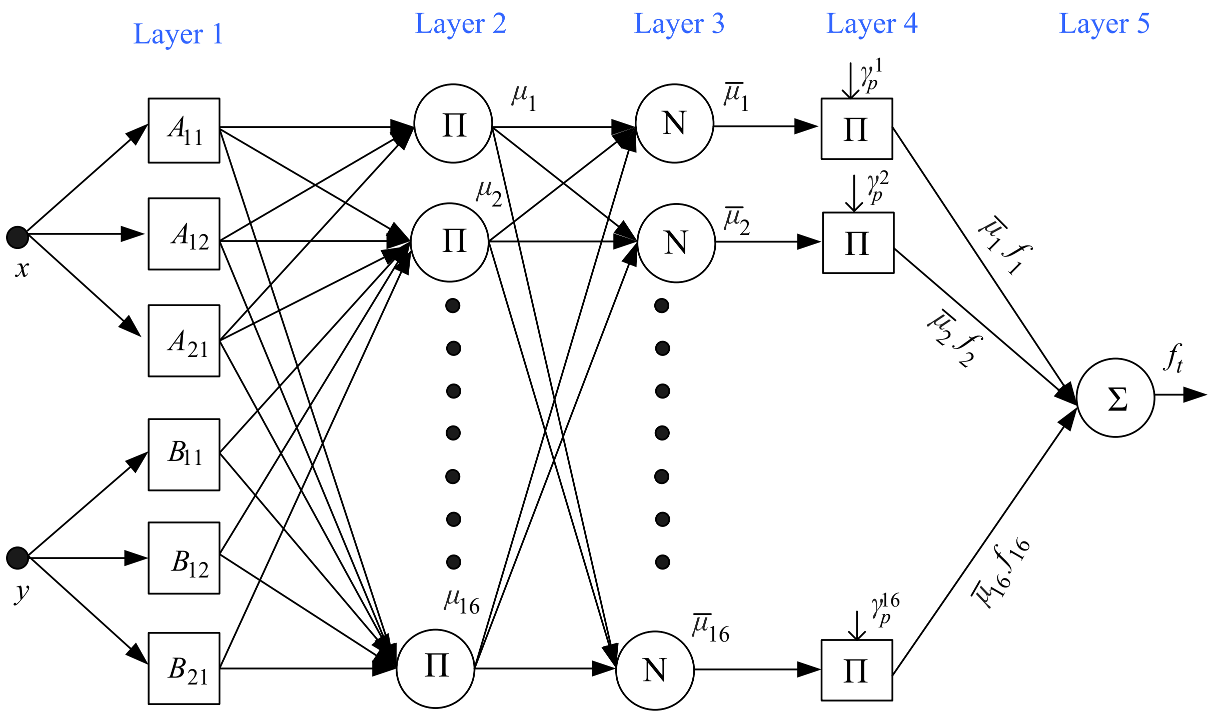

Fig. 4.2 Configuration of the proposed ANF systems.

4.3 Online Hybrid Parameter Training

The hybrid training algorithm will be applied to update the ANF system parameters. The training data of torque and flux errors are obtained from the DFIG manipulated by a PI controller. Both ANF-1 and ANF-2 are trained using the data of torque error signals. ANF-1 is trained to limit the high starting torque; ANF-2 is trained to improve system dynamic performance. ANF-3 is trained using flux error data. An initial dataset of approximately 2000 data pairs is constructed from the DFIG-based WEC system at different wind speed from 10 m/sec to 16 m/sec. Among these data pairs, about 70% of the datasets are used to train the ANF network and the remaining 30% are used for testing.

The objective function in Equation (4.11) is formulated to reduce the difference between the theoretical and calculated output data,

$$W = \frac{1}{2} e^2 = \frac{1}{2} (y-f)^2 \tag{4.11}$$

where y and f are expected and theoretical output data, respectively.

4.3.1 Optimization of Consequent Parameters

The consequent parameters $\gamma_0^m, \gamma_1^m$and$\gamma_2^m$are trained using recursive LSE method as

$$P_{k+1} = P_k - \frac{P_k a_{k+1} a_{k+1}^T P_k}{1 + a_{k+1}^T P_k a_{k+1}} \tag{4.12}$$

$$\gamma_{j,k+1}^m = \gamma_{j,k}^m + P_{k+1} a_{k+1} (y_{k+1} - a_{k+1}^T \gamma_{j,k}^m) \tag{4.13}$$

where $\gamma_{j,k+1}^m$ represents the estimate of the optimal linear parameter values.

a_{k+1} is a vector containing the coefficients of the linear parameters to be optimized.

y_{k+1} is the actual system output.

$P_o = aI$, where a is a large number, … in this case.

$\gamma_{j,0}^m$ is usually initialized to a vector of zeros.

m=1,2,….., 9 ; j= 0,1, 2; k=1, 2, …, N; N is the number of training data pairs.

4.3.2 Optimization of the Premise Parameters

The nonlinear MF parameters of proposed ANF-based controllers are trained by using the gradient decent (GD) algorithm, or

$$\begin{aligned} a_i(n+1) &= a_i(n) - \alpha_{ai} \frac{\partial W}{\partial a_i} \\ b_i(n+1) &= b_i(n) - \alpha_{bi} \frac{\partial W}{\partial b_i} \\ C_i(n+1) &= C_i(n) - \alpha_{ci} \frac{\partial W}{\partial C_i} \end{aligned} \tag{4.14}$$

where α_{ai}, α_{bi} and α_{ci} are the learning rates of the corresponding parameters and a_i, b_i and c_i are the premise parameters to be optimized, i=1,2 ,3. The derivatives can be defined using the chain rule, such as

$$\begin{aligned} \frac{\partial W}{\partial a_i} &= \frac{\partial W}{\partial f} \frac{\partial f}{\partial \mu_i} \frac{\partial \mu_i}{\partial a_i} \\ \frac{\partial W}{\partial b_i} &= \frac{\partial W}{\partial f} \frac{\partial f}{\partial \mu_i} \frac{\partial \mu_i}{\partial b_i} \end{aligned} \tag{4.15}$$

$$\frac{\partial W}{\partial c_i} = \frac{\partial W}{\partial f} \frac{\partial f}{\partial \mu_i} \frac{\partial \mu_i}{\partial c_i}$$

4.4 Stability Analysis of the Proposed ANF-based Adaptive DTF Control

After developing the ANF based DTF control the stability analysis of the WEC system is performed for theoretical verification of the overall system stability.

4.4.1 Dynamics of a Second Order System

The transfer function of a second order underdamped system can be formulated as

$$T(s) = \frac{\omega_n^2}{s^2 + 2\zeta\omega_n s + \omega_n^2} \tag{4.16}$$

where ζ is the damping ratio and ω_n is the natural frequency of the second order underdamped system.

The step response of a second order underdamped system generates damped oscillation, as its poles are in the left half portion of the *S*-plane [119]. The performance of this second order underdamped system can be evaluated by the percent overshoot (*%OS*) as

$$\%OS = \frac{C_{max} - C_{final}}{C_{final}} \times 100 \tag{4.17}$$

where C_{max} is the peak value and C_{final} is the steady state value of the output respectively.

The system parameter ζ can be determined from *%OS* [119] by

$$\zeta = \frac{-\ln(\frac{\%OS}{100})}{\sqrt{\pi^2 + \ln^2(\frac{\%OS}{100})}} \tag{4.18}$$

4.4.2 System Identification and Stability Analysis

For system identification the torque step response is obtained considering the step signal varying from 0 to 1 per unit at 1.0 sec. From this step response, the numerical value of ω_n and *%OS* are obtained to determine ζ using Equation (4.18). Table 4.2 summarizes the system parameters and estimated transfer function of the WEC system. Fig. 4.3 shows the step responses of the estimated second order system as well as the actual WEC system. It is seen that the WEC system with proposed adaptive DTF controller can be approximated to a second order underdamped system [119]. Thus, the stability of the DFIG WEC system can be demonstrated through the bode plot of the estimated second order system, as presented in Fig. 4.4. It can be seen from Fig. 4.4 that the DFIG WEC system with proposed adaptive DTF control technique is stable with a phase margin of 55.65° at a crossover frequency of 27 rad/sec.

Table 4.2 Numerical values of system parameters and transfer function of the estimated systems

Quantity	**Value**
Damping ratio (ζ):	0.5495
Natural frequency of oscillation (ω_n):	36.12 (rad/sec)
Estimated transfer function:	$\frac{1305}{s^2 + 39.7s + 1305}$
Poles of the estimated system:	$-19.85 \pm j30.18$

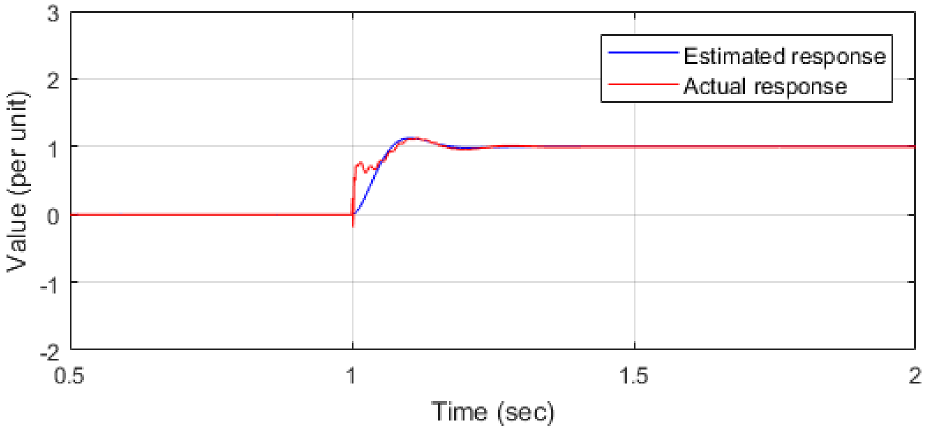

Fig. 4.3 The step response of the estimated system and the actual system

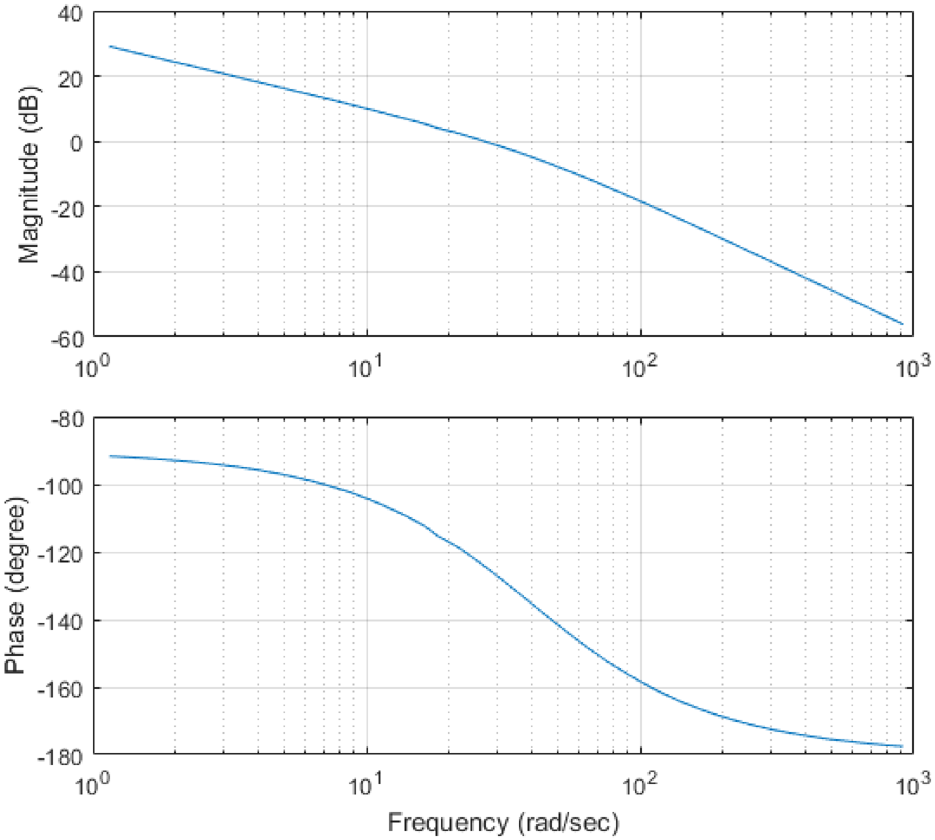

Fig. 4.4 Bode plot of the estimated system

4.5 Simulation Results and Discussions

The performance of the proposed adaptive DTF control technique is tested by simulation using MATLAB/Simulink at different DFIG WEC operating conditions. MATLAB/Simulink software is used for simulation due to its robustness and availability. The performance is compared with a classical fuzzy logic controller that also utilizes the same inputs as the proposed adaptive DTF control technique, but the fuzzy system parameters are selected by experience and not being optimized in operation. In addition, the proposed ANF based DTF control technique is compared with a PI-based classical DTF control scheme. Some typical results are presented below.

Fig. 4.5 shows the starting performance of the proposed adaptive DTF, fuzzy logic, and PI-DTF control scheme for the WEC system at a constant wind speed of 10 m/sec. From Fig. 4.5, it is found that the peak value of the starting torques reach at 6.0×10^4 and 2.3×10^4 N.m, for the fuzzy logic and PI-DTF control schemes, respectively, which are much higher that of the proposed ANF-based adaptive DTF control scheme with a peak value of 1.37×10^4 N.m. Thus, the proposed controller can significantly reduce the transient torque compared to these classical controllers. Furthermore, the proposed adaptive DTF control can reduce the transient time to 0.2 s, which is significantly faster than the fuzzy logic (0.3 sec), and PI control (0.27 sec).

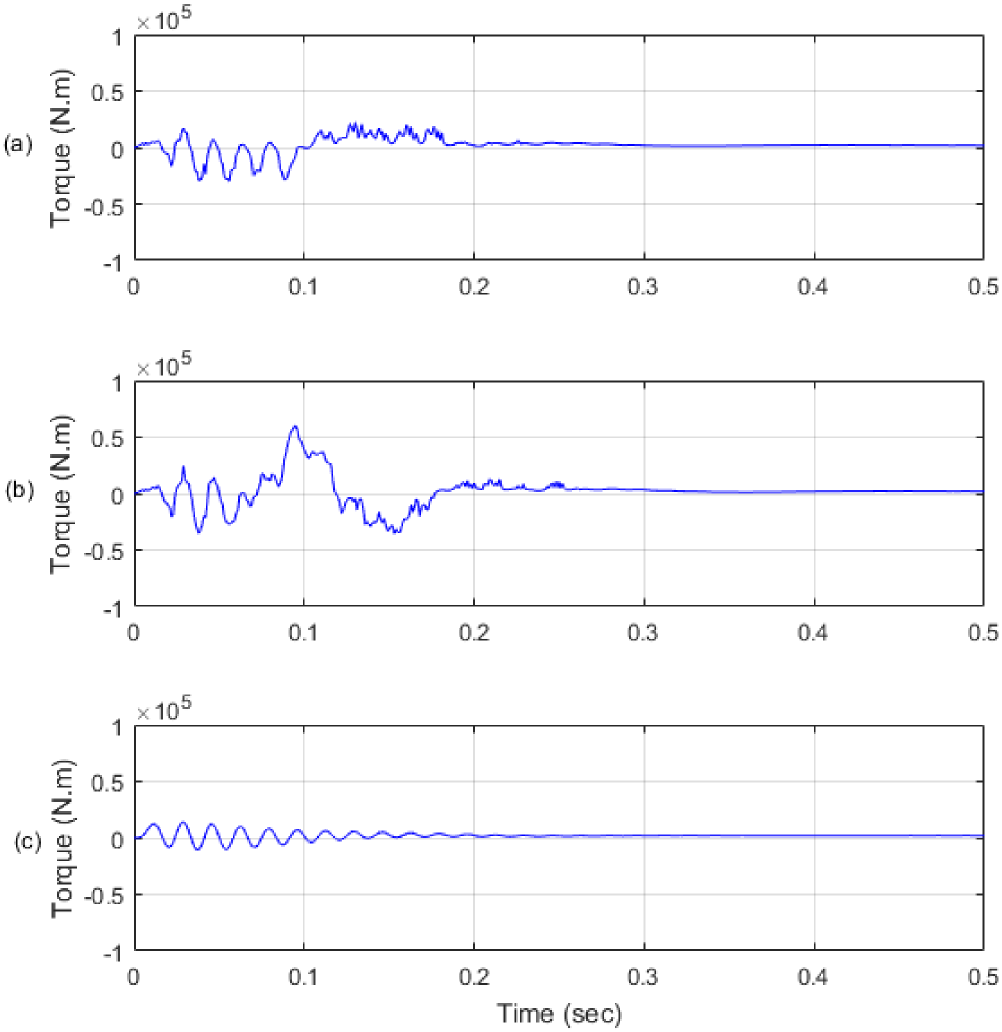

Fig. 4.5 Transient performance among the proposed PI, fuzzy and ANF-based adaptive DTF control schemes: (a) torque for PI; (b) torque for fuzzy; (c) torque for ANF.

As can be seen in Fig. 4.6, although the transient stator current peak (1.5×10^4 A) from the proposed adaptive DTF control scheme is comparable with those from both fuzzy logic and PI-DTF control schemes, the transient currents from both fuzzy logic and PI-based DTF control are more fluctuating and distorted than those from the proposed DTF control scheme. Furthermore, the proposed adaptive DTF control can significantly reduce the transient time in comparison with fuzzy logic and PI schemes (0.2 sec vs 0.35 sec).

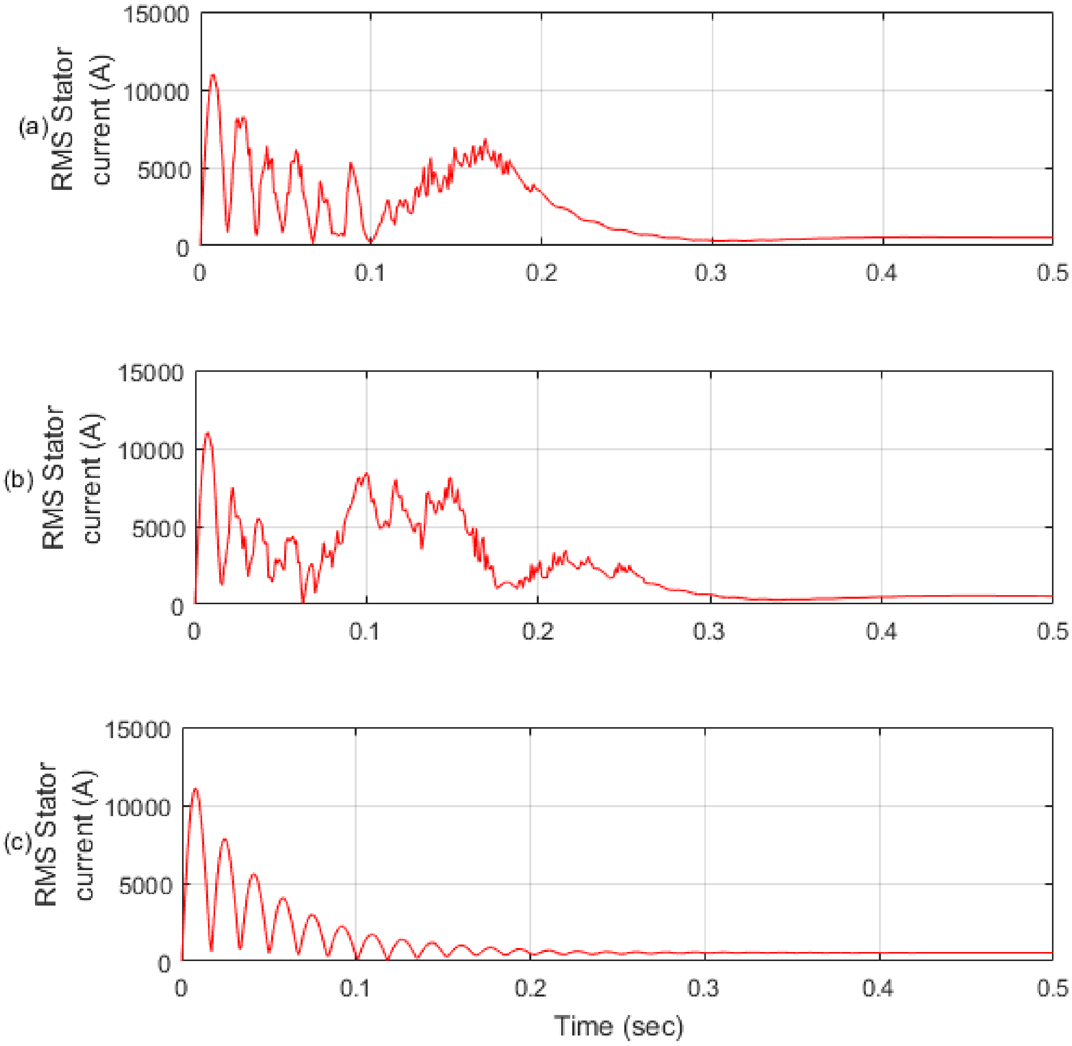

Fig. 4.6 Transient performance among the proposed PI, fuzzy and ANF-based adaptive DTF control schemes: (a) RMS Stator currents for PI; (b) RMS Stator currents for fuzzy; (c) RMS Stator currents for ANF.

Likewise, the transient performance of the rotor speed for the proposed ANF-based adaptive DTF control scheme is compared with the related control techniques and presented in Fig. 4.7. Analyzing Fig. 4.7, it is evident that the transient peak for the rotor speed is much higher for the PI and fuzzy control schemes (204.8 and 198.8 rad/sec, respectively), whereas the peak is only 189.7 rad/sec for the proposed ANF-based DTF control scheme.

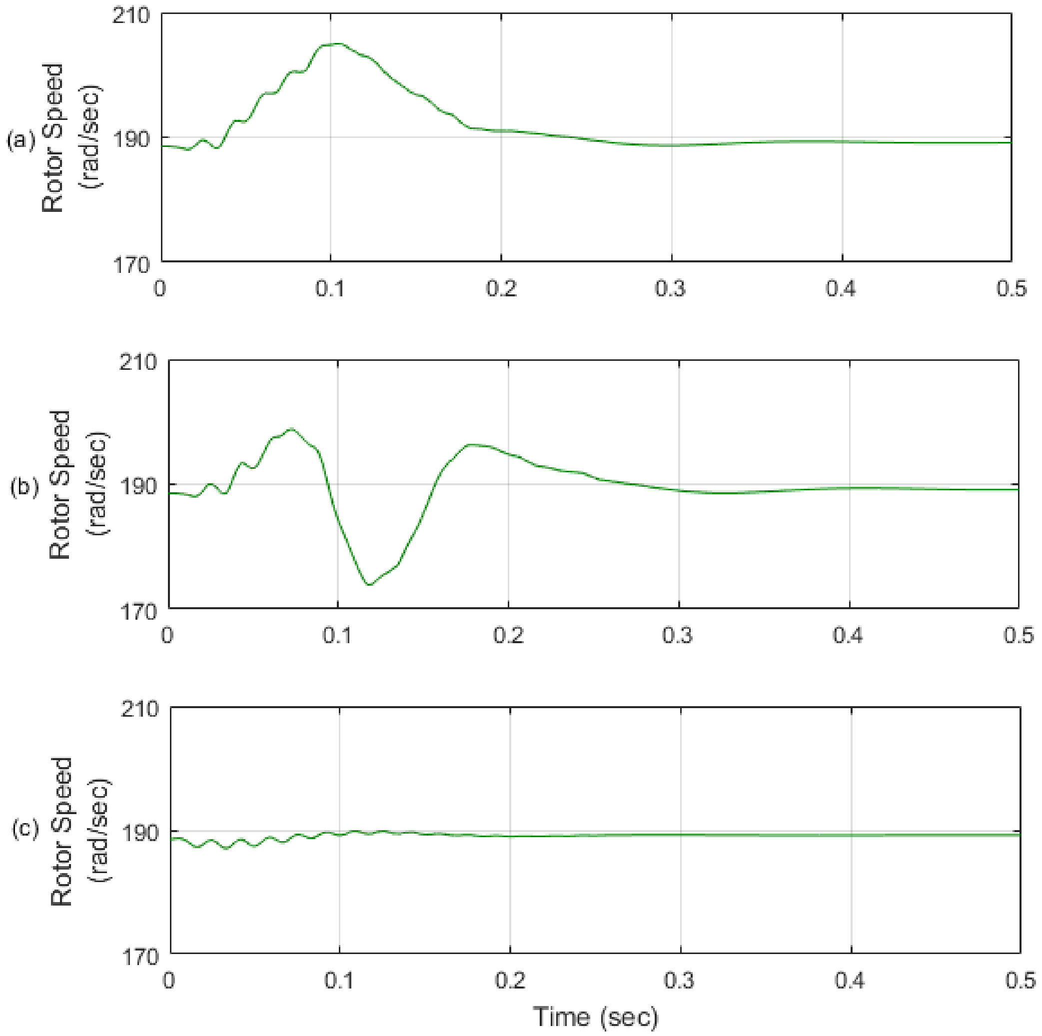

Fig. 4.7 Transient performance comparison among the proposed PI, fuzzy and ANF-based adaptive DTF control schemes: (a) rotor speed for PI; (b) rotor speed for fuzzy; (c) rotor speed for ANF.

The dynamic performance of the proposed adaptive DTF control scheme is compared with that of the fuzzy logic and PI-based schemes for a step increase in wind speed from 10 m/sec to 16 m/sec at the time of 1.0 sec. It is seen in Fig. 4.8 that the peak torque of the ANF-based control (5719 N.m) is lower than those of the fuzzy logic (5885 N.m) and PI control (5833 N.m) at the transition time of wind speed. On the other hand, the proposed adaptive DTF control can effectively reduce the *%OS* and settling time of the torque (see Table 4.3). In addition, from Fig. 4.9, it is seen that the adaptive DTF control can reduce the overshoot slightly (0.368%) for rotor speed than the fuzzy logic and PI-DTF control methods (0.421%).

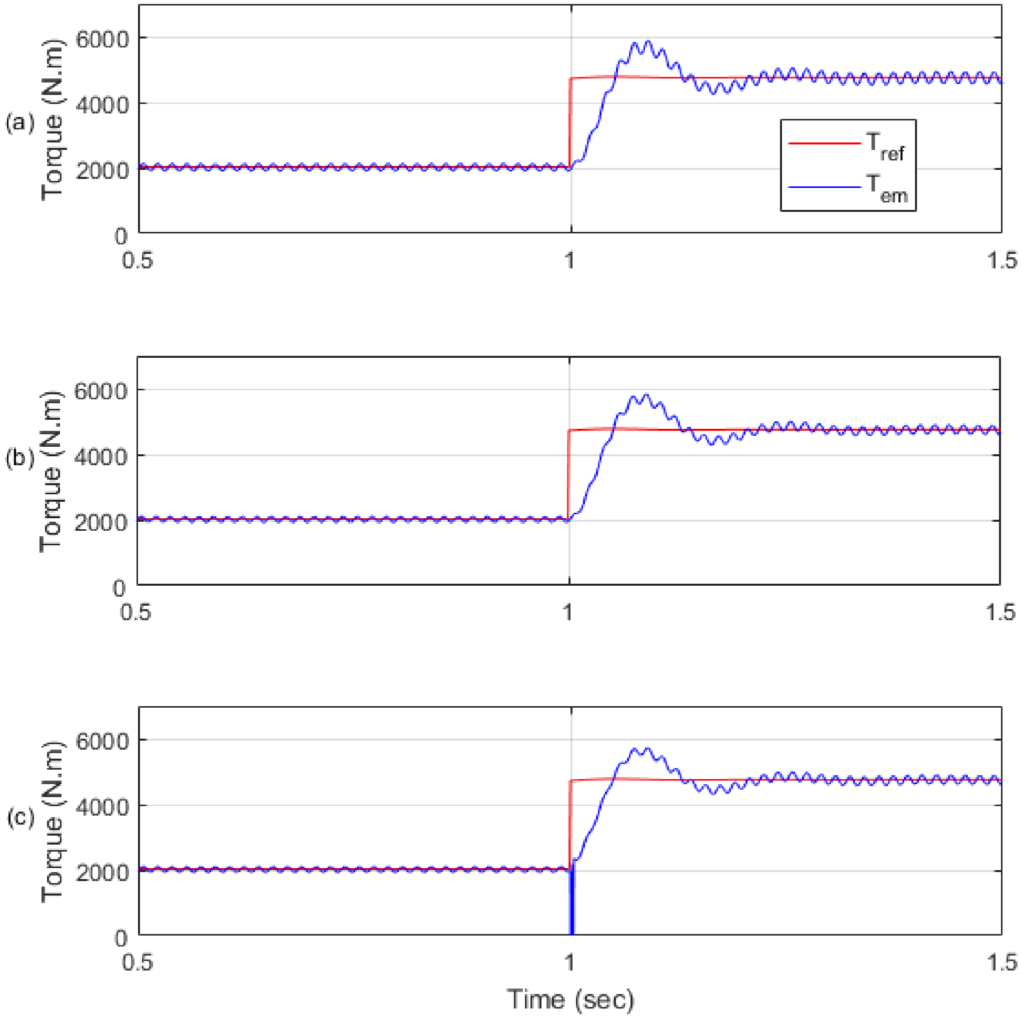

Fig. 4.8 Dynamic performance among the proposed PI, fuzzy and ANF-based adaptive DTF control schemes: (a) torque for PI; (b) torque for fuzzy; (c) torque for ANF.

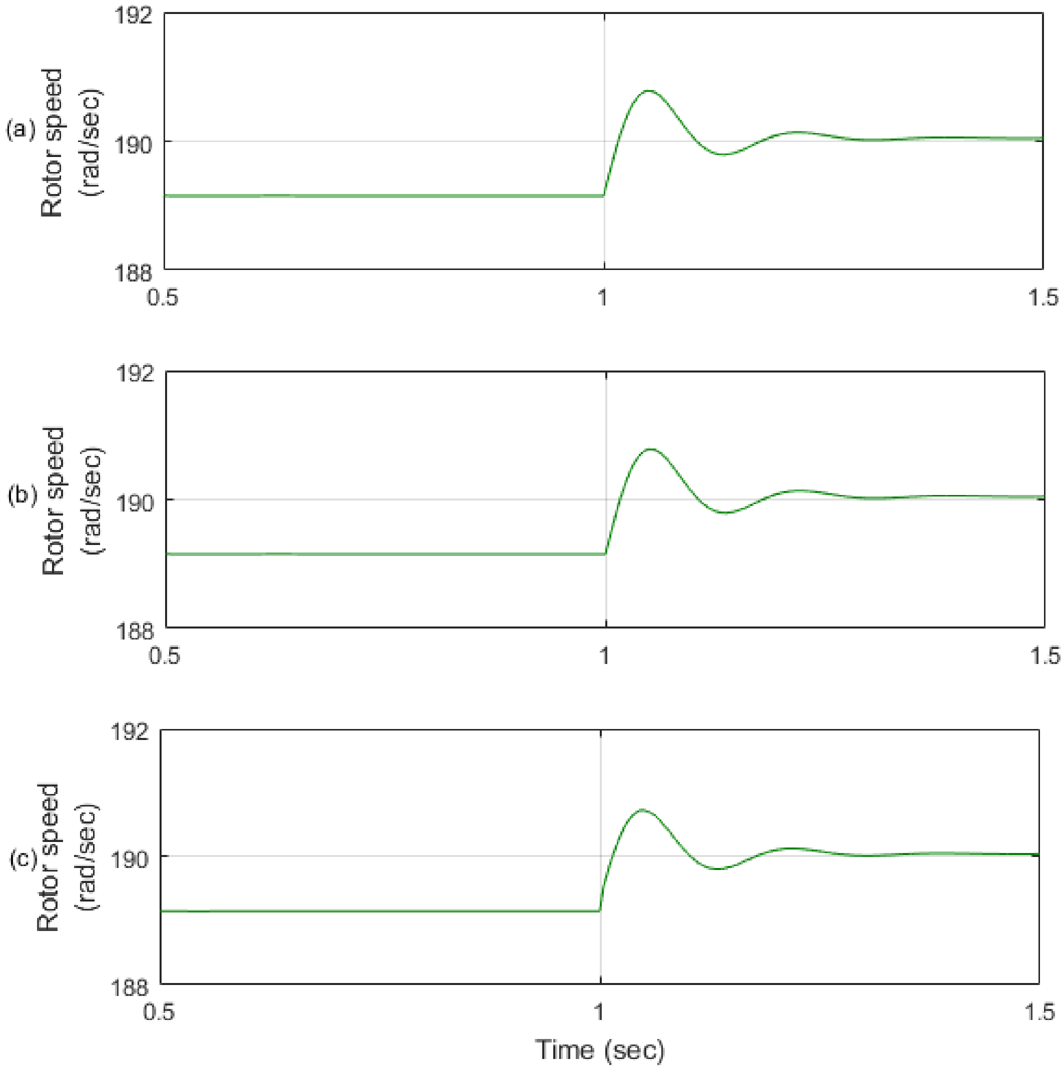

Fig. 4.9 Dynamic performance among the proposed PI, fuzzy and ANF-based adaptive DTF control schemes: (a) rotor speed for PI; (b) rotor speed for fuzzy; (c) rotor speed for ANF.

Additionally, Fig. 4.10 represents the per-phase rms of the stator current generated by applying fuzzy logic, PI and the proposed ANF-based adaptive DTF control at the moment of wind speed change, as mentioned earlier. From Fig. 4.10, it is found that the peak of stator current is significantly reduced for the proposed adaptive DTF control (1033 A) in comparison with the fuzzy logic and conventional PI-based schemes (1040 A vs 1039 A) with the wind speed variation at 1.0 sec. Table 4.3 summarizes the comparison results among the proposed adaptive DTF, fuzzy logic and PI-based schemes. It is evident that the proposed ANF-based adaptive DTF control scheme can achieve the lowest settling time and overshoot for torque and stator current responses compared to both FLC and PI control schemes.

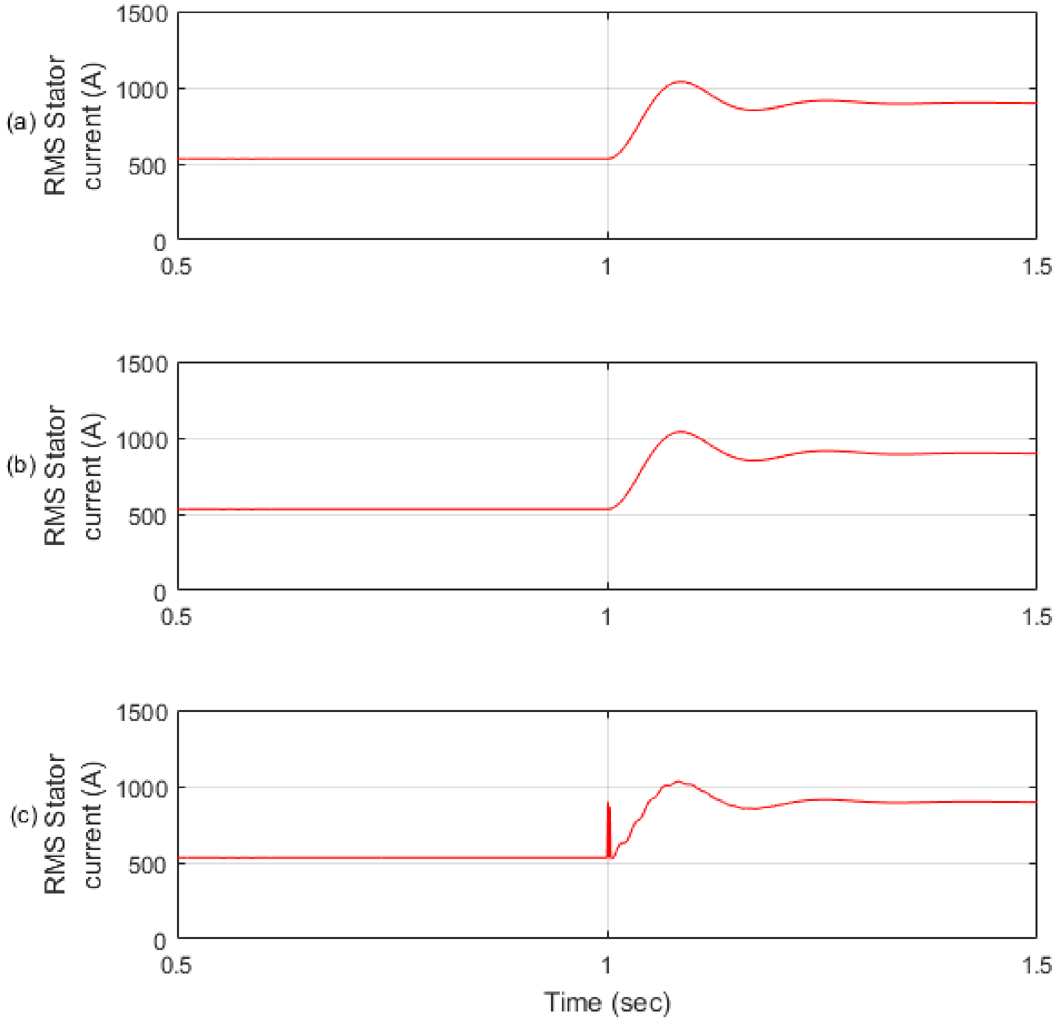

Fig. 4.10 Dynamic performance among the proposed PI, fuzzy and ANF-based adaptive DTF control schemes: a) rotor speed for PI; (b) rotor speed for fuzzy; (c) rotor speed for ANF.

Table 4.3 Comparative results among ANF, fuzzy and PI controllers

Property	**Proposed ANF-based adaptive DTF scheme**	**Fuzzy logic-based scheme**	**PI controller**
Torque settling time	0.23 s	0.28 s	0.283 s
Torque overshoot	13.2%	17.36%	20.73%
Stator current settling time	0.224 s	0.279 s	0.28 s
Stator current overshoot	12.5%	14.02%	17.98%

4.6 Real-time Implementation and Results

A laboratory prototype has been developed to examine the effectiveness of the proposed ANF adaptive DTF control of DFIG WEC system in real-time. As shown in Fig. 4.11, a 480 VA wound rotor induction machine is used as DFIG, which is connected to 208V-60Hz grid. A dynamometer (from LabVolt) is configured as a small wind turbine, which allows command from the computer. Table 4.4 summarizes the parameters and ratings of the equipment used to build the experimental prototype. A three-phase full-wave diode rectifier is used as the GSC to simplify the system structure. The control signal for RSC is generated from a DSP board (DS1104). In the experiment the wind speed is abruptly changed from 3 m/sec to 10 m/sec to examine the dynamic performance of the related control schemes. The applied reference torque varies from -2.5 N.m to 1.6 N.m according to the turbine characteristics.

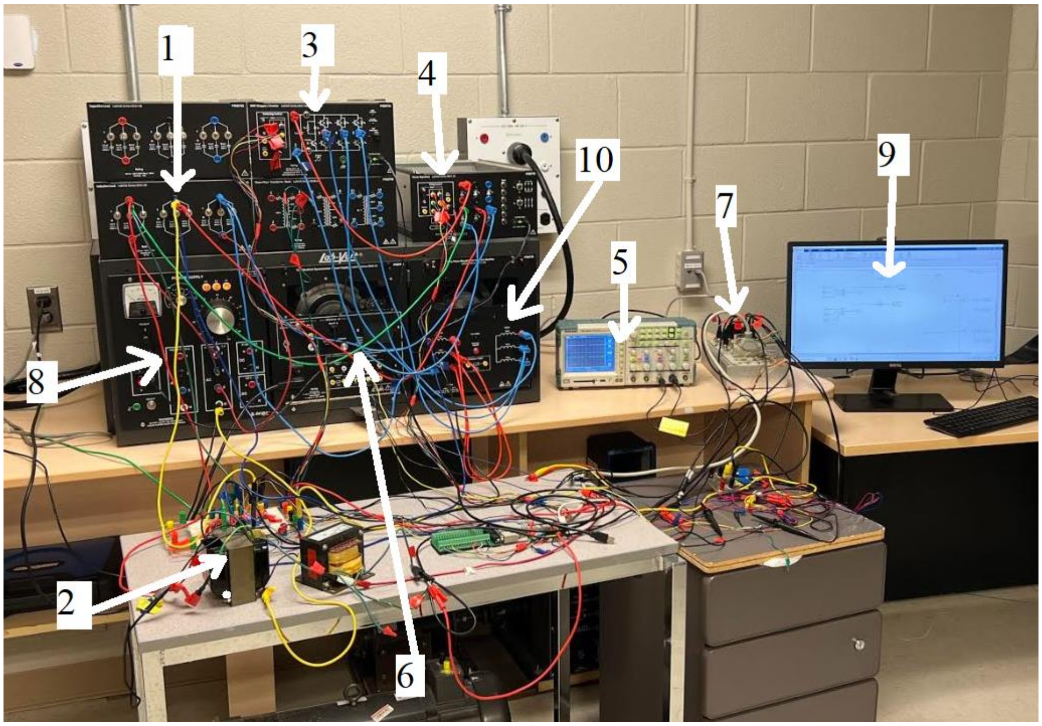

Fig. 4.11 Experimental setup for the proposed DFIG- WEC system: (1) line inductance; (2) sensors; (3) RSC; (4) grid side converter; (5) oscilloscope; (6) wind turbine; (7) DS1104; (8) grid; (9) host PC for DS 1104; (10) DFIG.

Table 4.4 Experimental parameters of DFIG WEC system

Parameters	**Value**
Rated wind turbine power	450 W
Pitch angle	0°
Rated DFIG power	480 VA
Grid voltage (rms)	208 V
Grid frequency	60 Hz.
Leakage resistance	8.10 Ω
Leakage inductance	30.0 mH
Dc bus capacitance	4.2 mF

Fig. 4.12 shows the variations of torque and stator current for the proposed ANF, fuzzy and classical PI control schemes corresponding to wind speed variations. It is evident that there is less fluctuation and overshoot of torque for the proposed adaptive DTF control scheme compared to both the fuzzy and the PI-based control schemes. Thus, it is verified that the proposed adaptive DTF control scheme can improve the dynamic performance of WEC system.

(a)

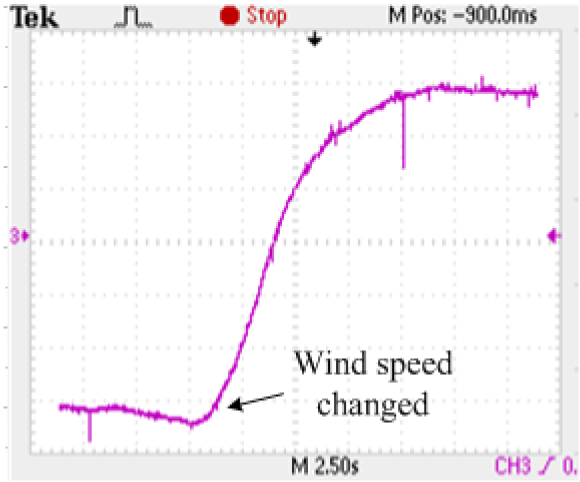

(b)

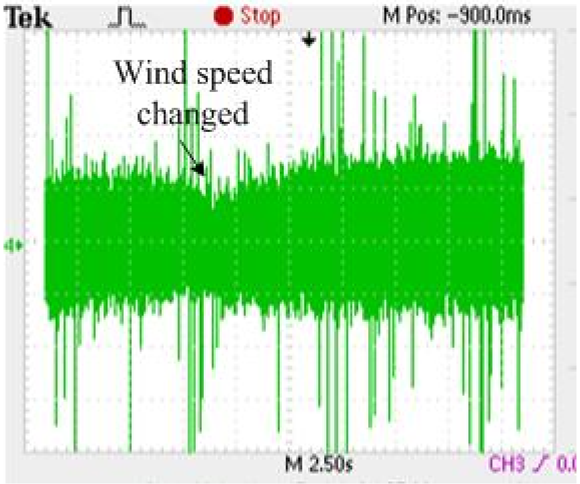
Tek
Stop
M Pos: −900.0ms
Wind speed changed
M 2.50s
CH3

(c)

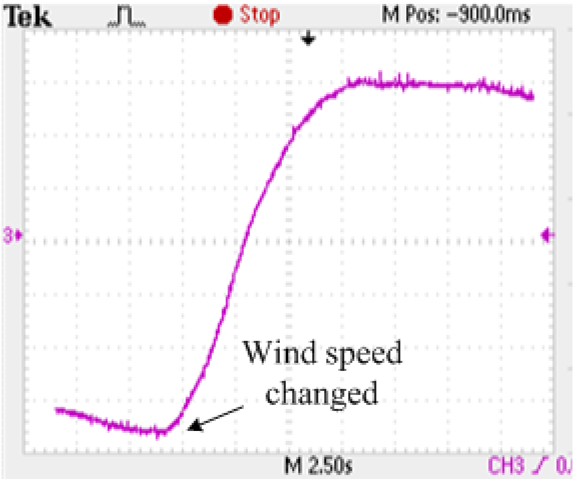
Tek
Stop
M Pos: −900.0ms
Wind speed changed
M 2.50s
CH3

(d)

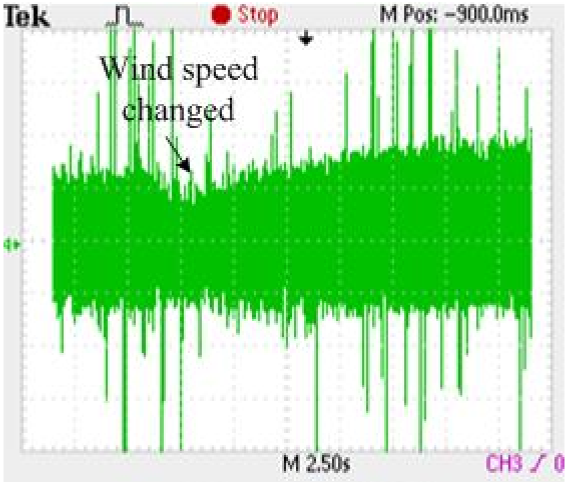
Tek
Stop
M Pos: −900.0ms
Wind speed changed
M 2.50s
CH3

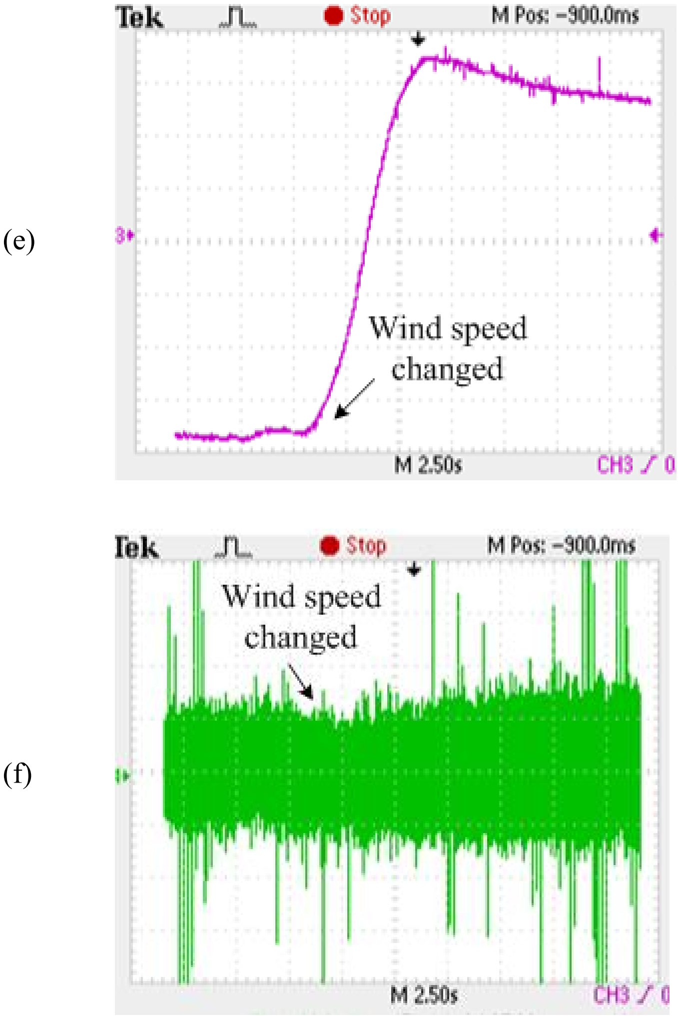

Fig. 4.12 Experimental performance of the machine torque and stator current for the wind speed variation: (a) torque for the proposed adaptive DTF control (Scale: Y axis- 1div= 1 N.m); (b) stator current for the proposed adaptive DTF control (Scale: Y axis- 1div= 0.2 A); (c) torque for fuzzy based control; (d) stator current for fuzzy based control; (e) torque for PI control; (f) stator current for PI control.

From Fig. 4.13(a), the current waveforms of DFIG remains sinusoidal while applying the proposed adaptive DTF controller to manipulate the WEC system against wind speed variation. However, it is worth to mention that the instantaneous stator current waveforms are collected directly from the output nodes of sensors and hence, some spikes are seen due to mechanical vibrations in the wind turbine, fluctuating conditions of grid and high bandwidth of the display device. However, the spikes do not affect the displayed quantities for analysis. It can also be seen from Fig. 4.13(b) that the rotor speed of the WEC system follows reference speed properly when the wind speed changes from 3 m/sec to 10 m/sec. Thus, the proposed ANF-based adaptive DTF control can improve both the dynamics response of the WEC system and the overall performance.

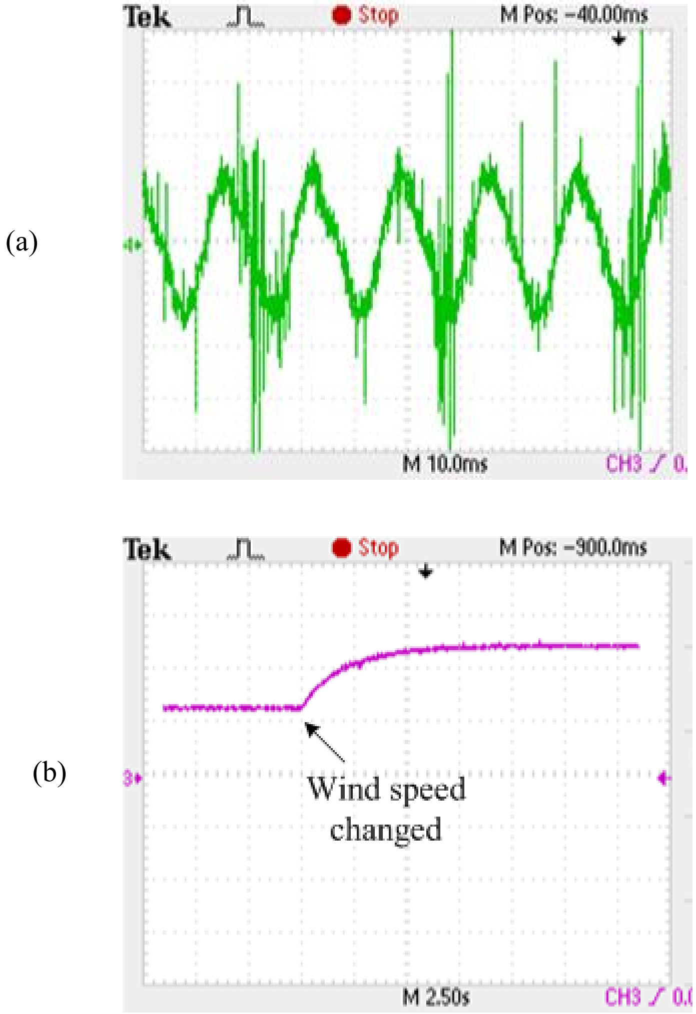

Fig. 4.13 Experimental performance of (a) instantaneous stator current (Scale: Y axis- 1div= 0.2 A); (b) rotor speed (Scale: Y axis- 1div= 1000 rpm) of the WEC system with proposed adaptive DTF controller for a step change in wind speed from 3.0 m/sec to 10.0 m/sec.

4.7 Chapter Conclusion

An ANF-based novel adaptive DTF control scheme has been proposed in this chapter for a grid-tied DFIG WEC system. The performance of the ANF-based adaptive DTF control has been verified by simulation tests using MATLAB/Simulink, in terms of dynamic response of electromechanical torque, stator current, and rotor speed. Simulation test results have shown that the proposed adaptive DTF controller is able to control the torque and stator current effectively at the starting time and at the time of wind speed variations, due to the adaptive feature and inherent learning capacity of ANF network. The stability of the DFIG WEC system with the proposed control has also been verified by bode plot analysis. A prototype DFIG WEC system was also built in the laboratory environment to test the effectiveness of the proposed adaptive DTF control technique in real-time. It has been verified through real-time test results that the proposed adaptive DTF control outperforms the classical control schemes such as fuzzy logic and PI control in terms of settling time and overshoot for the stator current and torque.

Chapter 5
Proposed INF-based Direct Torque and Flux Control Technique

This chapter includes the formulation of the INF-based direct torque and flux (DTF) control technique, detailed analysis of ensemble training methods, the performance analysis of the INF network and the proposed training method, and stability analysis of the WEC system.

5.1 Structure of the Proposed INF-based DTF Control Technique

The specific structure of the DFIG-based WEC system with the proposed INF-based DTF control technique is shown in Fig. 5.1. The INF-based DTF control technique uses the inputs of torque and flux errors (e_t, e_ψ), as well as their change rates (Δe_t, Δe_ψ). A selector (s_w) is used to improve the adaptive capability of the INF-based DTF control to accommodate transient and dynamic operating situations. When the system operates under transient conditions, based on the value of s_w, the set of linear parameters will be applied in INF network, which have been trained considering the transient operating condition of the WEC system to generate the control signal v_q for the rotor side converters. On the other hand, under dynamic wind speed conditions and according to the value of s_w, the other set of linear parameters will be applied, which have been trained considering the dynamic operating condition of the WEC system. The details of this adaptation technique are discussed later in Sections 5.2 and 5.3.

To calculate the stator flux, at first the α-β components of the stator flux ($\psi_{s\alpha}$, $\psi_{s\beta}$) are calculated from the α-β components of the stator voltages ($v_{s\alpha}$, $v_{s\beta}$) and currents ($i_{s\alpha}$, $i_{s\beta}$) by

$$\psi_{s\alpha} = \int (v_{s\alpha} - R_s i_{s\alpha}) dt \tag{5.1}$$

$$\psi_{s\beta} = \int (v_{s\beta} - R_s i_{s\beta}) dt \tag{5.2}$$

The magnitude (ψ_s) and angle (θ_s) of the stator flux are calculated by

$$\psi_s = \sqrt{\psi_{s\alpha}^2 + \psi_{s\beta}^2} \text{ and } \theta_s = \tan^{-1} \frac{\psi_{s\beta}}{\psi_{s\alpha}} \tag{5.3}$$

The generated torque (T_{em}) is calculated by

$$T_{em} = \frac{3P}{2}\left(i_{s\beta}\psi_{s\alpha} - i_{s\alpha}\psi_{s\beta}\right) \tag{5.4}$$

where P is the number of pole pairs in DFIG.

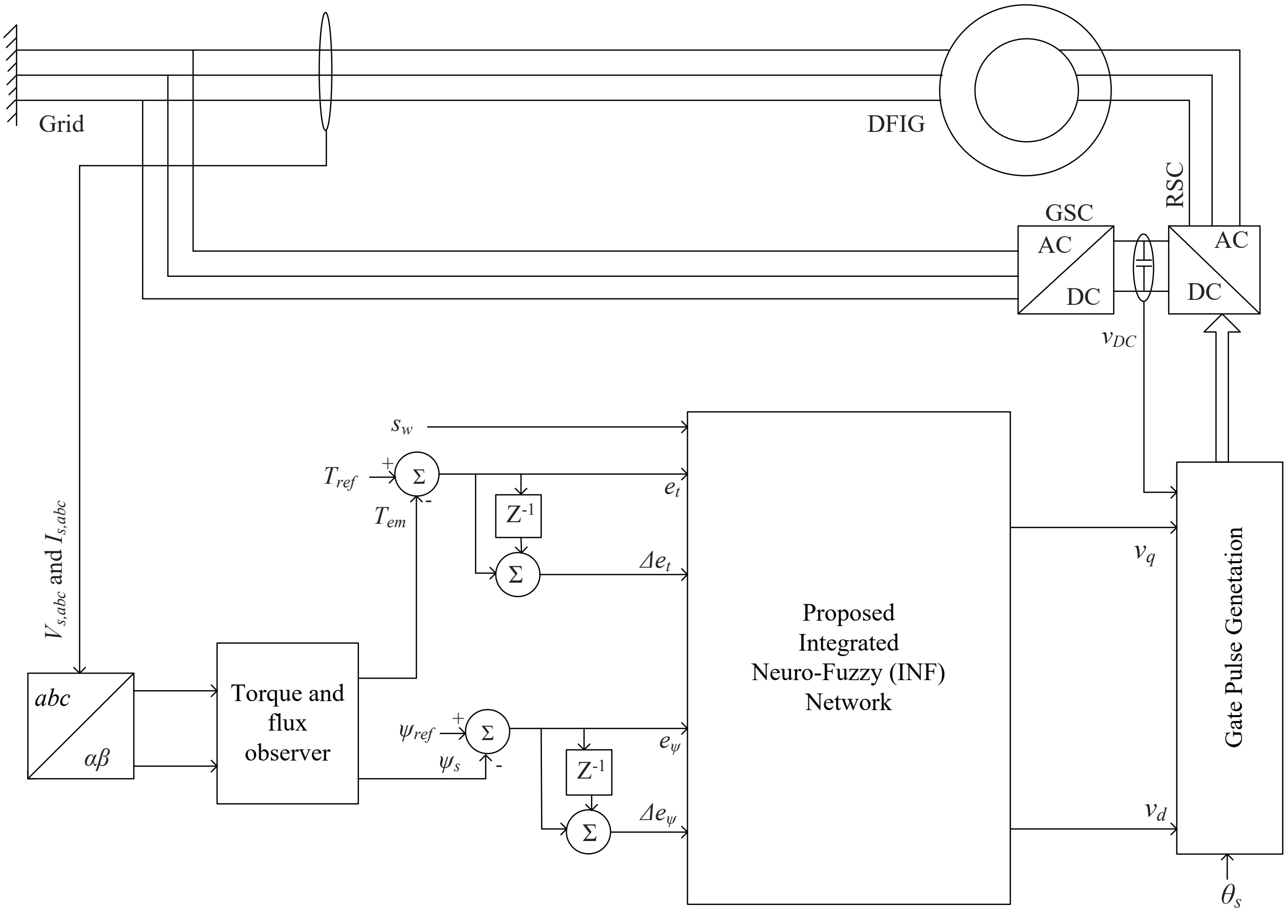

Fig. 5.1 Block diagram of the proposed INF-based DTF control technique for DFIG-based WEC system

5.2. Sugeno-based Fuzzy Interface System and Adaptive NF Network

Among different type of structure combining the neural network and fuzzy systems, the adaptive NF system represents the operation of a fuzzy interface system with different layers of computation similar to neural network. Therefore, the parameters of the specifiec fuzzy system can be trained and optimized using different training algorithms. As a result, the NF system represents an optimized parameter-based fuzzy interface system which also allows the adaptation of parameters through the training process.

A two-input sugeno-based fuzzy interface system with two rules, along with its NF network representation, are presented in Fig. 5.2. In this system, fuzzy weights W_1 and W_2 are estimated considering the input membershp functuions (MFs), and fuzzy rules (known as fuzzification process). For this sugeno-based fuzzy interface system the functional outputs f_1 and f_2 and the final output f are calculated as

$$f_1 = p_1x + q_1y + r_1 \tag{5.5}$$

$$f_2 = p_2x + q_2y + r_2 \tag{5.6}$$

$$f = \frac{W_1f_1 + W_2f_2}{W_1 + W_2} = \overline{W_1}f_1 + \overline{W_2}f_2 \tag{5.7}$$

where, p_1, p_2,q_1, q_2, r_1, r_2 are the linear parameter of the fuzzy system. The process of estimating the final output is known as the defuzzification process, as shown in Equation (5.7).

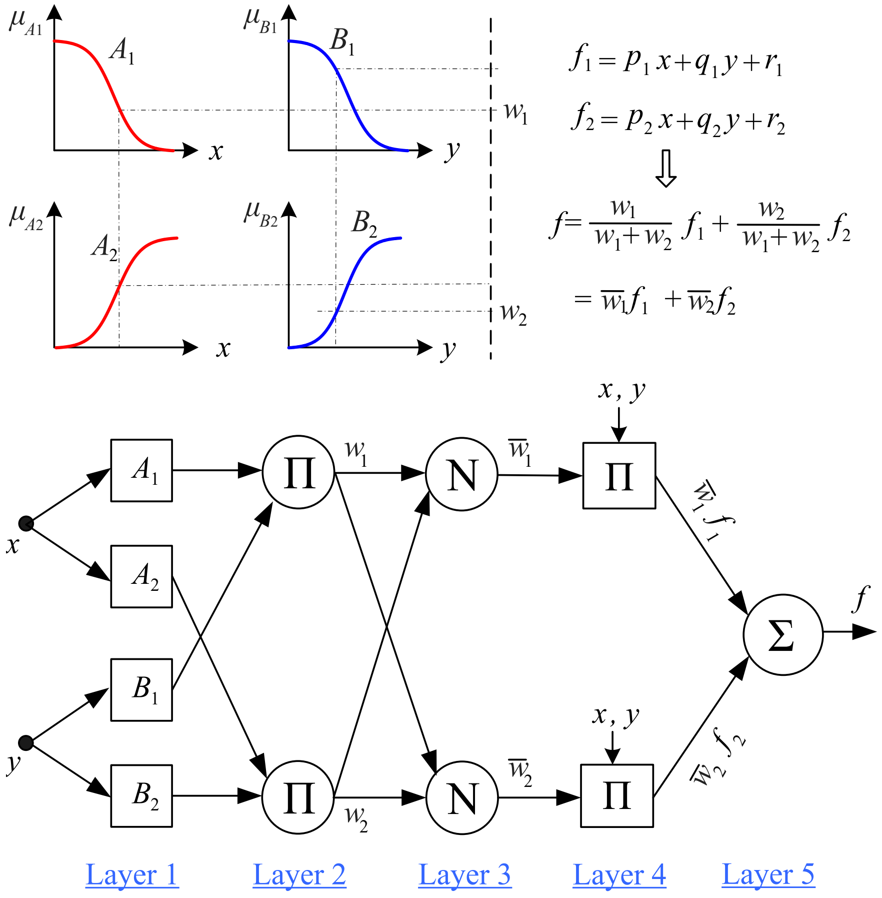

Fig. 5.2 A two-input sugeno-based fuzzy interface system and its NF network representation.

The computational burden of a NF network can be estimated by combining the computation steps of each layer as

$$N_{total} = N_{L1} + N_{L2} + \cdots + N_{L5} \tag{5.8}$$

where $N_{L1}, N_{L2}, N_{L3}, N_{L4}, N_{L5}$ denote the computational state in each layer, and N_{total} denotes the total computational states. Furthermore, the computational steps of each layer are calculated by

$$N_{L1} = \sum_{m}^{N_{ip}} n_{mf,m} \tag{5.9}$$

$$N_{L2} = N_{L3} = N_{L4} = \prod_{k=1}^{N_{ip}} n_{mf,k} \tag{5.10}$$

$$N_{L5} = 1 \tag{5.11}$$

where N_{ip} is total number of input variables and n_{mf} represents membership functions (MFs) in each input variable.

5.3 Structure of the Proposed INF Network

The specific structure of the proposed INF network is shown in Fig. 5.3. The functionality of each layer of INF network is described below:

Layer 1: This is the fuzzification layer. For the proposed INF network, each input has two MFs. Therefore, the MFs are presented as

$$\mu_{A_{ij}}(x_i) = \frac{1}{1 + e^{-a_{ij}(x_i - c_{ij})}} \tag{5.12}$$

where i =1, 2, ...,4; j=1, 2; x_1, x_2, x_3 and x_4 are the torque error, flux error, and the corresponding change of the errors (e_t, Δe_t e_ψ, Δe_ψ), respectively. The parameters a_{ij} and c_{ij} are the single sets of optimized nonlinear MF parameters.

Layer 2: This is the fuzzy operation layer. As the max-product fuzzy composition is used for the INF network, the firing strength for the m-th rule (μ_m) can be determined by

$$\mu_m = \prod_{i=1}^{4} \mu_{A_{ij}}(x_i) \tag{5.13}$$

where *m*=1, 2,...,16.

Layer 3: This is the normalization layer. The normalized firing strength ($\bar{\mu}_m$) for each rule becomes

$$\bar{\mu}_m = \frac{\mu_m}{\sum_{i=1}^{16} \mu_i} \tag{5.14}$$

Layer 4: This is the processing layer. The functional outputs of this layer $f_{m,1}$ and $f_{m,2}$ are related to the outputs O_1 and O_2, respectively. The parameters $\gamma_{p\_tr}^{m}$, $\gamma_{p\_ss}^{m}$ and γ_{q}^{m} are linear consequent parameters that will be optimized during training process, as discussed in the following subsection. f_{m_tr} and f_{m_ss} represent the functional outputs at the time of transient and steady states, respectively. At the time of transient states f_{m_tr} is used as $f_{m,1}$, otherwise f_{m_ss} is used as $f_{m,1}$, which is further used to calculate O_1. The adaptation of the $f_{m,1}$ is performed considering the value of s_w. The functional outputs, f_{m_tr} and f_{m_ss} are computed such that

$$f_{m\_tr} = \gamma_{0\_tr}^{m} + \sum_{p=1}^{4} \gamma_{p\_tr}^{m} x_p \tag{5.15}$$

$$f_{m\_ss} = \gamma_{0\_ss}^{m} + \sum_{p=1}^{4} \gamma_{p\_ss}^{m} x_p \tag{5.16}$$

$f_{m,1}$ and $f_{m,2}$are determined as

$$f_{m,1} = s_w \times f_{m\_tr} + (1 - s_w) \times f_{m_{ss}} \tag{5.17}$$

$$f_{m,2} = \gamma_0^m + \sum_{q=1}^{4} \gamma_q^m x_q \tag{5.18}$$

where *p*=1, 2, …, 4; *q*=1, 2, …, 4; *m*=1, 2, ..., 16.

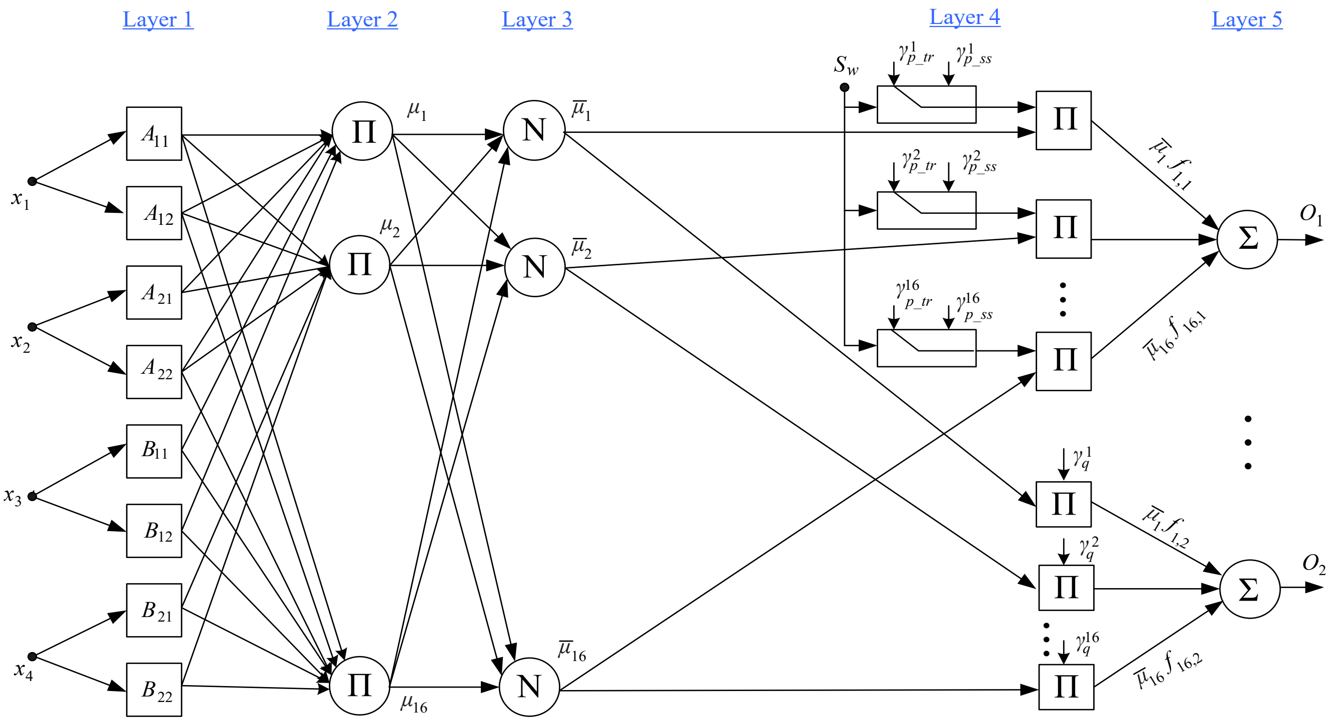

Fig. 5.3 Architecture of the proposed INF-network for DTF control technique

Layer 5: This is the defuzzification layer. The outputs O_1 and O_2 of the INF network are v_q and v_d, which are calculated by

$$O_1 = \sum_{m=1}^{16} \overline{\mu_m} f_{m,1} \tag{5.19}$$

$$O_2 = \sum_{m=1}^{16} \overline{\mu_m} f_{m,2} \tag{5.20}$$

5.4 Proposed Ensemble Training Method

The ensemble technique is applied to design different intelligent systems combining the outcomes from different algorithms and datasets[120]. Hence, the proposed ensemble training has the capacity to utilize the datasets obtained from different operating conditions to optimize nonlinear system parameters. The objective of the proposed ensemble training method is to train the INF system parameters based on a proposed weighted aggregator. The objective function W for ensemble training is formulated as

$$W = \frac{1}{2}\sum_{u=1}^{2}\left[\sum_{i=1}^{N}\left(y_{i,u} - O_{i,u}\right)^2\right] \tag{5.21}$$

where, $y_{i,u}$ are the targeted outputs from the training data pairs.

5.4.1 Training Algorithm

The INF system consists of both linear and nonlinear parameters to be updated. The consequent linear parameters $\gamma_{p\_tr}^{m}$, $\gamma_{p\_ss}^{m}$ and γ_{q}^{m} are trained using a recursive LSE training method, as described in Equations (5.18) and (5.19).

$$P_{k+1} = P_k - \frac{P_k b_{k+1} b_{k+1}^T P_k}{1 + b_{k+1}^T P_k b_{k+1}} \tag{5.22}$$

$$\gamma_{j,k+1}^{m} = \gamma_{j,k}^{m} + P_k + P_{k+1} b_{k+1}\left(y_{k+1} - b_{k+1}^T \gamma_{j,k}^{m}\right) \tag{5.23}$$

where $\gamma_{j,k+1}^{m}$are the linear parameters; b_{k+1} is the vector of the consequent parameters; y_{k+1} is the targeted output from the training data pairs; m=1,2,….,16; k=1, 2, …, N; N is the total number of training data. On the other hand, the premise nonlinear MF parameters, centers c_{ij_r}, and spreads a_{ij_r} are trained using gradient decent algorithm such that

$$a_{ij\_r}(n+1) = a_{ij\_r}(n) - \alpha_a \frac{\partial W}{\partial a_{ij_r}} \tag{5.24}$$

$$c_{ij\_r}(n+1) = c_{ij\_r}(n) - \alpha_c \frac{\partial W}{\partial c_{ij_r}} \tag{5.25}$$

where $\alpha_a$and α_c are the learning rates of the corresponding parameters; i=1, 2 …., 4; j=1, 2, ..., 4; r=1, 2; A weighted aggregator is suggested to optimize premise parameters based on the weights W_{t1} and W_{t2}, calculated by

$$W_{t1} = \frac{1/E_{r1}}{(1/E_{r1}) + (1/E_{r2})} \tag{5.26}$$

$$W_{t2} = \frac{1/E_{r2}}{(1/E_{r1}) + (1/E_{r2})} \tag{5.27}$$

where E_{r1} and E_{r2} are the error coefficients calculated from the theoretical and targeted values of each output such that

$$E_{r1} = \sum_{n=1}^{N} \frac{1}{2}\left(y_{1,n} - O_{1,n}\right)^2 \tag{5.28}$$

$$E_{r2} = \sum_{n=1}^{N} \frac{1}{2}\left(y_{2,n} - O_{2,n}\right)^2 \tag{5.29}$$

The premise parameters are optimized by

$$a_{ij} = W_{t1} \times a_{ij\_1} + W_{t2} \times a_{ij\_2} \tag{5.30}$$

$$c_{ij} = W_{t1} \times c_{ij\_1} + W_{t2} \times c_{ij\_2} \tag{5.31}$$

5.4.2 Steps of INF System Training

Fig. 5.4 shows the block diagram of the training procedures of the INF system using the proposed ensemble training method. Two different datasets are used in this training process. The first dataset is constructed considering the dynamic response of the WEC system due to wind speed variation. The first training data pair P_{S11}: $\{[x_{11}, x_{21}, x_{31}, x_{41}]; y_{11}\}$ is taken from the first dataset. The second data pair is constructed from first dataset as P_{S12}: $\{[x_{11}, x_{21}, x_{31}, x_{41}]; y_{21}\}$. On the other hand, the second dataset corresponds to the transient operating condition of the DFIG-based WEC system. The training data pair from the second dataset is constructed as P_{S21}: $\{[x_{11}, x_{21}, x_{31}, x_{41}]; y_{21}\}$. For a WEC system, in implementation, P_{S11}: $\{[e_{t1}, \Delta e_{t1}, e_{\psi 1}, \Delta e_{\psi 1}]; v_{q1}\}$, P_{S12}: $\{[e_{t1}, \Delta e_{t1}, e_{\psi 1}, \Delta e_{\psi 1}]; v_{d1}\}$, and P_{S21}: $\{[e_{t2}, \Delta e_{t2}, e_{\psi 2}, \Delta e_{\psi 2}]; v_{q2}\}$. The ensemble training will take following steps, as shown in Algorithm-5.1.

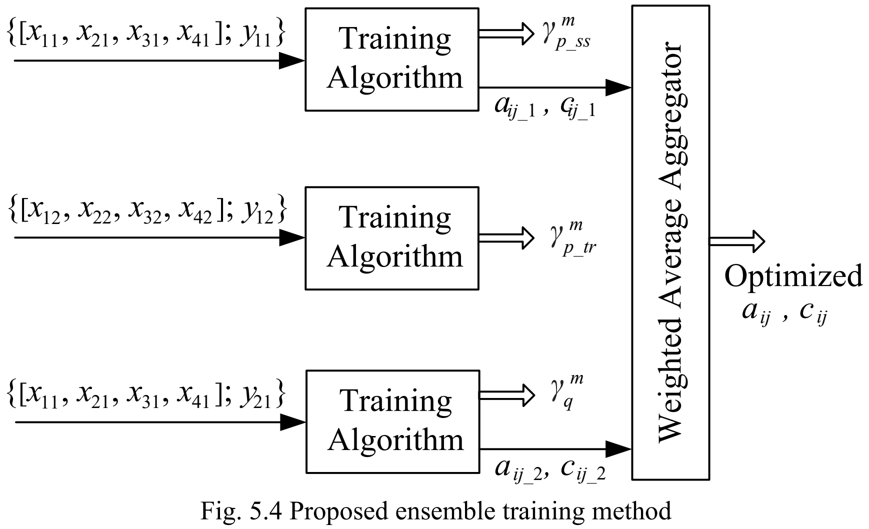

Fig. 5.4 Proposed ensemble training method

Algorithm 5.1 Ensemble Training Method

```
Step 1
    select $P_{S11}$. Optimize $\gamma_{p\_ss}^{m}$ using Equations (5.22) and (5.23)
Step 2
    Train $a_{ij\_1}$ and $c_{ij\_1}$ using Equations (5.24) and (5.25)
Step 3
    select $P_{S21}$ . Optimize $\gamma_{p\_tr}^{m}$ using Equations (5.22) and (5.23)
Step 4
    select $P_{S12}$ . Optimize $\gamma_{q}^{m}$ using Equations (5.22) and (5.23)
Step 5
    Train $a_{ij-2}$ and $c_{ij-2}$ using Equations (5.24) and (5.25)
Step 6
    Calculate $a_{ij}$, $c_{ij}$ using Equations (5.26) and (5.31)
```

5.5 Effectiveness Analysis of the Proposed Network and Training Algorithms

The proposed INF network is first trained with the ensemble training technique; the network is then validated using the holdout validation process, which splits the total dataset into two portions. One portion is used for training the INF network and the other is used for testing purposes. An initial dataset of approximately 2000 data pairs is obtained from the WEC system considering different speed conditions from 10 m/sec to 16m/sec; 70% of the datasets are used to train the INF network, and 30% of datasets are used for testing [121]. Furthermore, to investigate the effectiveness of the proposed INF network and ensemble training algorithm, the root mean square error (*RMSE*) for the training and testing is determined and analyzed:

$$RSME = \sqrt{\frac{\sum_{n=1}^{N}(y_n - O_n)^2}{N}} \tag{5.32}$$

where y_n are the targeted outputs from the training data pairs, O_n are the calculated data from INF network and N is the total number of data pairs. The performance of the proposed INF network is compared with the classical 4 input 2 output NF network in terms of *RMSE* and total computational states [122]. Additionally, the processing time required for training and operation for the related systems (using MATLAB software on a computer having Intel Core i7 processor and 12 GB RAM) are also analyzed and compared.

Table 5.1 summaries the calculation of the computational states using Eq. (5.8) to (5.11) for the proposed INF based DTF control technique using the NF network with 4 inputs and 2 outputs. It is clear that the computational burden is much lower for the proposed INF based DTF control technique due to the use of the new INF network. Table 5.2 summarizes processing effectiveness of the proposed INF and classical multioutput NF configurations. From the comparison, it is evident that the proposed INF configuration has significantly fewer computational states and shorter computational time compared to the similar classical one; this makes the proposed INF-based DTF control scheme effective to compute the output, maintaining near- equivalent network performance in terms of *RMSE*. Additionally, the effectiveness of the proposed training method is also compared with the traditional training algorithm by training the proposed INF network using both proposed and traditional training methods. Table 5.3 summarizes the performance comparison between the proposed and traditional training algorithms in terms of *RMSE*. From the table, it is evident that the proposed ensemble training technique is effective in terms of *RMSE* compared to the traditional training technique [49].

Table 5.1 Computational states calculation related to the NF networks

Parameters	**Classical NF network**	**Proposed INF network**
N_{L1}	16	8
N_{L2} to N_{L4}	96	64
N_{L5}	2	2
N_{total}	**16+96+2=114**	**8+64+2=74**

Table 5.2 Performance comparison between NF configurations

	Classical NF network	**Proposed INF network**
Computational states	114	74
Testing time (sec)	0.8923	0.3512
Testing *RMSE*	4.7×10^{-5}	4.73×10^{-5}
Training *RMSE*	2.87×10^{-6}	2.84×10^{-6}

Table 5.3 Performance comparison between training algorithms

	Traditional algorithm	**Proposed algorithm**
Training *RMSE*	2.87×10^{-6}	2.84×10^{-6}
Testing *RMSE*	4.74×10^{-5}	4.7×10^{-5}
Training time	68.04 sec	62.49 sec

5.6 System Stability Analysis

5.6.1 Second Order System and Stability Analysis

The transfer function (*T*(*s*)) of a second order linear time invariant (LTI) system can be presented by

$$T(s) = \frac{\omega_n^2}{s^2 + 2\zeta\omega_n + \omega_n^2} \tag{5.33}$$

where s is the Laplace variable, ω_n is the natural frequency of oscillation, ζ is the damping ratio. The percent overshoot (*%OS*) of *T*(*s*) can be calculated as

$$\%OS = \frac{C_{peak} - C_{final}}{C_{final}} \tag{5.34}$$

where C_{peak} and C_{final} represents the peak and the final value calculated from the step response of *T*(*s*). The *%OS* is related to ζ as

$$\zeta = -\frac{\ln\left(\frac{OS}{100}\right)}{\sqrt{\left(\pi^2 + \ln^2\left(\frac{\%OS}{100}\right)\right)}} \tag{4.35}$$

The stability of a LTI system can be analyzed from bode plot by observing the phase margin (*PM*). Mathematically,

$$PM = \emptyset - (-180^0) = 180^0 + \emptyset \tag{5.36}$$

where $\emptyset$ is the phase of the system at the crossover frequency (ω_c) [119].

5.6.2 Stability Analysis of the WEC system

The stability of the DFIG-based WEC system with the proposed INF-based DTF control technique is analyzed in this subsection by applying a step change of wind speed from zero to rated value. Firstly, the step response of the torque is obtained and the value of natural frequency of oscillation (ω_n), percent overshoot (*%OS)* and damping ratio (ζ) are determined from the torque step response. Furthermore, the approximate transfer function of a second order linear time invariant system is determined and presented in Table 5.4. System stability is analyzed using the estimated transfer function. Fig. 5.5 shows the bode plot of the estimated system. From the bode plot, it can be seen that the system is stable with a phase margin of 56^0 at ω_c=29.95 rad/sec. Hence, it can be concluded that WEC system with the INF-based DTF control technique can cope with any of wind speed variation within the rated operational range.

Table 5.4 Transfer function and system parameters of the approximated second order system

Quantity	Value
Damping ratio (ζ)	0.5412
Natural frequency of oscillation (ω_n)	39.57 (rad/sec)
Estimated transfer function	$\frac{1565}{s^2 + 42.83s + 1565}$
Poles of the estimated system	-21.415 ±j33.2743

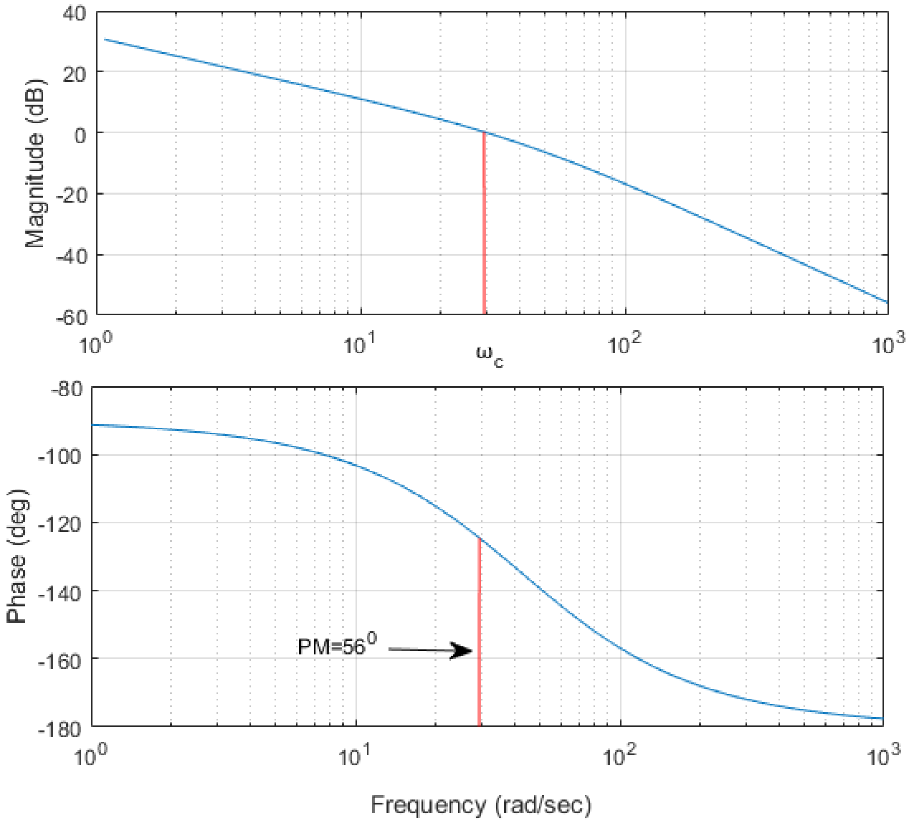

Fig. 5.5 Bode plot of the approximated system

5.6.3 Stability Analysis Under Disturbance

To investigate the stability under disturbance conditions, a wind profile with gust wind and external disturbance is considered, as shown in Fig. 5.6 [101], [123].

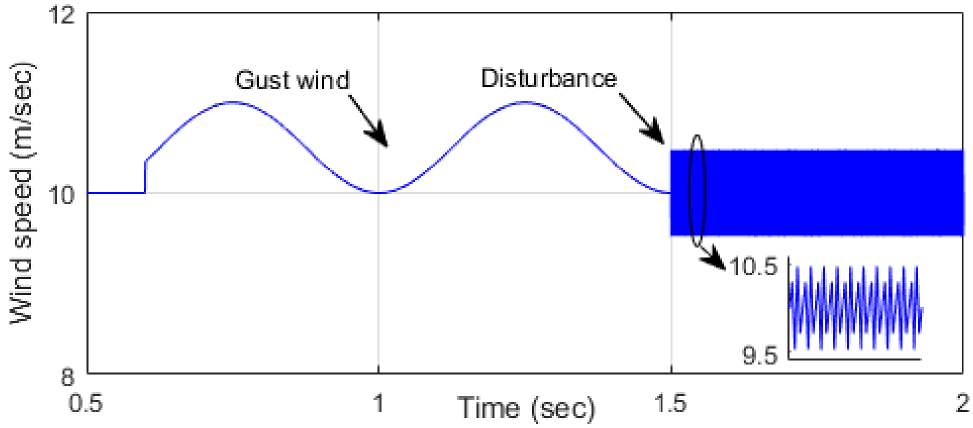

Fig. 5.6 Wind profile with gust wind and external disturbance.

The wind velocity incorporating the gust wind can be described as

$$V = V_{base} + \frac{V_{gust,m}}{2}(1 - \cos 4\pi t);\, 0.6 < t < 1.5 \tag{5.37}$$

where V_{base}= base wind speed, which is considered as 10 m/sec, $V_{gust,m}$= maximum gust speed, t= considered simulation time. Additionally, 10% random disturbance is added with the base wind velocity for the time of 1.5 sec to 2.0 sec. Furthermore, Lyapunov theorem of stability is applied to check the stability of the WEC system with the proposed INF-based DTF control technique through the trajectory analysis. Lyapunov theorem of stability states that a system is considered as stable near the equilibrium point λ, if for a Ω>0, there exists ρ>0 such that $\|\lambda(0)\| < \rho$, then $\|\lambda(t)\| \leq \Omega$ for all t>0; provided that $\Omega \epsilon \mathcal{R}$, and $\rho \epsilon \mathcal{R}$, where $\mathcal{R}$ is the set of real numbers [124], Here, $\|\lambda(t)\|$ represents the norm of $\lambda(t)$. As by definition in a two-dimensional space, $||\lambda|| = \sqrt{\lambda_x^2 + \lambda_y^2}$, so $\|\lambda(t)\| \leq \Omega$ signifies,

$$\lambda_x^2 + \lambda_y^2 \leq \Omega^2 \tag{5.38}$$

here $\lambda_x$and λ_y represents the x-axis and y-axis components of λ , respectively. Equation (34) shows that the system will be considered stable if the trajectory of λ lies within a circle of the finite radius Ω in a two-dimensional plane. The Lyapunov theorem is used to check the trajectory of torque

(T_e), flux (ψ_s) and rotor current (I_s) under the disturbance condition, as described above. Hence, considering (34), the constraints to be satisfied for these three quantities can be described as

$$\begin{gathered} T_{ex}^2 + T_{ey}^2 \leq \Omega_T^2 \\ \psi_{sx}^2 + \psi_{sy}^2 \leq \Omega_\psi^2 \\ I_{sx}^2 + I_{sy}^2 \leq \Omega_I^2 \end{gathered} \tag{5.39}$$

where $T_{ex} = T_e \cos \omega t$; $T_{ey} = T_e \sin \omega t$; $\psi_{sx} = \psi_s \cos \omega t$; $\psi_{sy} = \psi_s \sin \omega t$; $I_{sx} = I_s \cos \omega t$ and $I_{sy} = I_s \sin \omega t$ and Ω_T, $\Omega_\psi, \Omega_I \epsilon \mathcal{R}$, $\omega = 2\pi f$, f=grid frequency. Fig. 5.7 represents the trajectories of T_e, ψ_s, and I_s, considering the wind profile incorporating gusts and disturbances. From Fig. 5.7, it is obvious that the trajectories of T_e, ψ_s, and I_s have satisfied the constraints developed in Equation (5.35), as changes of these quantities have remained bounded within the circles of finite radii. Consequently, it can be concluded that the proposed INF-based DTF control can maintain stability of the WEC system for disturbance at wind speed conditions.

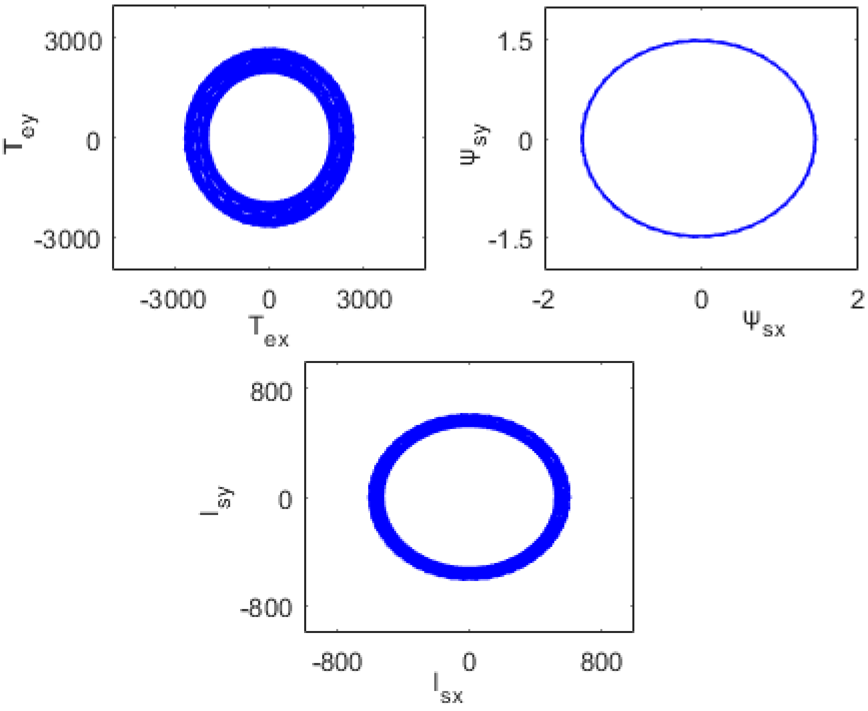

Fig. 5.7 Trajectories of T_e, ψ_s, and I_s, considering the wind profile in Fig. 5.6.

Table 5.5 Simulation parameters of DFIG WEC system

Parameters	Value
Rated power of the turbine	1.0 MW
Rated power of DFIG	1.0 MW
RMS Grid voltage	690 V
Grid frequency	60 Hz.
Number of pole pairs	2
Leakage resistance	2.9 mΩ
Leakage inductance	0.08 mH
Magnetizing inductance	2.5 mH
DC coupling capacitance	150 mF

5.7 Simulation Testing and Result Analysis

The effectiveness of the proposed INF-based DTF control technique is investigated through simulation testing, corresponding to wind-speed variations and starting transients for a DFIG-based WEC system. The performance of the WEC system using the proposed INF-based control technique is compared with the traditional decoupled NF-based DTF control scheme. The MATLAB/Simulink software is used for comparison and analysis. The parameters used in this study are summarized in Table 5.5.

Fig. 5.8 shows the performance comparison of the starting transient torque of the generator for the traditional decoupled, and the proposed INF-based DTF control technique. From Fig. 5.8(b), it is evident that the INF-based DTF control technique can significantly reduce the torque fluctuation and distortion, with the peak transient torque of 1.41×10^4 N.m vs 2.84×10^4 N.m generated by decoupled NF-based DTF control scheme (Fig. 5.8(a)). Moreover, it is clear that the INF-based DTF control technique can also reduce the transient time compared to the decoupled NF-based DTF control scheme (0.2 s vs. 0.3 s). Fig. 5.9 presents the transient performance of the rotor speed using the related controllers. The INF-based DTF control technique has a starting peak speed of 189.84 rad/sec, which is lower than that of the decoupled NF-based scheme (198.84 rad/sec). The INF-based control can also significantly reduce the transient time of the rotor speed in comparison with decoupled DTF control technique (0.2 vs 0.4 s) due to its more efficient adaptive capability.

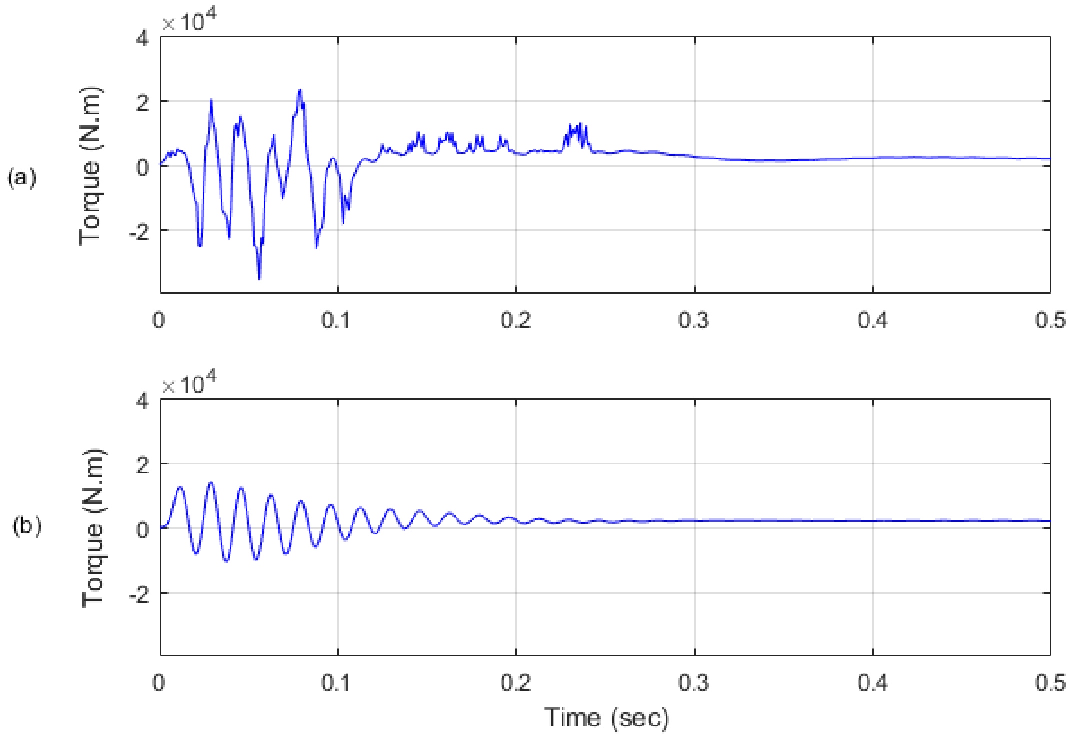

Fig. 5.8 Transient performance comparison of the generator starting torques, using:(a) decoupled NF; (b) proposed INF-based DTF control scheme

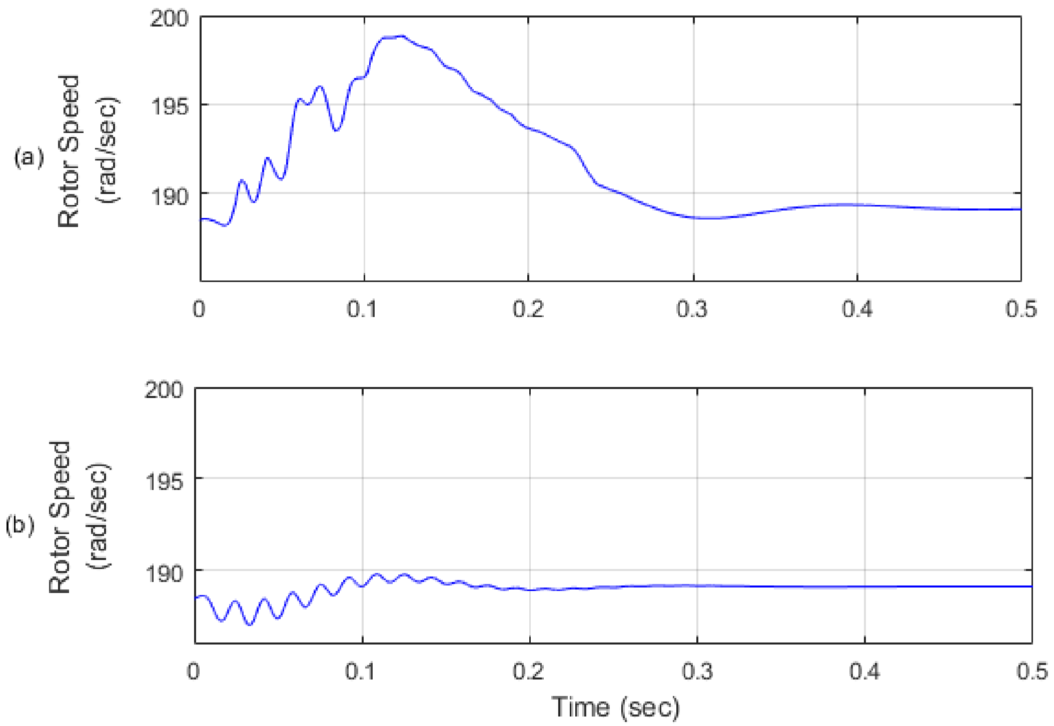

Fig. 5.9 Transient performance comparison of rotor speed using: (a) decoupled NF; (b) proposed INF - DTF control scheme.

Furthermore, Fig. 5.10 shows the transient performance comparison of the stator current between these controllers. Although the performance of these controllers is similar in this case with transient current peaks approximately 1.1×10^4, the transient current of the proposed INF-based DTF control technique is less distorted, and decays faster (0.2 s) compared to decoupled NF-based DTF control scheme (0.3 s). Consequently, it can be concluded that the proposed INF-based DTF control technique can improve the transient performance of the DFIG-based WEC system due to altering the consequent parameters of the proposed INF network considering transient operation of WEC system.

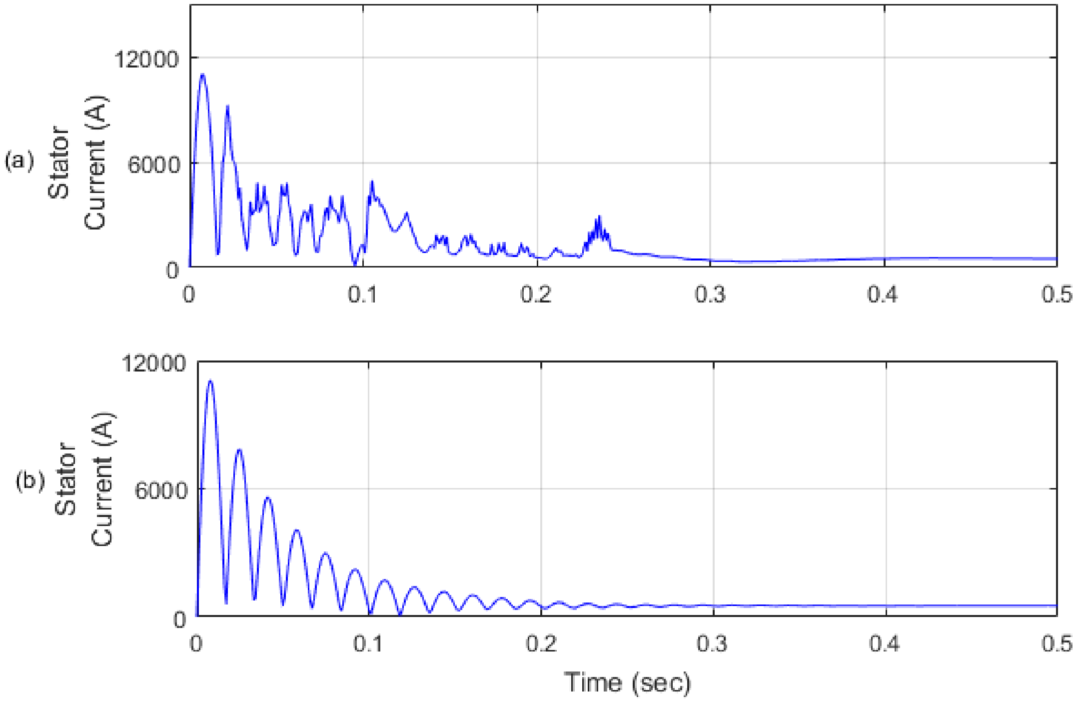

Fig. 5.10 Transient performance comparison of stator current using: (a) decoupled NF; (b) proposed INF-based DTF control scheme

On the other hand, the dynamic performance of the DFIG-based WEC system with the proposed INF-based DTF control technique is studied considering a step change in wind speed of 10 m/sec to 16 m/sec at 1.0 sec, using the related control techniques. Figs. 5.11 to Fig 5.13 show the dynamic performance of different quantities related to DFIG-based WEC system. From Fig. 5.11(b), it is observed that the peak torque from the INF-based control reaches 5975 N.m, which is much lower than the decoupled NF-based DTF control scheme (6012 N.m). In addition, it is seen from Fig. 5.12 that the rotor speed peak using the proposed INF-based DTF control is also slightly lower (190.75 rad/sec) than the decoupled NF-based DTF control scheme (190.8 rad/sec). Similarly, from Fig. 5.13, the stator current peak using the INF-based DTF control is (1076 A), which is lower compared to the classical decoupled NF-based DTF control scheme (1115 A). Hence, it is evident that the proposed INF-based DTF control technique can improve the dynamic performance of the WEC system.

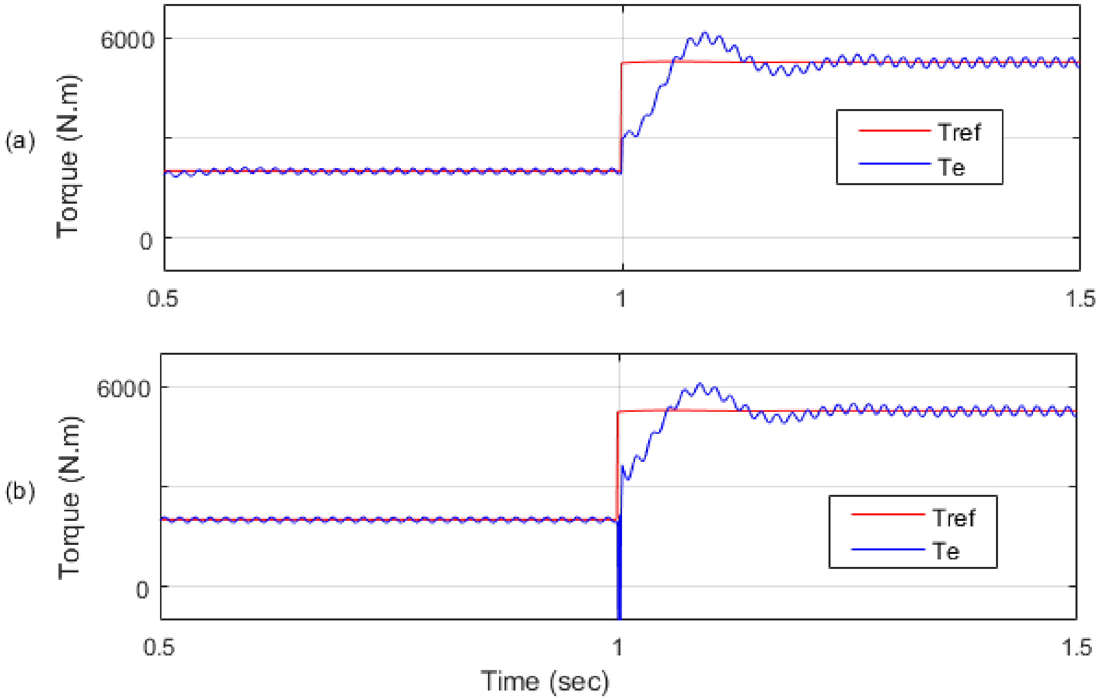

Fig. 5.11 Generator torque performance comparison for a step change in wind speed using: (a) decoupled NF; (b) proposed INF-based DTF control scheme

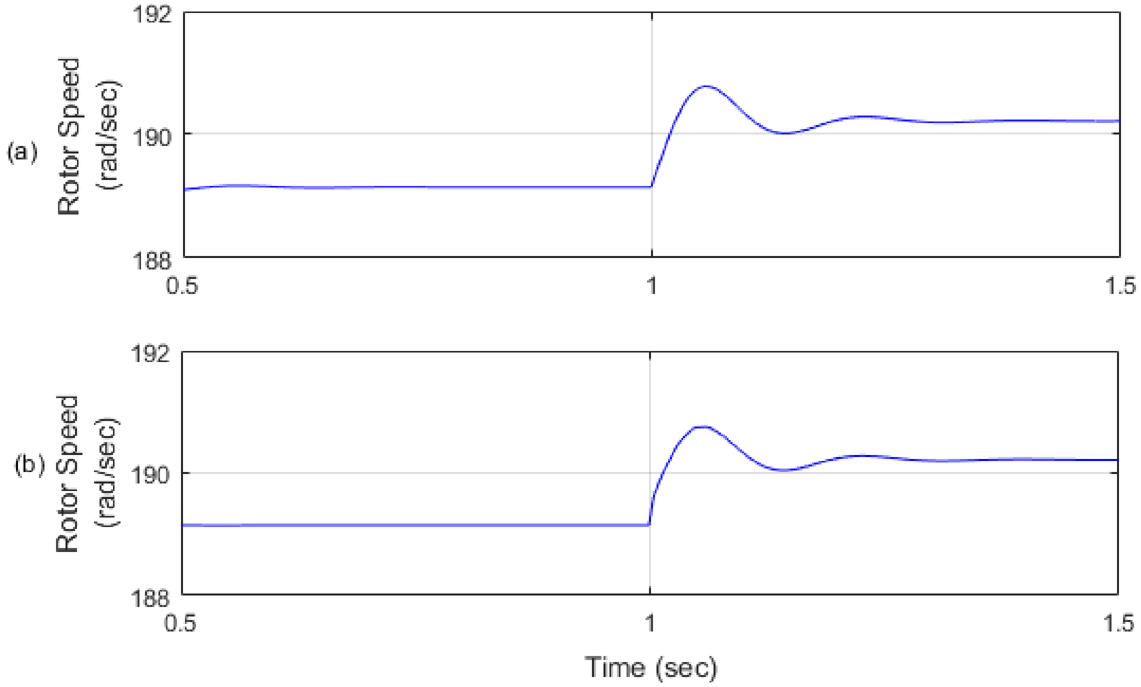

Fig. 5.12 Rotor speed performance comparison for a step change in wind using: (a) decoupled NF; (b) proposed INF-based DTF control scheme

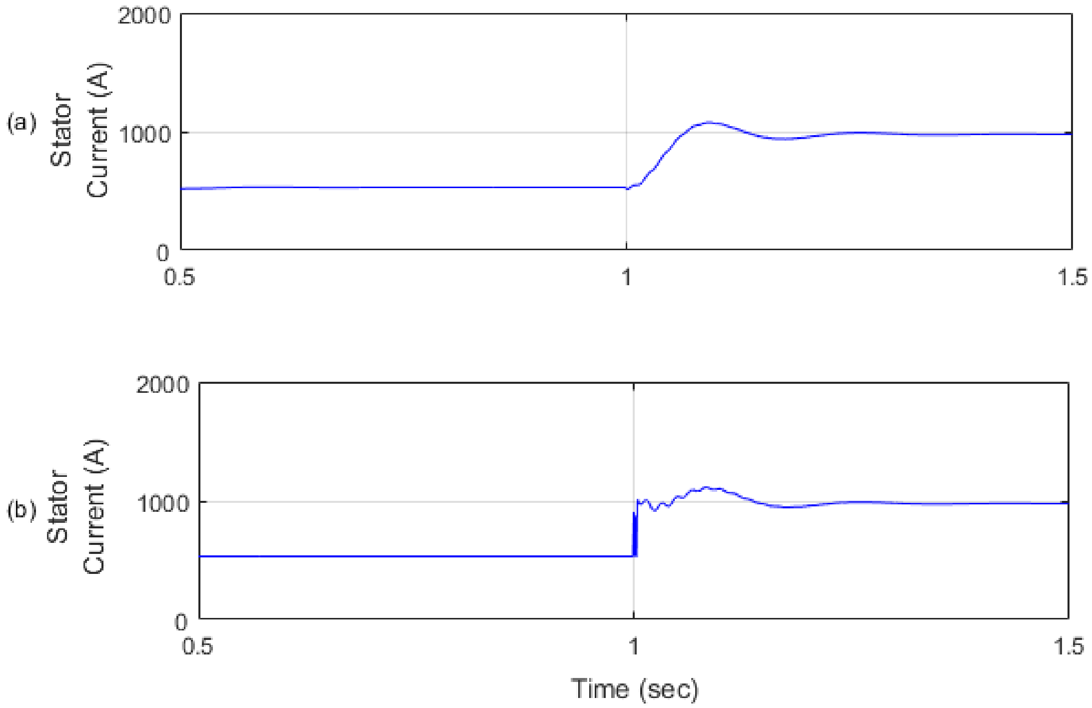

Fig. 5.13 Stator current performance comparison for a step change in wind using: (a) decoupled NF; (b) proposed INF-based DTF control scheme.

Fig. 5.14 shows the comparative responses of torque, stator current and rotor speed of the DFIG WEC system using different control techniques for a step change in wind speed from 0 m/sec to 16 m/sec. From these responses, it is observed that the peak of the torque in the step response (Fig. 5.14 (a) is much lower (5977 N.m) for the proposed INF-based DTF control technique compared to both the conventional NF and PI-based controller (6200 N.m and 6400 N.m) respectively. Similarly, the current peak for the proposed technique is 1097 A, which is 1122 A for the conventional NF and 1161 A for the PI-based schemes (Fig 5.14(b)). Likewise, rotor speed peak at the time of step change is slightly lower for the proposed control technique (190.744 rad/sec vs 190.875 and 190.847 rad/sec), which is evident from Fig. 5.14(c). Table 5.6 summarizes the performance of the INF-based DTF control technique compared to the decoupled NF and decoupled PI-based DTF control scheme. From this table, it is observed that the *%OS* for torque, rotor speed and stator current have improved for the proposed INF-based technique compared to both the classical decoupled NF and benchmark-tuned PI-based scheme.

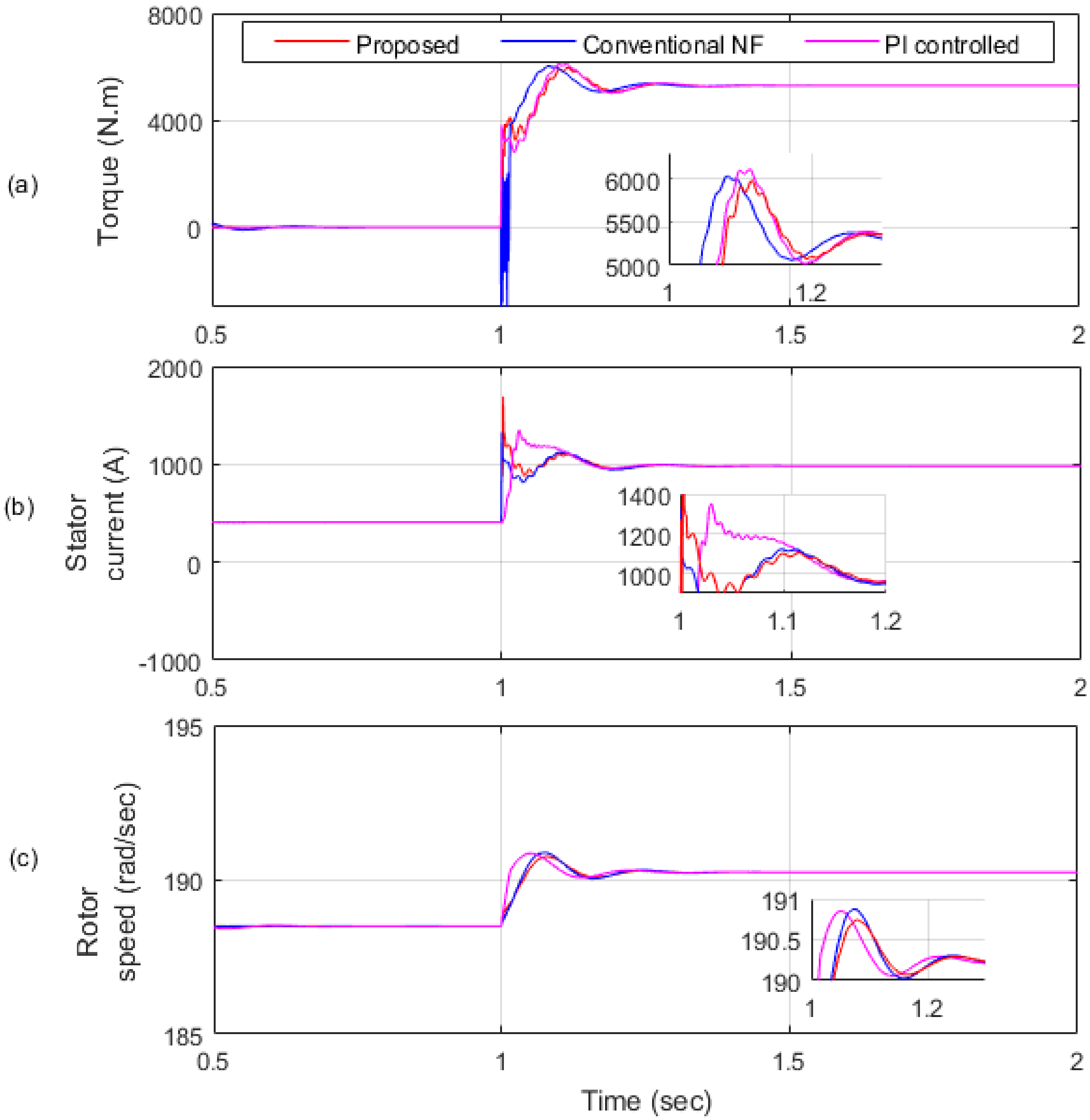

Fig. 5.14 Comparative performances among the proposed INF, conventional NF and PI controllers for a step change in wind speed (0-16 m/sec): (a) torque; (b) stator current; (c) rotor speed.

Table 5.6 Performance comparison among the related control techniques

Property	**Proposed INF-based DTF control**	**Decoupled NF-based DTF control**	**Decoupled PI-based DTF control**
Torque Overshoot	12.7%	16.91%	20.73%
Rotor speed Overshoot	0.27%	0.339%	0.324%
Stator current Overshoot	11.4%	14.1%	17.98%

5.8 Experimental Testing and Result Analysis

The effectiveness of the proposed INF-based DTF control technique is verified by experimental tests in this section. A prototype of a DFIG-based WEC system is implemented in the laboratory environment using the DSP board (DS 1104). A four-quadrant dynamometer from ‘LabVolt Series’ is used to emulate the real-time behavior of a wind turbine, which is shown in Fig. 5.15. The parameters and ratings of the assembled DFIG-based WEC system are presented in Table 5.7. To investigate the real-time dynamic response of the DFIG-based WEC system, the simulated wind speed varies from 3 m/sec to 12 m/sec through ‘LVDAC-EMS’ software from the command computer.

Table 5.7 Parameters of the experimental setup

Parameters	Value
Rated wind turbine power	450 W
Pitch angle	0°
Rated DFIG power	480 VA
Grid voltage (rms)	208 V
Number of pole pairs	2
Leakage resistance	8.10 Ω
Leakage inductance	30.0 mH

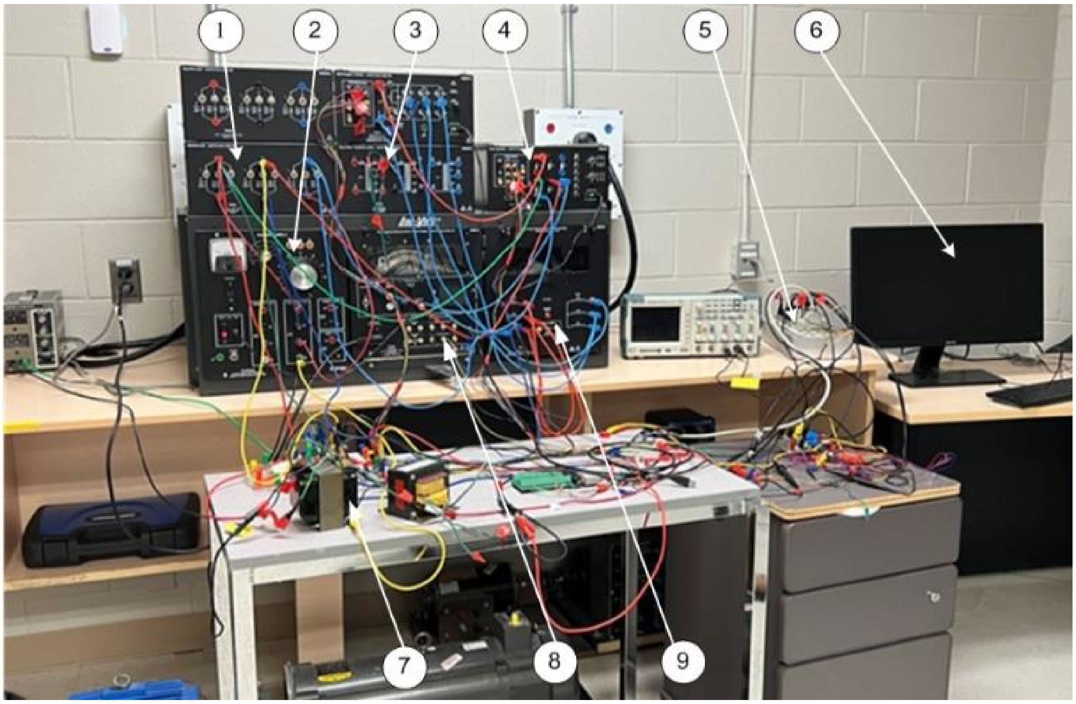

Fig. 5.15 Experimental setup of the DFIG-based WEC system for testing: (1) line inductance; (2) grid; (3) rotor side converter; (4) rectifier; (5) DS1104; (6) command computer for DS 1104; (7) sensors; (8) wind turbine; (9) DFIG.

Fig. 5.16 shows the dynamic response of the torque, rotor speed and stator current of the DFIG-based WEC system using the decoupled NF-based DTF control scheme. Fig. 5.17 presents the dynamic responses of the same quantities using the proposed INF-basedDTF control technique. It is evident from Figs. 5.16(a) and 5.17(a) that the change in torque for wind speed variation is smoother for the proposed INF-based DTF control technique compared to the conventional NF scheme. Additionally, the WEC system torque using the proposed INF-based DTF control technique can track the reference more accurately compared to the decoupledDTF control scheme. Similar to the classical control technique, the proposed INF-based DTF control technique can also maintain smooth rotor speed change at the time of wind speed variation (Figs. 5.16(b) and 5.17(b)). Moreover, the stator current for using the INF-based DTF control technique exhibits less fluctuation compared to using conventional NF-based decoupled DTF control scheme (Figs. 5.16(c) and 5.17(c)). Consequently, it can be concluded that the proposed INF-based DTF control outperforms the related classical control technique in terms of dynamic performance, whereas it does not significantly affect the performance of the rotor speed. Furthermore, the proposed INF-based DTF control technique does not distort the sinusoidal shape of stator current of the DFIG in WEC system, as indicated in Fig. 5.17(d), which implies the controller’s possible effectiveness for grid-connected operation. However, some spikes are visible in the waveform of instantaneous current and torque as discussed in Chapter 4 (Section 4.6).

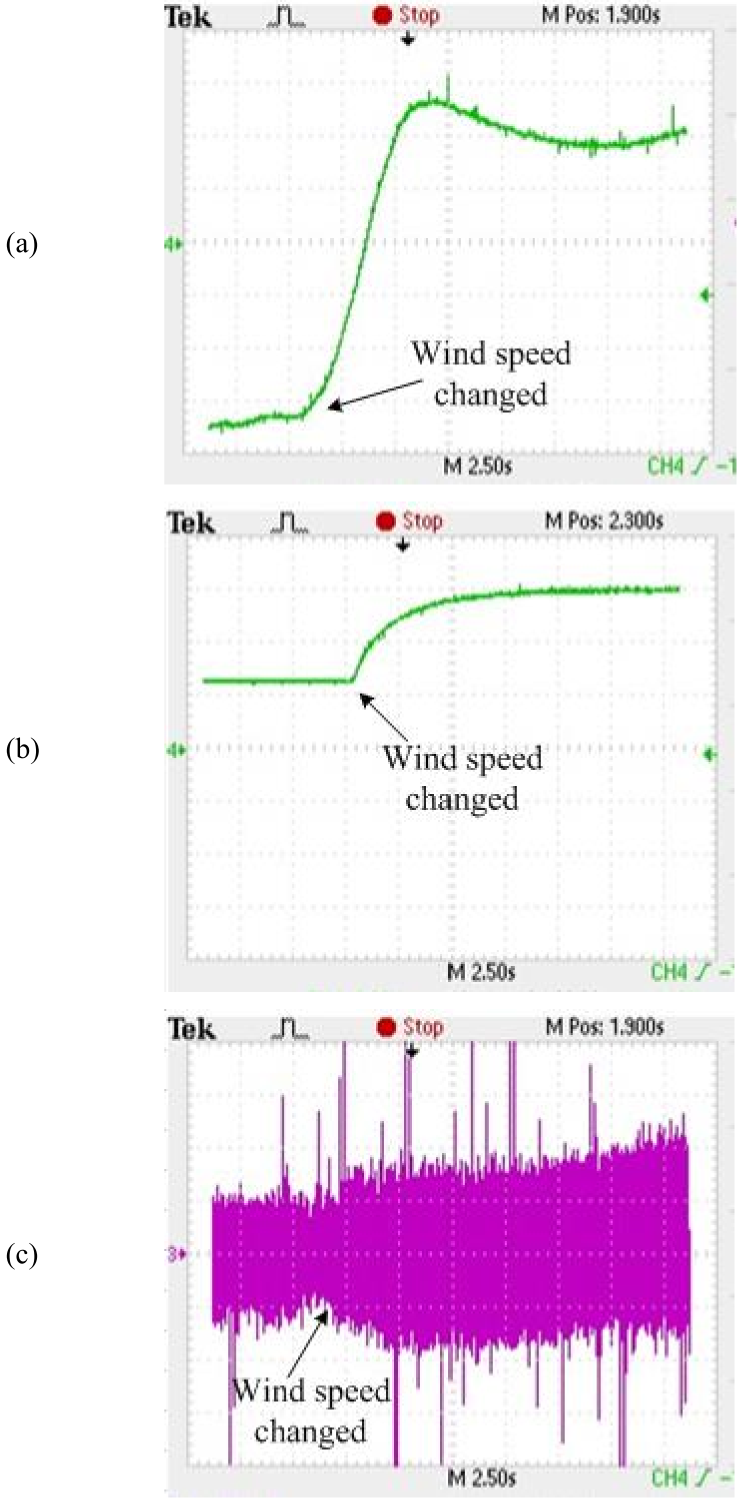

(d)

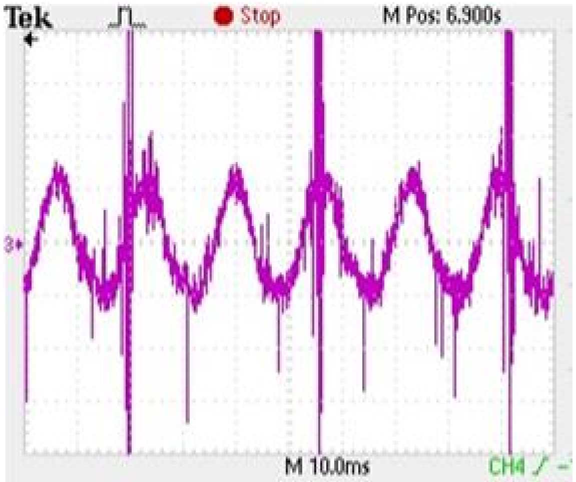

Fig. 5.16 The Experimental dynamic response of the DFIG-based WEC system using decoupled NF-based DTF control scheme: (a) torque (Scale: 1 div: =1.0 N.m); (b) rotor speed (Scale: 1 div: =1000 rpm); (c) stator current (Scale: 1 div: =0.2 A); (d) instantaneous stator current.

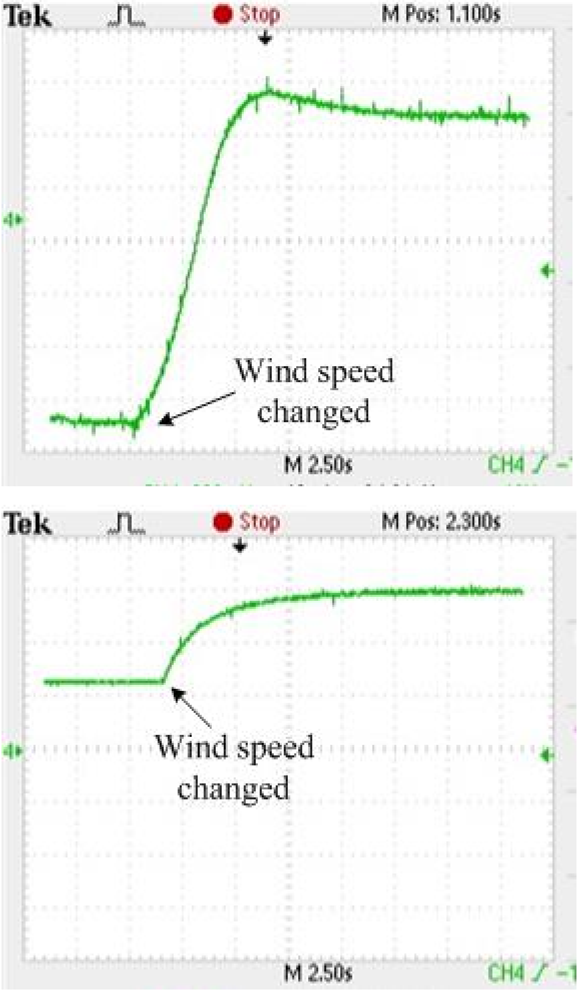

(c)

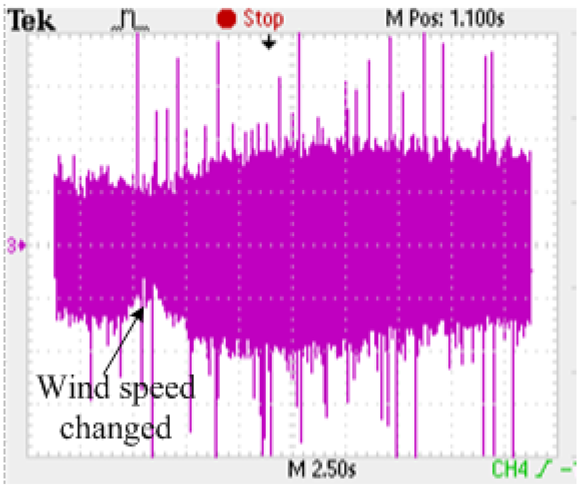

(d)

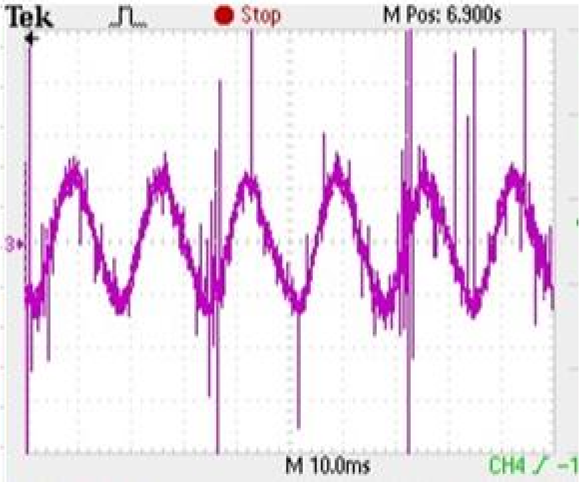

Fig. 5.17 Experimental dynamic response of the DFIG-based WEC system using the proposed INF-based DTF control technique: (a) torque (Scale: 1 div: =1.0 N.m); (b) rotor speed (Scale: 1 div: =1000 rpm); (c) stator current (Scale: 1 div: =0.2 A); (d) instantaneous stator current

5.9 Chapter Conclusion

A novel INF-based DTF control technique was presented in this chapter to control the RSC of DFIG-based WEC system. The proposed INF-based DTF control scheme has been found to have less computational burden compared to the classical NF-based DTF control. The transient and steady-state operating conditions of the WEC system have been incorporated with the INF by adjusting some of its parameters. In addition, an ensemble training algorithm has also been developed for online training of the proposed INF structure. Stability analysis of the DFIG-based WEC system using the INF-based DTF control technique has been also provided. The performance of the WEC system using INF-based DTF control has been examined firstly by using simulation tests, with the comparison of the classical decoupled NF-based DTF control scheme. Finally, a prototype DFIG-based WEC system has been built to test the performance of the proposed INF-based DTF control scheme in real-time. It has been found that the proposed INF-based DTF control technique improved the performance of the generator torque, stator current and rotor speed compared to the classical decoupled NF-based DTF control scheme. Therefore, the proposed INF-based DTF control scheme could be a potential candidate for real-life grid-connected DFIG-based WEC system.

Chapter 6

Neuro-Fuzzy based Fault Tolerant Control Technique for Induction Machine

In this chapter, a neuro fuzzy (NF) based fault-tolerant control (FTC) technique will be presented to accommodate the induction machine (IM) rotor bar fault. Firstly, the effect of BRB fault on current and torque is analyzed. Secondly, the proposed NF-based FTC approach is discussed. The effectiveness of the FTC technique is verified through simulation tests.

6.1 Fault Tolerant Control of IM

As discussed in Chapter 2 (Section 2.11), IM faults can cause motor performance degradation such as torque fluctuations, overheating, and power loss. The FTC aims to compensate for the adverse effect of faults so that the performance of the faulty machine can be improved to some extent before proper repairs or maintenance operations are undertaken. This study focuses on FTC for IM with BRB fault.

6.2 Analysis of Current and Torque of IM

From the discussions in Chapter 3 (Section 3.1), it is seen that when one or more rotor bars break then their adjacent bars have to carry more currents, which causes an asymmetry in magnetic flux distribution of IMs. Thus, the motor current incorporates different sideband frequencies, which is reflected on the line current spectra of faulty IMs. The characteristics sideband frequencies (f_k) for the BRB fault in IMs can be calculated as

$$f_k = (1 \pm 2ks) \times f_0 \tag{6.1}$$

where f_0 is the grid frequency in Hz; s is the slip; $k = \pm 1, \pm 2, \ldots, \pm N$, N is the order of sidebands.

If BRB fault occurs in an IM, the faulty stator current (I_s) can be presented as

$$I_s = I_{s\_0m} \sin 2\pi f_0 t + \sum_{k=-N}^{N} I_{s\_km} \sin 2\pi f_k t = \quad I_{s\_0} + I_{s\_ripple} \tag{6.2}$$

where

$I_{s\_0} = I_{s\_0m} \sin(2\pi f_0 t)$

$$I_{s\_ripple} = \sum_{k=-N}^{N} I_{s\_km} \sin(2\pi f_k t)$$

I_{s_0} is the current component of fundamental frequency; I_{s_ripple} is the current component that introduces ripples in the stator current when BRB fault occurs in the IM. From the discussions in Chapter 2 (Section 2.6), the torque T_{em} and flux ψ_s of the IM can be estimated as

$$\psi_{qs} = -\frac{v_{ds} - i_{ds}R_s}{\omega_s} \tag{6.3}$$

$$\psi_{ds} = \frac{v_{qs} - i_{qs}R_s}{\omega_s} \tag{6.4}$$

$$\psi_s = \sqrt{\psi_{ds}^2 + \psi_{qs}^2} \text{ and } \theta_s = \tan^{-1}\frac{\psi_{qs}}{\psi_{ds}} \tag{6.5}$$

$$T_{em} = \frac{3P}{2}\left(i_{qs}\psi_{ds} - i_{ds}\psi_{qs}\right) \ (N.m) \tag{6.6}$$

where

v_{ds}, v_{qs} — *d*- axis and *q*- axis comments of supply voltage v_s;

i_{ds}, i_{qs} — *d*- axis and *q*- axis comments of IM current I_s;

ω_s— synchronous speed of the IM;

ψ_{ds} and ψ_{qs}— *d*- axis and *q*- axis components of flux ψ_s in the IM;

P— number of pole pairs in IM.

Considering Equation (6.2), the *d*- axis and *q*- axis components (i_{ds} and i_{qs}) of IM current I_s can be estimated as

$$\begin{bmatrix} i_{ds} \\ i_{qs} \end{bmatrix} = \mathcal{T}_{dq}\{I_s\} = \mathcal{T}_{dq}\{I_{s\_0}\} + \mathcal{T}_{dq}\{I_{s\_ripple}\} = \begin{bmatrix} i_{ds\_0} + i_{ds\_ripple} \\ i_{qs\_0} + i_{qs\_ripple} \end{bmatrix} \tag{6.7}$$

where $\mathcal{T}_{dq}\{I_s\}$ represents the *d-q* transformation of I_s, that produces i_{ds} and i_{qs} [**]; i_{ds_0} and i_{qs_0} represents *d*- axis and *q*- axis comments of I_{s_0}; i_{ds_ripple} and i_{qs_ripple} represents *d*- axis and *q*- axis comments of I_{s_ripple}. Hence, the torque T_{em} of the IM at faulty condition can be estimated as

$$T_{em} = \frac{3P}{2}\left(i_{qs}\psi_{ds} - i_{ds}\psi_{qs}\right)$$

$$T_{em} = \frac{3P}{2}[(i_{qs\_0} + i_{qs\_ripple})\psi_{ds} - (i_{ds\_0} + i_{ds\_ripple})\psi_{qs}]$$

$$T_{em} = \frac{3P}{2}[(i_{qs\_0}\psi_{ds} - i_{ds\_0}\psi_{qs})] + \frac{3P}{2}[(i_{qs\_ripple}\psi_{ds} - i_{ds\_ripple}\psi_{qs})]$$

$$T_{em} = T_{em\_0} + T_{em\_ripple} \tag{6.8}$$

where

$$T_{em\_0} = \frac{3P}{2}[(i_{qs\_0}\psi_{ds} - i_{ds\_0}\psi_{qs})]$$

$$T_{em\_ripple} = \frac{3P}{2}[(i_{qs\_ripple}\psi_{ds} - i_{ds\_ripple}\psi_{qs})]$$

T_{em_0} and T_{em_ripple} are the induced electromagnetic torque and torque ripples due to BRB fault of the IM, respectively. Hence it can be concluded that a faulty IM introduces more ripples in the output torque.

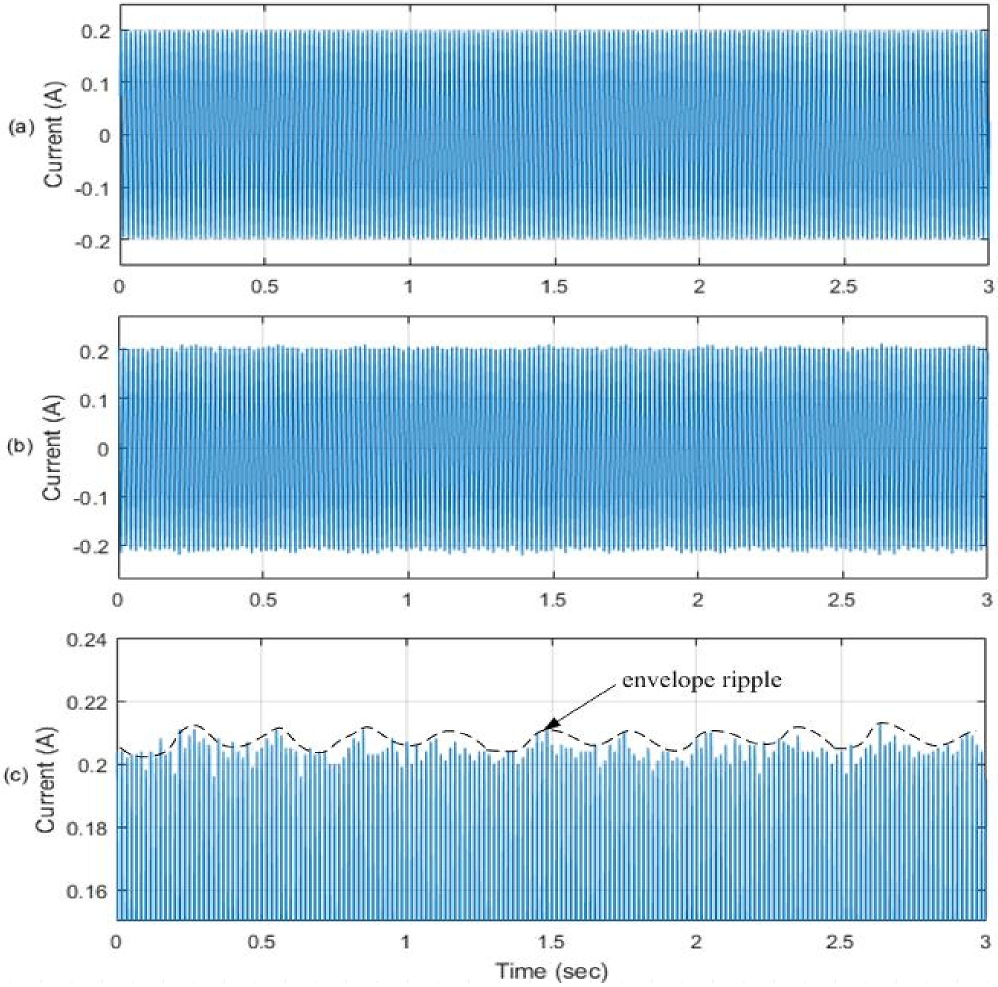

Fig. 6.1. The IM stator current signature comparison: (a) healthy IM, (b) faulty IM with three BRBs, (c) envelope ripple at faulty current signature presented in 6.1(b).

Fig. 6.1 represents the real time stator current signature comparison of IMs, which are collected using the experimental setup presented in Chapter 5 (Fig. 5.4). As the BRBs cannot carry current in IM operation, these broken bars cause asymmetry in the magnetic flux distribution in IM. This asymmetry is reflected in the stator current signature of the IM. From Fig. 6.1(a) it is observed that if the IM is healthy, the current is in an ideal sinusoidal form and there are no clear ripples in the current envelop signature. On the other hand, it is seen from Fig. 6.1(b) that ripples are clearly recognized in current envelopes for the IM with BRB fault.

Fig. 6.2 represents the IM torque responses for a healthy IM, and a faulty IM with three BRBs. The torque outputs from the healthy and faulty IM are calculated using Equation (6.6), using the corresponding stator signals as shown in Fig. 6.1. From Fig. 6.2(a) it is evident that the torque envelope of the faculty IM has clearer envelope ripples due to BRB fault, in comparison with the torque outputs from a healthy IM as reflected in Fig. 6.2(b).

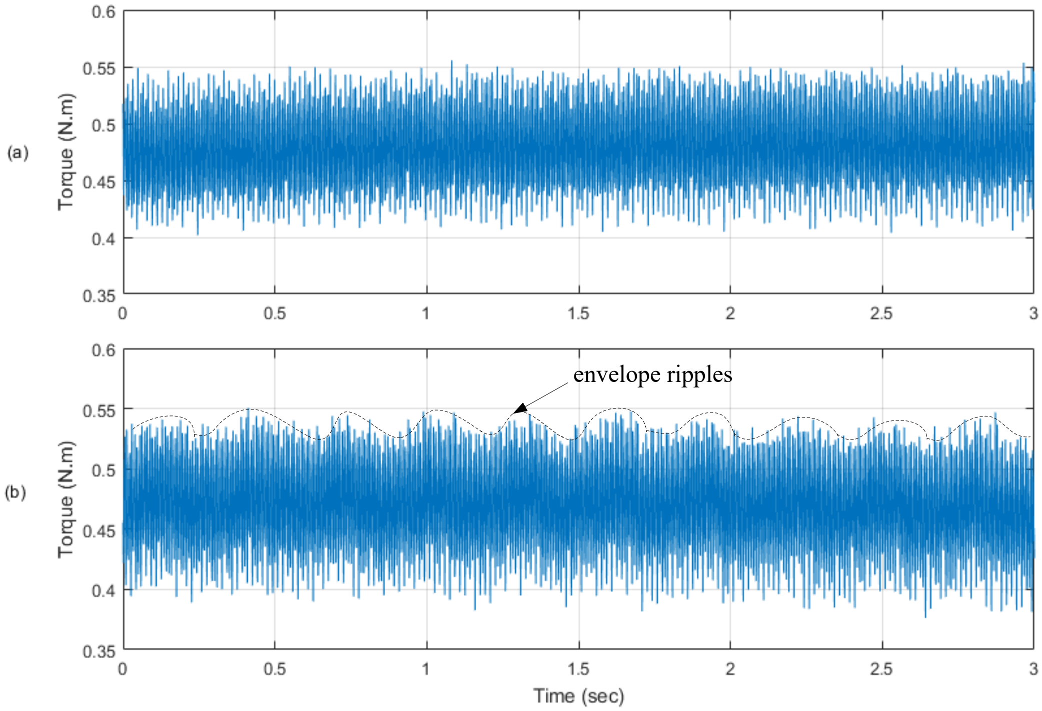

Fig. 6.2 The IM torque response comparison: (a) healthy IM, (b) faulty IM with three BRBs.

6.3 Analysis of Current and Torque Responses of a Faulty IM

Firstly, to investigate the effects of the BRB fault on IM outputs, different samples of current spectra of an IM having BRB faults are considered using the experimental setup presented in Chapter 3 (Fig. 3.4). The ratio I_{s_km}/I_{s_0m} for different samples of the IM with three BRBs are presented at Table 6.1. To model the faulty current in simulation, the average ratio of I_{s_km}/I_{s_0m} is considered. The specific sideband harmonics are generated under different IM operating slip s or speed. Additionally, the magnitude of the harmonics at current signature are estimated considering the average ratio of I_{s_km}/I_{s_0m}. Finally, the fault current signature is formulated by adding the sideband harmonics to the fundamental current response of the IM. Fig. 6.3 illustrates the modeling diagram of the current signature for a faulty IM in simulation.

Table 6.1. The ratio I_{s_km}/I_{s_0m} of IM with BRBs

k value	Sample 1	Sample 2	Sample 3	Sample 4	Sample 5	Average
1	1.00×10^{-2}	8.67×10^{-3}	8.88×10^{-3}	8.30×10^{-3}	9.10×10^{-3}	8.97×10^{-3}
-1	5.55×10^{-3}	6.69×10^{-2}	1.08×10^{-2}	5.87×10^{-3}	8.33×10^{-3}	2.23×10^{-2}
2	1.10×10^{-3}	8.98×10^{-4}	6.27×10^{-4}	1.04×10^{-3}	6.81×10^{-4}	2.94×10^{-3}
-2	2.06×10^{-3}	1.38×10^{-3}	1.48×10^{-3}	1.21×10^{-3}	1.63×10^{-3}	4.64×10^{-3}
3	1.17×10^{-3}	1.12×10^{-3}	1.11×10^{-3}	1.25×10^{-3}	1.08×10^{-3}	3.69×10^{-3}
-3	1.17×10^{-3}	1.28×10^{-3}	1.17×10^{-3}	1.13×10^{-3}	6.47×10^{-4}	4.06×10^{-3}

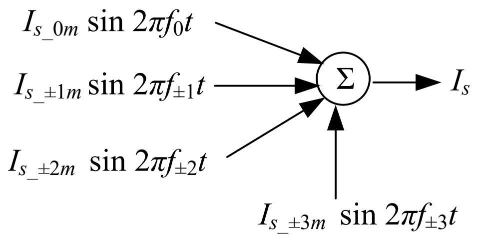

Fig. 6.3. The schematic diagram of modelling the faulty IM current signature.

Fig. 6.4 shows the simulated faulty current signatures and the torque responses respectively, using an IM with three BRBs. The torque response of the faulty IM is generated using Equation (6.6) considering the real time current signature given in Fig. 6.4(a). On the contrary, the simulated torque response is generated using Equation (6.6) based on the simulated current signature given in Fig. 6.4(b). Hence, the real time and simulated torque responses of the IM are presented in Figs. 6.4(c) and 6.4(d), respectively. Analyzing Figs. 6.4(c) and 6.4(d) it can be concluded that the simulation technique described in this section can generate torque ripples similar to the real time faulty torque response of the IM.

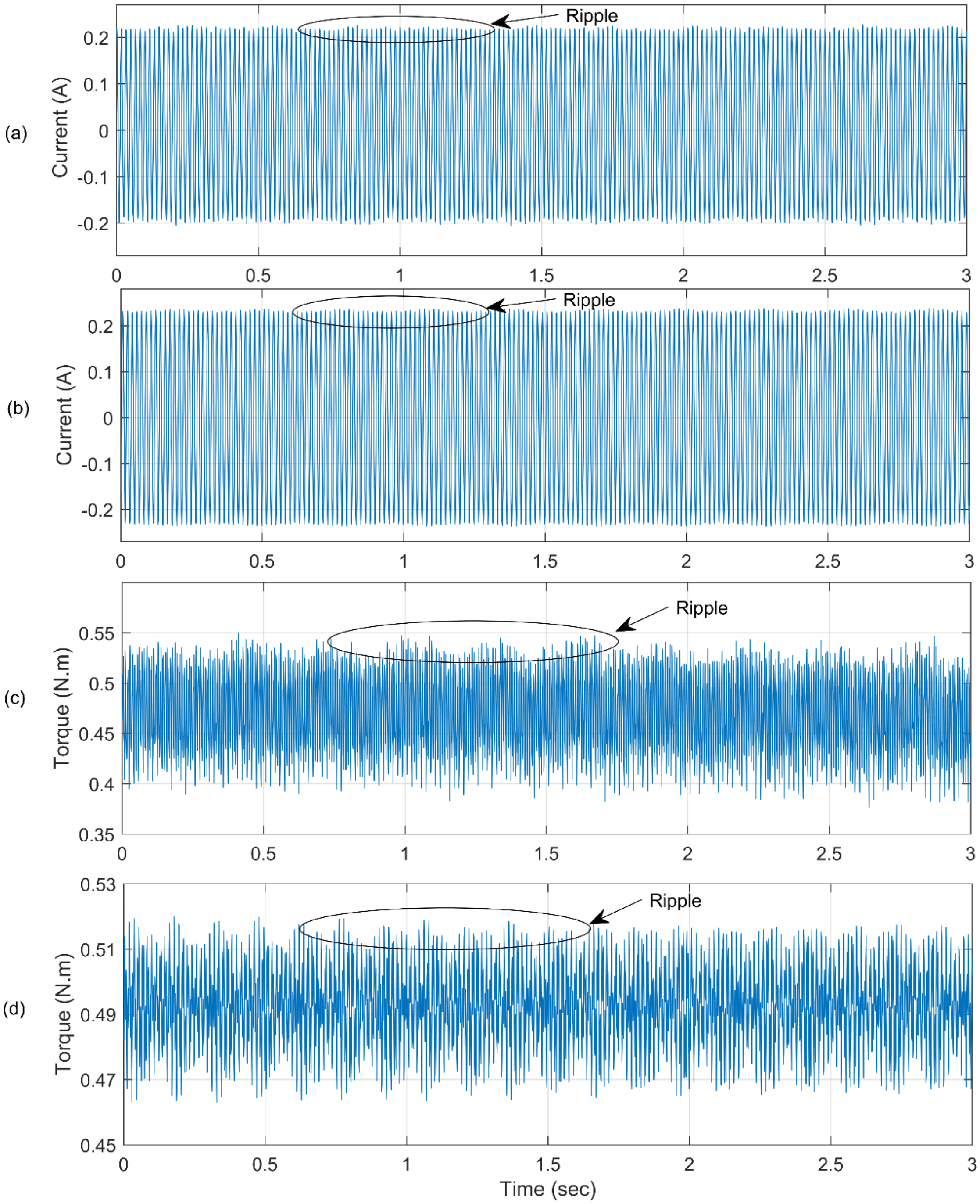

Fig. 6.4 Faulty current signatures and torque responses of IM: (a) real time current signature, (b) simulated current signature, (c) real time torque response, (d) simulated torque response.

6.4 The Proposed NF based FTC Technique

From the discussions in Sections 6.2 and 6.3, the BRB fault introduces ripples in the torque response of the IM, which may adversely affect the machine performance due to extra vibration and overheating of the IM. Hence, the proposed NF-based FTC aims to reduce the torque ripples due to BRB fault of the IM.

The arrangement of the IM with the NF based FTC technique is presented in Fig. 6.5. The proposed NF-based FTC technique can adapt its parameters considering the operational ranges of the torque of an IM. The adaptation of parameters are detailed discussed in Section 6.5 of this chapter. This adaptive technique allows the proposed FTC to reduce the torque ripple at different operating conditions during BRB fault. The specific implementation strategy of the proposed FTC will be discussed in Section 6.7.

As discussed in Chapter 2 (Section 2.4.4), the grid connected IM uses a rectifier and an inverter for the operation. The torque (T_{em}) of the IM is estimated from the operating voltage and current of the IM using Equation (6.6). The estimated T_{em} is compared with the reference torque to generate the errors for the torque (e_t and Δe_t). These errors work as inputs to the proposed NF-based FTC technique and estimate the q axis control signal (v_q) which is the output of the proposed NF based FTC technique. The q axis control voltage signal (v_q) can be adapted, by adjusting the inverters operation to reduce the torque ripples in IM operation. The training algorithms for updating the FTC system parameters will be discussed in Section 6.6 of this chapter. Furthermore, the stator flux values (ψ_s) of the IM are calculated using Equations (6.3) -(6.5), which are then utilized to generate the d axis control voltage signal (v_d) as illustrated in Fig. 6.5. The combination d axis cand q axis control voltage signals (v_d and v_q) are used to control the inverter connected to the IM.

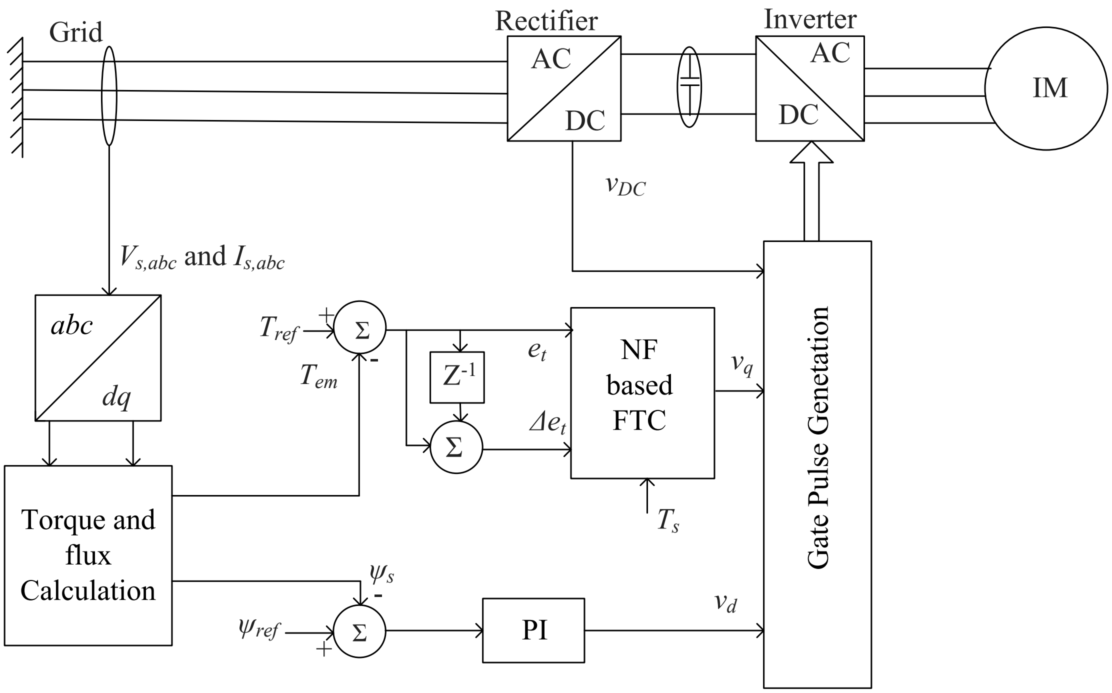

Fig. 6.5 The arrangement of the IM with the proposed NF based FTC technique.

6.5 The Architecture of the NF Network for the Proposed FTC Technique

The NF architecture of the proposed FTC technique is shown in Fig. 6.6. The layer functionality of NF network is described as below:

Layer 1: This is the input fuzzification layer. The inputs are fuzzified in this layer by using the fuzzy membership functions. For the construction of the specific NF network used in the proposed FTC two inputs of x and y are considered. Here input x represents the e_t and input y represents the quantity of Δe_t. Each input has three linear MFs as presented as

$$\mu_{Ai}(x) = \begin{cases} 0, & x \le a_i \\ \dfrac{x - a_i}{b_i - a_i}, & a_i < x < b_i \\ \dfrac{c_i - x}{c_i - b_i}, & b_i < x < c_i \end{cases} \tag{6.9}$$

$$\mu_{Bj}(y) = \begin{cases} 0, & y \le a_j \\ \dfrac{y - a_j}{b_j - a_j}, & a_j < y < b_j \\ \dfrac{c_j - y}{c_j - b_j}, & b_j < y < c_j \end{cases} \tag{6.10}$$

where *i*, *j* =1, 2, 3; The parameters {a_i, b_i, c_i} and {a_j, b_j, c_j} are the nonlinear premise parameters to be updated as discussed in Section 6.6.2.

Layer 2: This is the fuzzy composition layer. If the max-product fuzzy composition operator is used, the firing strength for the *m*-th rule (μ_m) can be determined by,

$$\mu_m = \mu_{Ai}(x)\mu_{Bj}(y) \ ,m = 1,2,\ldots,9. \tag{6.11}$$

Layer 3: This is the normalization layer. The normalized firing strength ($\bar{\mu}_m$) for each rule becomes,

$$\bar{\mu}_m = \frac{\mu_m}{\sum_{i=1}^{9}\mu_i} \tag{6.12}$$

Layer 4: For the proposed NF based FTC technique the linear parameters are optimized using the data from the different operational torque range. The training procedure for linear parameters are discussed in Section 6.6.1. The training purpose is to improve the adaptive capability of the NF system to reduce the torque ripples corresponding to different operating conditions of IM with BRB fault. Hence the NF network can adjust its linear parameters in different operating conditions, which makes it capable of reducing the torque ripple compared to the conventional FTC scheme. The parameters (γ_0^m, γ_1^m and γ_2^m) estimated at the operating torque T_{em} can be given as

$$\gamma_0^m = \sum_{l=1}^{N_l} \gamma_{0-l}^m\left[0.5 \times \tanh\big(\sigma(T_{em} - T_{min-l})\big) - 0.5 \times \tanh\big(\sigma(T_{em} - T_{max-l})\big)\right] \tag{6.13}$$

$$\gamma_1^m = \sum_{l=1}^{N_l} \gamma_{1-l}^m \left[0.5 \times \tanh\big(\sigma(T_{em} - T_{min-l})\big) - 0.5 \times \tanh\big(\sigma(T_{em} - T_{max-l})\big)\right] \tag{6.14}$$

$$\gamma_2^m = \sum_{l=1}^{N_l} \gamma_{2-l}^m \left[0.5 \times \tanh\big(\sigma(T_{em} - T_{min-l})\big) - 0.5 \times \tanh\big(\sigma(T_{em} - T_{max-l})\big)\right] \tag{6.15}$$

where $\gamma_{0-l}^m, \gamma_{1-l}^m, \gamma_{2-l}^m$ are the linear consequent parameters for *l*-th operational range of torque, *l*=1, 2, …N_l; N_l is the total torque range; T_{min-l} *and* T_{max-l} are the minimum and maximum torque values for the *l*-th range; σ should be high enough considering the operational torque ranges to estimate the parameter values accurately and σ = 10000 is considered for this analysis. For example, if we consider two consecutive torque ranges: $[T_{min-1}\ T_{max-1}]$ and $[T_{min-2}\ T_{max-2}]$ (or $l = 1, 2$), then γ_0^m can be estimated as

$$\gamma_0^m = \gamma_{0-1}^m\big[0.5 \times \tanh\big(\sigma(T_{em} - T_{min-1})\big) - 0.5 \times \tanh\big(\sigma(T_{em} - T_{max-1})\big)\big] + \gamma_{0-2}^m\big[0.5 \times \tanh\big(\sigma(T_{em} - T_{min-2})\big) - 0.5 \times \tanh\big(\sigma(T_{em} - T_{max-2})\big)\big]$$

Hence, the functional output is calculated in this layer as,

$$f_m = \gamma_0^m + \gamma_1^m x_i + \gamma_2^m y_j, \tag{6.16}$$

Layer 5: It is the defuzzification layer. The final output is calculated in this layer as

$$f_T = \bar{\mu}_1 f_1 + \bar{\mu}_2 f_2 + \cdots + \bar{\mu}_9 f_9 \tag{6.17}$$

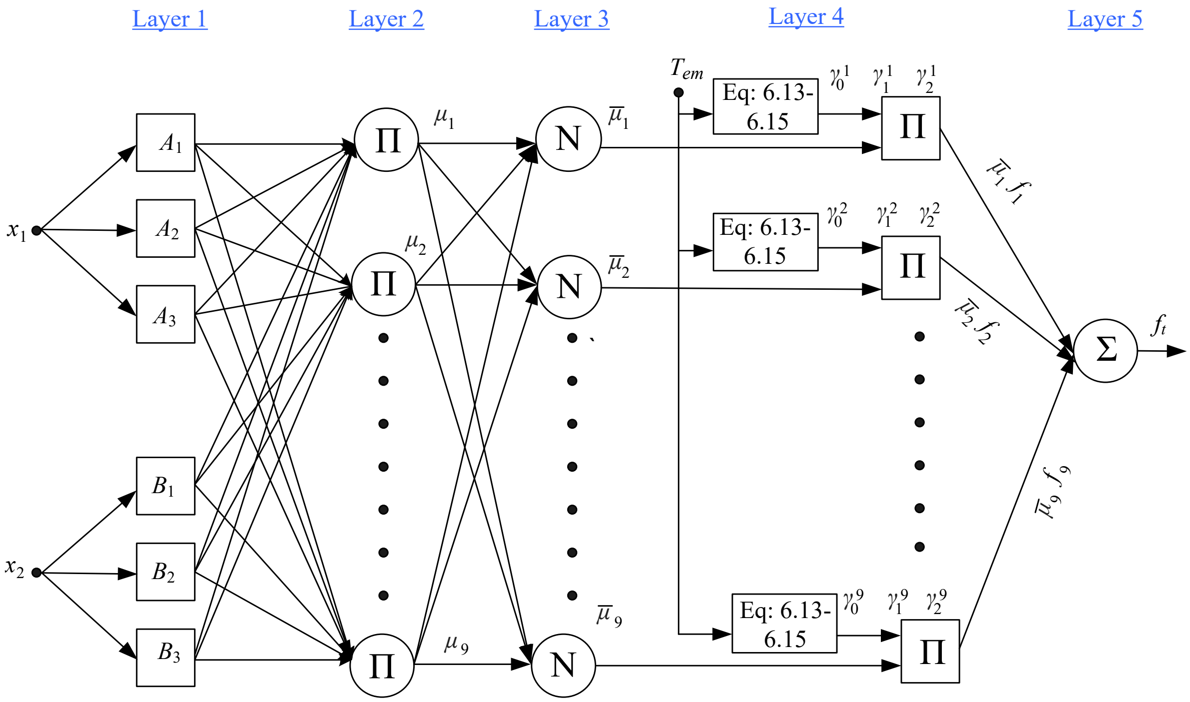

Fig. 6.6 The architecture of the NF network for the proposed FTC technique.

6.6 Training of Parameters for the NF System

The NF system has two types of parameters as linear consequent parameters and nonlinear premise parameters. The training process for both types of parameters are discussed in this section. The hybrid training algorithm will be applied to update the NF system parameters. The objective function in Equation (6.18) is formulated to reduce the difference between the theoretical and calculated output data,

$$W = \frac{1}{2}e^2 = \frac{1}{2}(y - f_T)^2 \tag{6.18}$$

where y and f_T are expected and theoretical output data, respectively.

6.6.1 Optimization of the Linear Consequent Parameters

The consequent parameters $\gamma_0^m, \gamma_1^m$and$\gamma_2^m$are trained using recursive LSE method:

$$P_{k+1} = P_k - \frac{P_k a_{k+1} a_{k+1}^T P_k}{1 + a_{k+1}^T P_k a_{k+1}} \tag{6.19}$$

$$\gamma_{j-l,k+1}^m = \gamma_{j-l,k}^m + P_{k+1} a_{k+1}(y_{k+1} - a_{k+1}^T \gamma_{j-l,k}^m) \tag{6.20}$$

where $\gamma_{j-l,k+1}^m$ represents the estimate of the optimal linear parameter values.

a_{k+1} is a vector containing the coefficients of the linear parameters to be optimized.

y_{k+1} is the actual system output.

$P_o = aI$, where a is a large number, … in this case.

$\gamma_{j-l,0}^m$is usually initialized to a vector of zeros.

m=1,2,.., 9 ; j= 0,1, 2; k=1, 2, …, N; N is the number of training data pairs; l=1, 2, …N_l; N_l is the total operational torque range. From the training process the optimized linear consequent parameters, $\gamma_{0-l}^m, \gamma_{1-l}^m, \gamma_{2-l}^m$ are obtained for l=1,2,…, N_l-th operational range of the torque. Consequently, the parameters γ_0^m, γ_1^m and γ_2^m can be estimated using Equation (6.13) to Equation (6.15) as discussed in Section 6.5. In addition, 2000 data are collected considering different operational toque conditions and 70% of the data are used for training.

6.6.2 Optimization of the Premise Parameters

The nonlinear MF parameters of proposed ANF based controllers are trained by using the gradient decent (GD) algorithm, or

$$a_i(n+1) = a_i(n) - \alpha_{ai}\frac{\partial W}{\partial a_i}$$

$$b_i(n+1) = b_i(n) - \alpha_{bi}\frac{\partial W}{\partial b_i} \tag{6.21}$$

$$C_i(n+1) = C_i(n) - \alpha_{ci}\frac{\partial W}{\partial C_i}$$

where α_{ai}, α_{bi} and α_{ci} are the learning rates of the corresponding parameters and a_i, b_i and c_i are the premise parameters to be optimized, i=1,2 ,3. The derivatives can be defined using the chain rule such as:

$$\frac{\partial W}{\partial a_i} = \frac{\partial W}{\partial f}\frac{\partial f}{\partial \mu_i}\frac{\partial \mu_i}{\partial a_i}$$

$$\frac{\partial W}{\partial b_i} = \frac{\partial W}{\partial f}\frac{\partial f}{\partial \mu_i}\frac{\partial \mu_i}{\partial b_i} \tag{6.22}$$

$$\frac{\partial W}{\partial c_i} = \frac{\partial W}{\partial f}\frac{\partial f}{\partial \mu_i}\frac{\partial \mu_i}{\partial c_i}$$

Table 6.2 Simulation parameters of the IM

Parameters	**Value**
Rated power	18.5 kW
Grid voltage(rms)	575 V
Grid frequency	60 Hz
Number of pole pairs	2
Leakage resistance	0.5968 Ω
Leakage inductance	0.35 mH
Magnetizing inductance	35 mH
DC bus capacitance	150 mF

6.7 Simulation Results and Analysis

The effectiveness of the proposed FTC technique is investigated through simulation studies in this section. The performance of the proposed FTC technique is compared to the conventional NF-based FTC technique which uses the fixed optimized parameters regardless of the operational torque as discussed in Chapter 4 (Section 4.2). Table 6.2 presents the simulation parameters of faulty IM and grid considered for this study. Three torque ranges are considered for the proposed FTC:

$l = 1$: range of T_{em}: [95, 105];

$l = 2$: range of T_{em}: [85 95]

$l = 3$: range of T_{em}: [75 85].

Figs. 6.7 - 6.9 represent the comparison between the conventional and the proposed NF based FTC technique for different torque operating conditions. To observe the torque response, the IM is controlled by using conventional-NF based FTC technique up to 2.5 sec of the simulation, and then the proposed FTC technique is applied for testing. From Fig. 6.7 it is evident that the proposed FTC can reduce the torque ripples and provide better performance compared to the conventional NF based FTC at T_{em}= 100 N.m. Figs. 6.8 and 6.9 show the respective comparison results of IM performance using these two NF FTC techniques at testing conditions of T_{em}= 90 N.m and 80 N.m, respectively. It is seen that the proposed NF-based FTC technique performs better than the conventional NF based FTC in suppressing the torque ripples for the faulty IM due to adaptation the NF system parameters based on the instantaneous operational torque of IM.

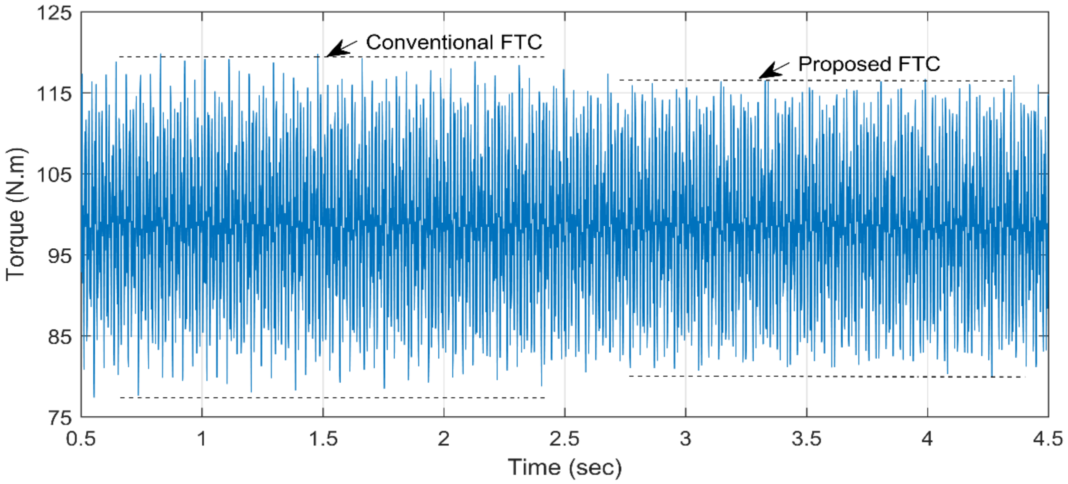

Fig. 6.7 Simulated comparative torque response between conventional and proposed FTC techniques for IM operating at T_{em}= 100 N.m.

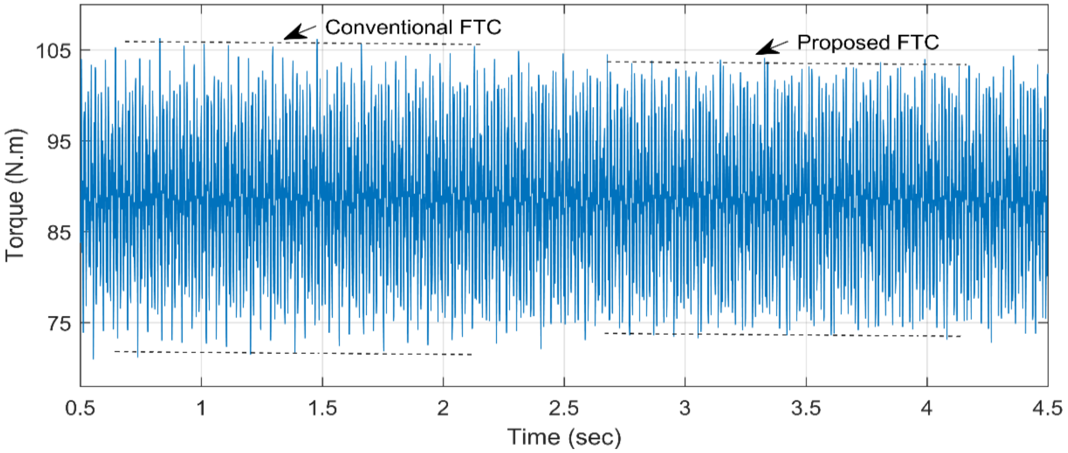

Fig. 6.8 Simulated comparative torque response between conventional and proposed FTC techniques for IM operating at T_{em}= 90 N.m.

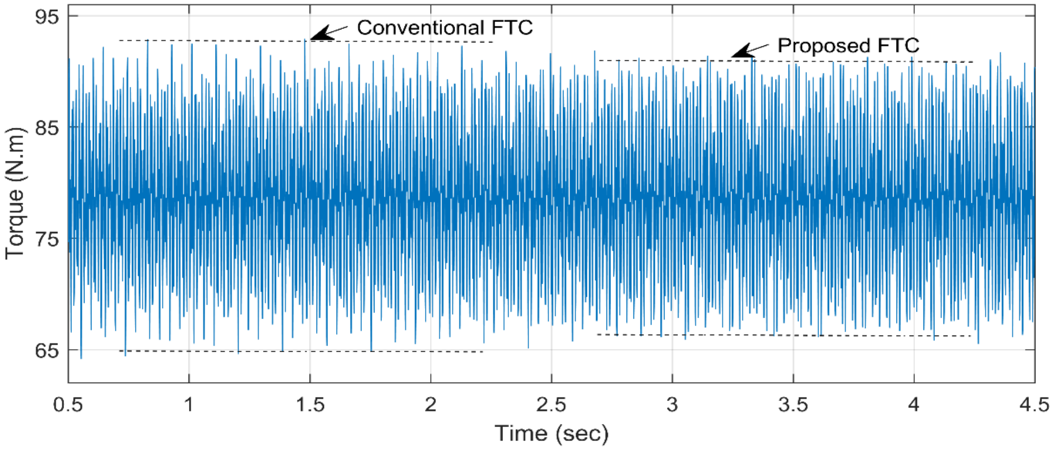

Fig. 6.9 Simulated comparative torque response between conventional and proposed FTC techniques for IM operating at T_{em}= 80 N.m.

6.8 Chapter Conclusion

A new NF based FTC technique has been presented in this chapter to cope with BRB fault of the IM. At first the torque ripple at the time of BRB fault has been analyzed considering the real time healthy and faulty current and torque data of IM. Furthermore, the NF based FTC technique has been presented and the detail NF structure used to design the FTC is discussed accordingly. The effectiveness of the proposed FTC has been investigated at different operating torque conditions at simulation environment. The simulation results, it is evident that the proposed FTC technique can reduce the torque ripple at the time of BRB fault compared to the conventional NF based FTC approach. Recently the IM has been gaining popularity as wind generators for WEC systems and hence, the developed NF based FTC technique could be a potential candidate to utilize for faulty SCIG based WEC system.

Chapter 7

Conclusion and Future Work

7.1 Conclusion

Induction machines (IMs) are commonly used in WEC system and various industrial sectors. IM defects can degrade operational performance and quality of the related machines. These IM defects can be induced by electrical, thermal or mechanical stress. It is essential to recognize IM defects at their earliest stage so as to prevent machine performance degradation and improve production quality and safety. Hence, this work focuses on IM broken rotor bar (BRB) fault detection, as BRB fault could generate extra heating, vibration, acoustics noise, or even sparks in IMs.

An EEMD technique has been presented in this thesis to improve the accuracy of signal processing-based IM BRB fault detection. The EEMD technique has applied a new similarity function, as suggested in the thesis, in order to compare IMFs with the benchmark signature to select the representative IMFs for advanced analysis. Likewise, an OAMF technique is developed and applied to the MCSA to recognize the sidebands of the characteristic frequency of the selected IMFs while employing the presented EEMD technique. The OAMF will use an adaptive window function to adjust its bandwidth and provide optimized accentuation in the sidebands of MCSA without reconstructing the original time domain signal. A novel optimization technique (MWOA) is also developed and presented in this study, with enhanced searching capability in order to reach global optima. Finally, a new post-processing method has been used to enhance representative features for BRB fault detection. The efficacy of the proposed EEMD technique has been verified experimentally.

WEC system is an effective strategy to generate electric power as it is the most cost-effective and environmentally friendly strategy. IMs are mostly used in different configurations of WEC systems. Among various WEC system configurations, the DFIG-based system is one of the most used methods due to its advantages such as variable speed wind regulations, fractional converter size, flexible and bidirectional reactive power transformation, etc. However, it is difficult to control the healthy IM based WEC system due to uncertain wind speed and nonlinear operation of the IMs as well as WEC system. Hence, in this thesis an ANF-based DTF control technique has been developed for controlling the RSC of DFIG based WEC system. The proposed ANF-based DTF control technique has exhibited superior dynamic WEC system performance by reducing torque and stator current overshoot, as well as settling time for the WEC system compared to the conventional fuzzy and PI-based control techniques. Additionally, this control technique has the capability to improve the transient condition by reducing the peak torque and stator current at the initial starting period. The effectiveness of the developed ANF-based DTF control technique has been verified firstly through simulation tests (considering the wind speed variation), as well as through transient starting conditions. Furthermore, the ANF-based DTF control technique has implemented in DS1104 board and has been applied to a laboratory prototype. The experimental results have also supported the efficacy of the proposed control technique.

In addition, an integrated neuro-fuzzy (INF)-based DTF control technique has been also developed for the DFIG-based WEC system. An INF network has been developed and analyzed and has been utilized and further applied in the developed INF-based DTF control technique. The presented INF-based DTF control technique has processed torque and flux errors to generate the control signals for RSC. The construction, assembly and operation of the INF structure has been presented systematically in this thesis. Furthermore, an ensemble training method has been developed to train the proposed INF system parameters. The INF network presented in this thesis has less computational states compared to classical NF network; it is therefore deemed suitable for the developed DTF control technique. The presented INF-based DTF control technique has shown enhanced dynamic WEC system performance compared to the conventional NF-based DTF control scheme. The effectiveness of the developed INF-based DTF control technique has been investigated through simulation as well as experimental analysis in a laboratory. Furthermore, the stability analysis of the WEC system controlled by the INF-based DTF control has been analyzed and presented in this thesis.

Moreover, the squirrel cage induction machine (SCIM) is utilized sometimes as wind generator other than DFIG. SCIM also has the usage in most of the industrial applications. However, the BRB fault occur in SCIM may adversely affect the performance of the machine. A novel NF based fault tolerant control (FTC) technique has been developed to cope with BRB fault of the IM. The proposed FTC technique can reduce the torque ripple and improve the operational performance of IM at the time of BRB fault. The operation of NF based FTC technique along with the detail NF structure have been discussed. The effectiveness of the proposed technique is verified through simulation.

7.2 List of Publications

The following publications have been made through the course of this research and development work:

1. M.S. Arifin, M.N. Uddin and W. Wang, "Neuro-Fuzzy Adaptive Direct Torque and Flux Control of a Grid-connected DFIG WECS with Improved Dynamic Performance," IEEE Transactions on Industry Applications, vol. 59, no. 6, pp. 7692-7700, Nov.-Dec. 2023, doi: 10.1109/TIA.2023.3302844.
2. M.S. Arifin, M.N. Uddin and W. Wang, "Neuro-Fuzzy Adaptive Direct Torque and Flux Control of a Grid-connected DFIG WECS with Improved Dynamic Performance," 2022 IEEE Industry Applications Society Annual Meeting (IAS), Detroit, MI, USA, 2022, pp. 1-8, doi: 10.1109/IAS54023.2022.9940061.
3. M.S. Arifin, W. Wang, and M.N. Uddin, “A Modified EMD Technique for Broken Rotor Bar Fault Detection in Induction Machines,” Sensors, vol. 24, no. 16, #5186, pp.1-16, Aug. 2024, doi: 10.3390/s24165186.
4. M.S. Arifin, W. Wang, and M.N. Uddin, “An Enhanced EMD Technique for Broken Rotor Bar Fault Detection in Induction Machines,” IEEE Transactions on Instrumentation and Measurement (under review).
5. M.S. Arifin, W. Wang, and M.N. Uddin, “A novel Adaptive EMD Technique for Broken Rotor Bar Fault Detection in Induction Machines,” The 3rd International Conference on Electronics, Energy and Measurement, 2025 (submitted).
6. M.S. Arifin, M.N. Uddin and W. Wang, “An Integrated Neuro-Fuzzy-based Direct Torque and Flux Control Scheme for DFIG WECS,” IEEE Transactions on Industry Applications (submitted).

7.3 Future Work

The future work of this thesis includes the following:

1. The algorithms related to machine learning and artificial intelligence can be applied to design intelligent controllers for the WEC system. The dynamic performance can be investigated by introducing those controllers in WEC system. Additionally, algorithms related to intelligent control can be applied in off-grid WEC system to investigate the performance of WEC system.

2. Advanced research can be undertaken into the EEMD technique to other types of IMs and on available online datasets for BRB fault detection. In addition, more research can be undertaken to adopt the EEMD for fault detection in other IM systems such as rolling element bearings.

3. The proposed NF based FTC can be applied to a real motor with BRB faults to investigate the effectiveness of the control technique experimentally.

Appendix-A

MATLAB-Simulink blocks for simulation

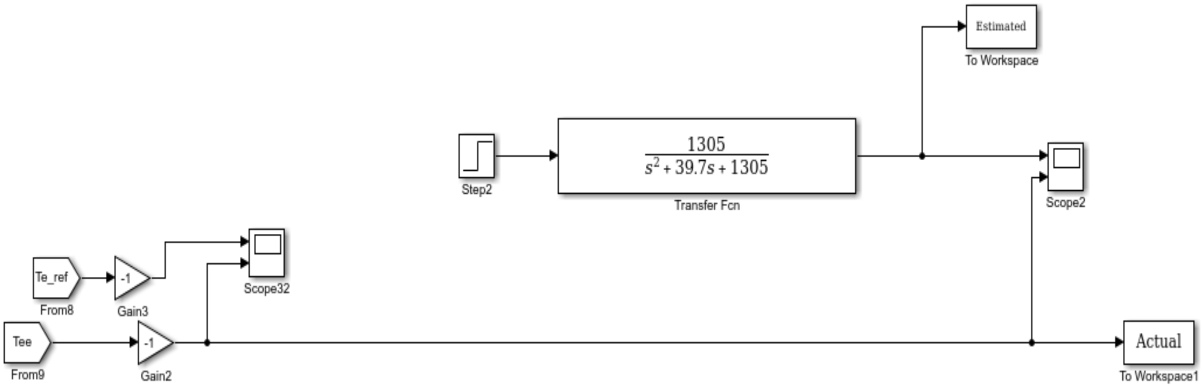

Fig. A.1 Estimate the actual and real transfer function

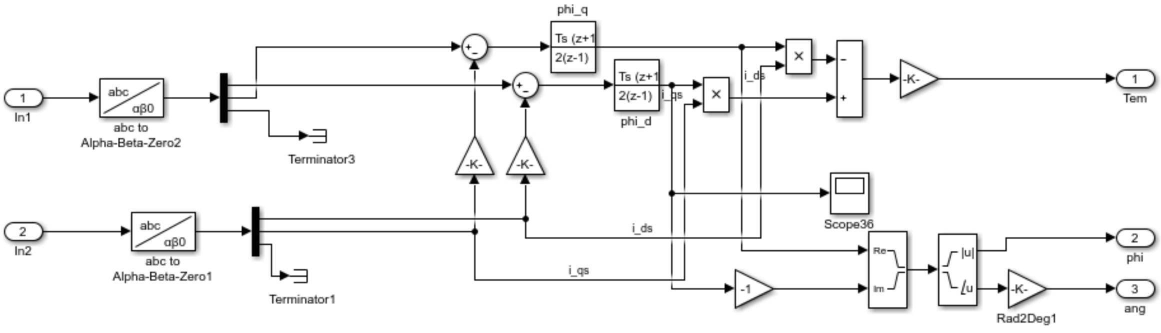

Fig. A.2 Torque and flux calculation of DFIG

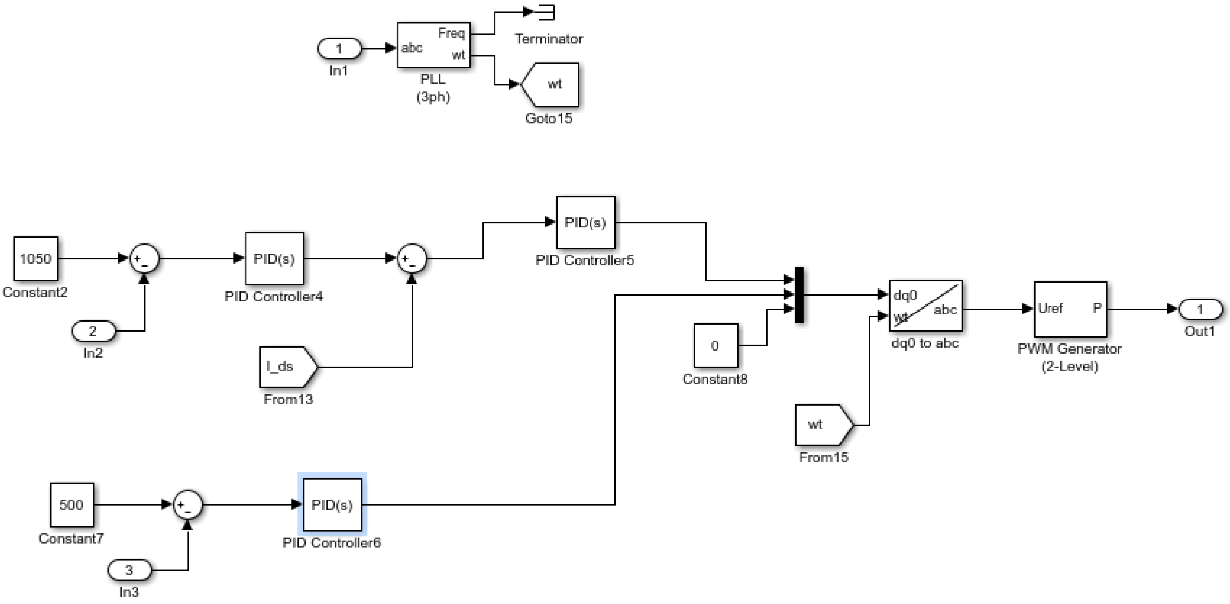

Fig. A.3 Grid side control of DFIG

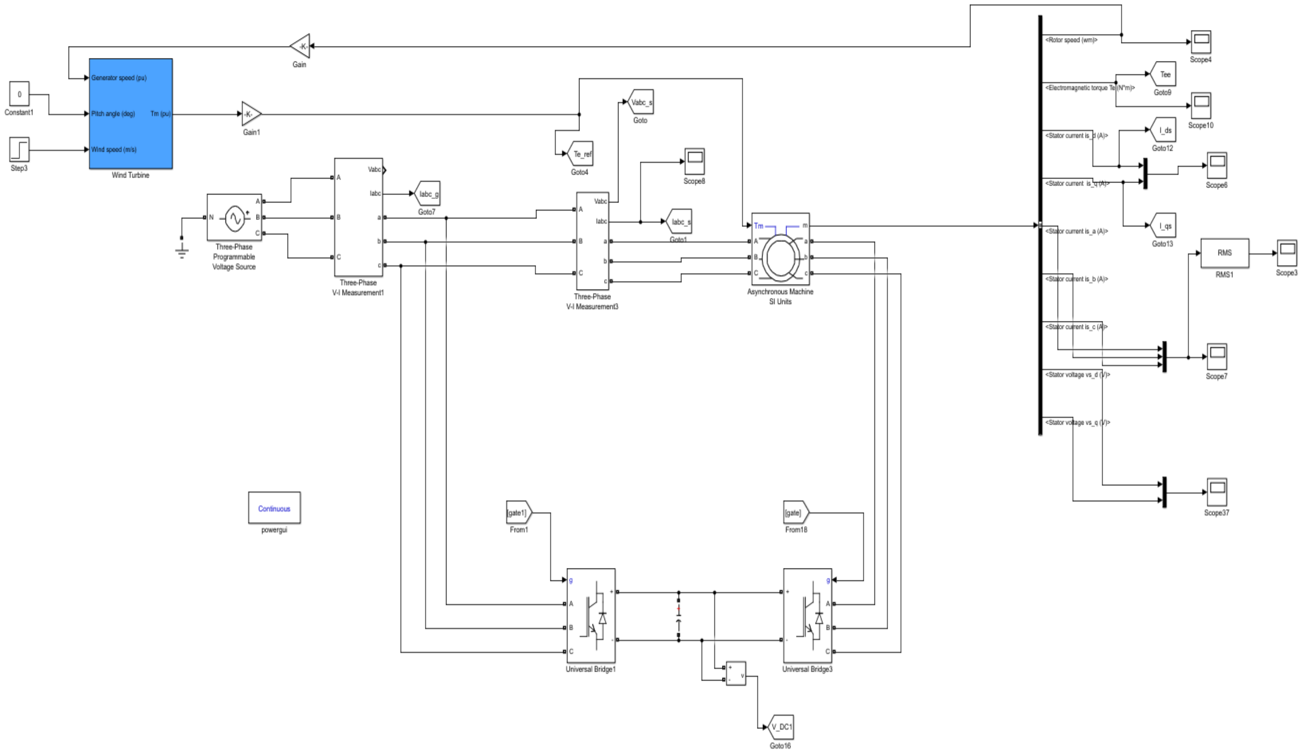

Fig. A.4 DFIG based WEC system

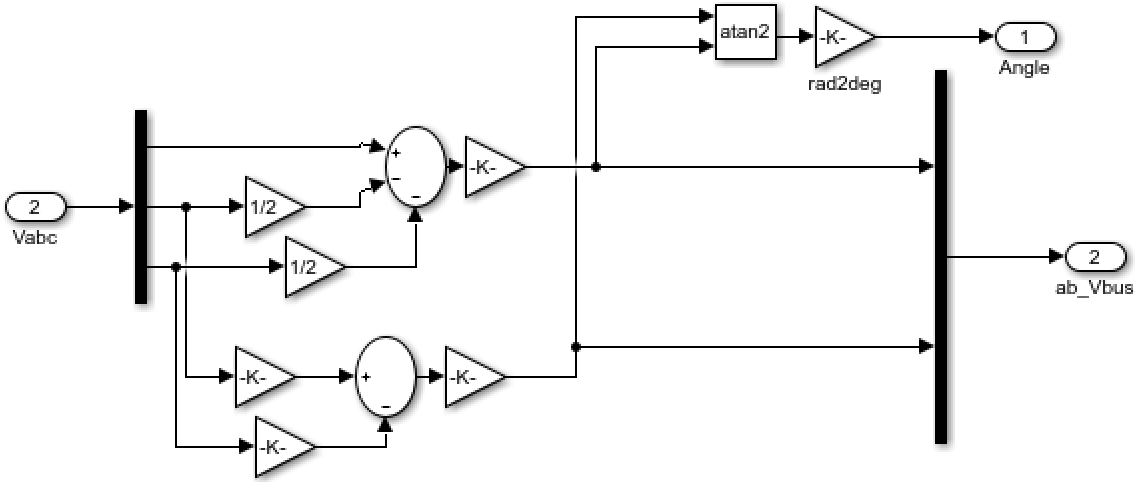

Fig. A.5 *abc* to *αβ* transformation

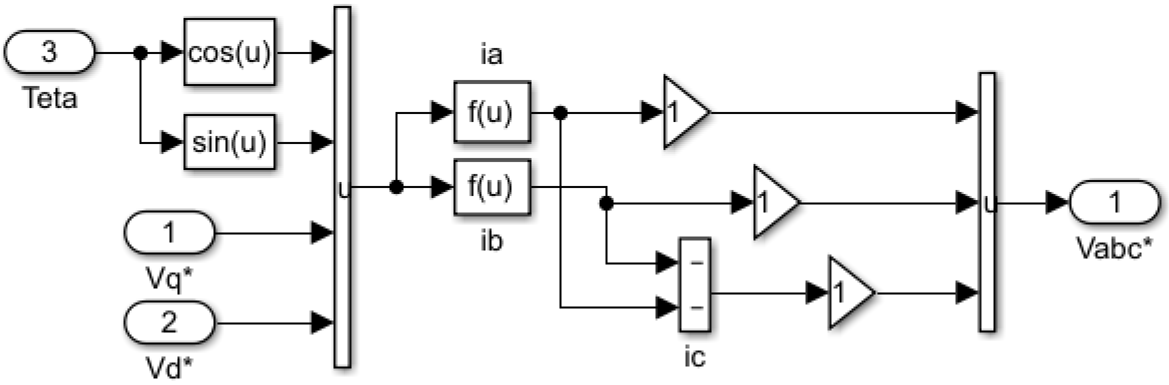

Fig. A.6 *dq* to *abc* transformation

Appendix-B

MATLAB Coding for different algorithms

Code for LSE training algorithm

```
clc;
close all;
clear all;

zz=xlsread('Data_Project.xlsx'); % First 50 data is used to
dertermine initial P and theta
z=zz(1:50,1:4);
y=zz(1:50,5); % output matrix

W1=sigmf(z,[-0.05 500]); %Non linear parameters are kept
constant
W2=sigmf(z,[0.05 500]);

W11=W1(:,1).*W1(:,2).*W1(:,3);  % returns firing strength
W22=W1(:,1).*W1(:,2).*W2(:,3);
W33=W1(:,1).*W2(:,2).*W1(:,3);
W44=W1(:,1).*W2(:,2).*W2(:,3);
W55=W2(:,1).*W1(:,2).*W1(:,3);
W66=W2(:,1).*W1(:,2).*W2(:,3);
W77=W2(:,1).*W2(:,2).*W1(:,3);
W88=W2(:,1).*W2(:,2).*W2(:,3);
W_all=W11+W22+W33+W44+W55+W66+W77+W88;

W111=W11./W_all; %normalization
W222=W22./W_all;
W333=W33./W_all;
W444=W44./W_all;
W555=W55./W_all;
W666=W66./W_all;
W777=W77./W_all;
W888=W88./W_all;

A1=W111.*z; %step for initial "A" matrix formation
A2=W222.*z;
A3=W333.*z;
A4=W444.*z;
A5=W555.*z;
A6=W666.*z;
A7=W777.*z;
A8=W888.*z;
```

```
A=[A1,A2,A3,A4,A5,A6,A7,A8];  %initial "A" matrix
theta=inv(A'*A)*A'*y; %initial
p=inv(A'*A);

% Recursive
zz=xlsread('Data_Project.xlsx'); %Last 300 data is recurcively
used
z=zz(51:350,1:4);
y=zz(51:350,5); % output matrix

W1=sigmf(z,[-0.05 500]);
W2=sigmf(z,[0.05 500]);

for i=1:300
W11=W1(i,1).*W1(i,2).*W1(i,3);
W22=W1(i,1).*W1(i,2).*W2(i,3);
W33=W1(i,1).*W2(i,2).*W1(i,3);
W44=W1(i,1).*W2(i,2).*W2(i,3);
W55=W2(i,1).*W1(i,2).*W1(i,3);
W66=W2(i,1).*W1(i,2).*W2(i,3);
W77=W2(i,1).*W2(i,2).*W1(i,3);
W88=W2(i,1).*W2(i,2).*W2(i,3);
W_all=W11+W22+W33+W44+W55+W66+W77+W88;

W111=W11./W_all;
W222=W22./W_all;
W333=W33./W_all;
W444=W44./W_all;
W555=W55./W_all;
W666=W66./W_all;
W777=W77./W_all;
W888=W88./W_all;

A1=W111.*z(i,:);
A2=W222.*z(i,:);
A3=W333.*z(i,:);
A4=W444.*z(i,:);
A5=W555.*z(i,:);
A6=W666.*z(i,:);
A7=W777.*z(i,:);
A8=W888.*z(i,:);



A(i,:)=[A1,A2,A3,A4,A5,A6,A7,A8];
```

```
B=A(i,:)';

 p=p-(p*B*B'*p)/(1+B'*p*B); % using 5.50 book by R. Jang

theta=theta+(p*B)*(y(i)-B'*theta); % using 5.50 book by R. Jang
 end
```

Code for GD training algorithm

```
clc;
close all;
clear all;
%fixed linear parameters

zz=xlsread('Data_Project.xlsx');
z=zz(:,1:4);
y=zz(:,5); % output matrix
as1=0.05;as2=0.05;as3=0.05;  % s=small
ab1=0.05;ab2=0.05;ab3=0.05;  %b=big

cs1=500;cs2=500;cs3=500;
cb1=500;cb2=500;cb3=500;

for(i=1:200)   %No of epochs
    for (j=1: size(z,1))

W1(j,1)=sigmf(z(j,1),[-as1 cs1]);
W1(j,2)=sigmf(z(j,2),[-as2 cs2]);
W1(j,3)=sigmf(z(j,3),[-as3 cs3]);

W2(j,1)=sigmf(z(j,1),[ab1 cb1]);
W2(j,2)=sigmf(z(j,2),[ab2 cb2]);
W2(j,3)=sigmf(z(j,3),[ab3 cb3]);


W11=W1(j,1)*W1(j,2)*W1(j,3);  %product firing strength
W22=W1(j,1)*W1(j,2)*W2(j,3);
W33=W1(j,1)*W2(j,2)*W1(j,3);
W44=W1(j,1)*W2(j,2)*W2(j,3);
W55=W2(j,1)*W1(j,2)*W1(j,3);
W66=W2(j,1)*W1(j,2)*W2(j,3);
W77=W2(j,1)*W2(j,2)*W1(j,3);
W88=W2(j,1)*W2(j,2)*W2(j,3);
W_all=W11+W22+W33+W44+W55+W66+W77+W88;



W111=W11/W_all;
```

```
W222=W22/W_all;
W333=W33/W_all;
W444=W44/W_all;
W555=W55/W_all;
W666=W66/W_all;
W777=W77/W_all;
W888=W88/W_all;

f1=W111*(z(j,:)*theta(1:4,:));
f2=W222*(z(j,:)*theta(5:8,:));
f3=W333*(z(j,:)*theta(9:12,:));
f4=W444*(z(j,:)*theta(13:16,:));
f5=W555*(z(j,:)*theta(17:20,:));
f6=W666*(z(j,:)*theta(21:24,:));
f7=W777*(z(j,:)*theta(25:28,:));
f8=W888*(z(j,:)*theta(29:32,:));

f=f1+f2+f3+f4+f5+f6+f7+f8;


dE_df= f-y(j,1);
dfW11=(f1-f)/W_all;
dfW22=(f2-f)/W_all;
dfW33=(f3-f)/W_all;
dfW44=(f4-f)/W_all;
dfW55=(f5-f)/W_all;
dfW66=(f6-f)/W_all;
dfW77=(f7-f)/W_all;
dfW88=(f8-f)/W_all;


dmus1_as1=(z(j,1)-cs1)*W1(j,1)*(1-W1(j,1));
dmus2_as2=(z(j,2)-cs2)*W1(j,2)*(1-W1(j,2));
dmus3_as3=(z(j,3)-cs3)*W1(j,3)*(1-W1(j,3));
dmub1_ab1=(z(j,1)-cb1)*W2(j,1)*(1-W2(j,1));
dmub2_ab2=(z(j,2)-cb2)*W2(j,2)*(1-W2(j,2));
dmub3_ab3=(z(j,3)-cb3)*W2(j,3)*(1-W2(j,3));


dmus1_cs1=-as1*W1(j,1)*(1-W1(j,1));
dmus2_cs2=-as2*W1(j,2)*(1-W1(j,2));
dmus3_cs3=-as3*W1(j,3)*(1-W1(j,3));
dmub1_cb1=-ab1*W2(j,1)*(1-W2(j,1));
dmub2_cb2=-ab2*W2(j,2)*(1-W2(j,2));
dmub3_cb3=-ab3*W2(j,3)*(1-W2(j,3));
```

```
df_mus1=dfW11*W1(j,2)*W1(j,3)+dfW22*W1(j,2)*W2(j,3)+dfW33*W2(j,2
)*W1(j,3)+dfW44*W2(j,2)*W2(j,3);
df_mus2=dfW11*W1(j,1)*W1(j,3)+dfW22*W1(j,1)*W2(j,3)+dfW55*W2(j,1
)*W1(j,3)+dfW66*W2(j,1)*W2(j,3);
df_mus3=dfW11*W1(j,1)*W1(j,2)+dfW33*W1(j,1)*W2(j,2)+dfW55*W2(j,1
)*W1(j,2)+dfW77*W2(j,1)*W2(j,2);
df_mub1=dfW55*W1(j,2)*W1(j,3)+dfW66*W1(j,2)*W2(j,3)+dfW77*W2(j,2
)*W1(j,3)+dfW88*W2(j,2)*W2(j,3);
df_mub2=dfW33*W1(j,1)*W1(j,3)+dfW44*W1(j,1)*W2(j,3)+dfW77*W2(j,1
)*W1(j,3)+dfW88*W2(j,1)*W2(j,3);
df_mub3=dfW22*W1(j,1)*W1(j,2)+dfW44*W1(j,1)*W2(j,2)+dfW66*W2(j,1
)*W1(j,2)+dfW88*W2(j,1)*W2(j,2);

de_das1= dE_df*df_mus1*dmus1_as1;
de_das2= dE_df*df_mus2*dmus2_as2;
de_das3= dE_df*df_mus3*dmus3_as3;

de_dab1= dE_df*df_mub1*dmub1_ab1;
de_dab2= dE_df*df_mub2*dmub2_ab2;
de_dab3= dE_df*df_mub3*dmub3_ab3;


de_dcs1= dE_df*df_mus1*dmus1_cs1;
de_dcs2= dE_df*df_mus2*dmus2_cs2;
de_dcs3= dE_df*df_mus3*dmus3_cs3;

de_dcb1= dE_df*df_mub1*dmub1_cb1;
de_dcb2= dE_df*df_mub2*dmub2_cb2;
de_dcb3= dE_df*df_mub3*dmub3_cb3;


as1=as1-0.0001*de_das1;
as2=as2-0.0001*de_das2;
as3=as3-0.0001*de_das3;


ab1=ab1-0.0001*de_dab1;
ab2=ab2-0.0001*de_dab2;
ab3=ab3-0.0001*de_dab3;


cs1=cs1-0.5*de_dcs1;
cs2=cs2-0.5*de_dcs2;
cs3=cs3-0.5*de_dcs3;
cb1=cb1-0.5*de_dcb1;
cb2=cb2-0.5*de_dcb2;
cb3=cb3-0.5*de_dcb3;
```

```
error(j)=0.5*(f-y(j,1))^2;

 end
Ec(i)=sum(error);
if Ec(i)<=0.00001
 break;
end
end
plot (Ec);
```

Code for optimized NF system

```
clear all;
clc;
close all;

zz=xlsread('Testing_data.xlsx');

z=zz(:,1:4);
y=zz(:,5); %targeted data

%optimized parameters
theta=[0.0006;0.0003;0.0003;-
0.1018;0.0002;0.0004;0.0004;0.0186;0.0003;0.0003;
    0.0004;0.0162;0.0005;0.0005;0.0003;-
0.0974;0.0005;0.0004;0.0005;-0.2167;
    0.0004;0.0002;0.0004;0.0057;0.0004;0.0004;0.0005;-
0.1408;0.0005;0.0001;0.0005;-0.0883];

as1=0.0383;as2=0.0614;as3=0.0826;
ab1=0.0098;ab2=0.0487;ab3=0.0775;

cs1=499.74;cs2=499.67;cs3=499.66;
cb1=499.86;cb2=499.69;cb3=499.81;

%***********MF************
W1(:,1)=sigmf(z(:,1),[-as1 cs1]);
W1(:,2)=sigmf(z(:,2),[-as2 cs2]);
W1(:,3)=sigmf(z(:,3),[-as3 cs3]);

W2(:,1)=sigmf(z(:,1),[ab1 cb1]);
W2(:,2)=sigmf(z(:,2),[ab2 cb2]);
W2(:,3)=sigmf(z(:,3),[ab3 cb3]);


W11=W1(:,1).*W1(:,2).*W1(:,3);  %Rules and firing strength
W22=W1(:,1).*W1(:,2).*W2(:,3);
```

```
W33=W1(:,1).*W2(:,2).*W1(:,3);
W44=W1(:,1).*W2(:,2).*W2(:,3);
W55=W2(:,1).*W1(:,2).*W1(:,3);
W66=W2(:,1).*W1(:,2).*W2(:,3);
W77=W2(:,1).*W2(:,2).*W1(:,3);
W88=W2(:,1).*W2(:,2).*W2(:,3);
W_all=W11+W22+W33+W44+W55+W66+W77+W88;


W111=W11./W_all;  %Normalization
W222=W22./W_all;
W333=W33./W_all;
W444=W44./W_all;
W555=W55./W_all;
W666=W66./W_all;
W777=W77./W_all;
W888=W88./W_all;


f1=z*theta(1:4,:);
f2=z*theta(5:8,:);
f3=z*theta(9:12,:);
f4=z*theta(13:16,:);
f5=z*theta(17:20,:);
f6=z*theta(21:24,:);
f7=z*theta(25:28,:);
f8=z*theta(29:32,:);

f11=W111.*f1;
f22=W222.*f2;
f33=W333.*f3;
f44=W444.*f4;
f55=W555.*f5;
f66=W666.*f6;
f77=W777.*f7;
f88=W888.*f8;

f=f11+f22+f33+f44+f55+f66+f77+f88;
```

References

[1] M. Mahmud and W. Wang, “A Smart Sensor-Based cEMD Technique for Rotor Bar Fault Detection in Induction Motors,” *IEEE Trans. Instrum. Meas.*, vol. 70, pp. 1–11, 2021, doi: 10.1109/TIM.2021.3107009.

[2] X. Liang, M. Z. Ali, and H. Zhang, “Induction Motors Fault Diagnosis Using Finite Element Method: A Review,” *IEEE Trans. Ind. Appl.*, vol. 56, no. 2, pp. 1205–1217, Mar. 2020, doi: 10.1109/TIA.2019.2958908.

[3] H. Shao *et al.*, “Stability Enhancement and Direct Speed Control of DFIG Inertia Emulation Control Strategy,” *IEEE Access*, vol. 7, pp. 120089–120105, 2019, doi: 10.1109/ACCESS.2019.2937180.

[4] C. Wu, P. Cheng, H. Nian, and F. Blaabjerg, “Rotor Current Oriented Control Method of DFIG-DC System Without Stator Side Sensors,” *IEEE Trans. Ind. Electron.*, vol. 67, no. 11, pp. 9958–9962, Nov. 2020, doi: 10.1109/TIE.2019.2956415.

[5] V. R. F. B. De Souza, L. S. Barros, F. B. Costa, and G. P. D. S. Junior, “Doubly Fed Induction Generator Low Voltage Ride Through Improvement Through Modular Multilevel Converter,” *IEEE Access*, vol. 10, pp. 57914–57929, 2022, doi: 10.1109/ACCESS.2022.3178960.

[6] P. Luong and W. Wang, “Smart Sensor-Based Synergistic Analysis for Rotor Bar Fault Detection of Induction Motors,” *IEEEASME Trans. Mechatron.*, vol. 25, no. 2, pp. 1067–1075, Apr. 2020, doi: 10.1109/TMECH.2020.2970274.

[7] R. Munje and D. Sonje, *Rotor Cage Fault Detection in Induction Motors by Motor Current Signature Analysis*. 2012.

[8] A. Shukla, M. Mahmud, and W. Wang, “A smart sensor-based monitoring system for vibration measurement and bearing fault detection,” *Meas. Sci. Technol.*, vol. 31, no. 10, p. 105104, Jul. 2020, doi: 10.1088/1361-6501/ab8dfc.

[9] G. Niu, X. Dong, and Y. Chen, “Motor Fault Diagnostics Based on Current Signatures: A Review,” *IEEE Trans. Instrum. Meas.*, vol. 72, pp. 1–19, 2023, doi: 10.1109/TIM.2023.3285999.

[10] C. G. Dias and I. E. Chabu, “Spectral Analysis Using a Hall Effect Sensor for Diagnosing Broken Bars in Large Induction Motors,” *IEEE Trans. Instrum. Meas.*, vol. 63, no. 12, pp. 2890–2902, Dec. 2014, doi: 10.1109/TIM.2014.2328184.

[11] J. R. Rivera-Guillen, J. J. De Santiago-Perez, J. P. Amezquita-Sanchez, M. Valtierra-Rodriguez, and R. J. Romero-Troncoso, “Enhanced FFT-based method for incipient broken rotor bar detection in induction motors during the startup transient,” *Measurement*, vol. 124, pp. 277–285, Aug. 2018, doi: 10.1016/j.measurement.2018.04.039.

[12] S. Halder, S. Bhat, D. Zychma, and P. Sowa, “Broken Rotor Bar Fault Diagnosis Techniques Based on Motor Current Signature Analysis for Induction Motor—A Review,” *Energies*, vol. 15, no. 22, Art. no. 22, Jan. 2022, doi: 10.3390/en15228569.

[13] A. Saghafinia, S. Kahourzade, A. Mahmoudi, W. P. Hew, and M. N. Uddin, “On line trained fuzzy logic and adaptive continuous wavelet transform based high precision fault detection of IM with broken rotor bars,” in *2012 IEEE Industry Applications Society Annual Meeting*, Oct. 2012, pp. 1–8. doi: 10.1109/IAS.2012.6374027.

[14] B. D. Eddine Cherif, A. Bendiabdellah, and S. Seninete, “Induction Motor Diagnosis with Broken Rotor Bar Faults Using DWT Technique,” in *2021 International Conference on Electrical, Communication, and Computer Engineering (ICECCE)*, Jun. 2021, pp. 1–5. doi: 10.1109/ICECCE52056.2021.9514085.

[15] Md. M. Rahman and M. N. Uddin, “Online Unbalanced Rotor Fault Detection of an IM Drive Based on Both Time and Frequency Domain Analyses,” *IEEE Trans. Ind. Appl.*, vol. 53, no. 4, pp. 4087–4096, Jul. 2017, doi: 10.1109/TIA.2017.2691736.

[16] M. Abd-el-Malek, A. K. Abdelsalam, and O. E. Hassan, “Induction motor broken rotor bar fault location detection through envelope analysis of start-up current using Hilbert transform,” *Mech. Syst. Signal Process.*, vol. 93, pp. 332–350, Sep. 2017, doi: 10.1016/j.ymssp.2017.02.014.

[17] M. S. Arifin, W. Wang, and M. N. Uddin, “A Modified EMD Technique for Broken Rotor Bar Fault Detection in Induction Machines,” *Sensors*, vol. 24, no. 16, Art. no. 16, Jan. 2024, doi: 10.3390/s24165186.

[18] H. Li, G. Feng, D. Zhen, F. Gu, and A. D. Ball, “A Normalized Frequency-Domain Energy Operator for Broken Rotor Bar Fault Diagnosis,” *IEEE Trans. Instrum. Meas.*, vol. 70, pp. 1–10, 2021, doi: 10.1109/TIM.2020.3009011.

[19] M. Lopez-Ramirez, C. Rodriguez-Donate, L. M. Ledesma-Carrillo, F. J. Villalobos-Pina, J. U. Munoz-Minjares, and E. Cabal-Yepez, “Walsh–Hadamard Domain-Based Intelligent Online Fault Diagnosis of Broken Rotor Bars in Induction Motors,” *IEEE Trans. Instrum. Meas.*, vol. 71, pp. 1–11, 2022, doi: 10.1109/TIM.2022.3141152.

[20] V. Fernandez-Cavero, J. Pons-Llinares, O. Duque-Perez, and D. Morinigo-Sotelo, “Detection of broken rotor bars in non-linear startups of inverter-fed induction motors,” in *2019 IEEE 12th International Symposium on Diagnostics for Electrical Machines, Power Electronics and Drives (SDEMPED)*, Aug. 2019, pp. 309–315. doi: 10.1109/DEMPED.2019.8864846.

[21] R. Alimardani, A. Rahideh, and S. Hedayati Kia, “Mixed Eccentricity Fault Detection for Induction Motors Based on Time Synchronous Averaging of Vibration Signals,” *IEEE Trans. Ind. Electron.*, vol. 71, no. 3, pp. 3173–3181, Mar. 2024, doi: 10.1109/TIE.2023.3266589.

[22] P. Wang, K. Wang, and L. Chen, “Broken Rotor Bars Detection in Inverter-Fed Induction Motors Under Continuous Switching of Different Speed Modes,” *IEEE Trans. Ind. Electron.*, vol. 71, no. 1, pp. 975–984, Jan. 2024, doi: 10.1109/TIE.2022.3225851.

[23] M. Ma, Z. Cao, H. Fu, W. Xu, and J. Dai, “Sparse Bayesian Learning Approach for Broken Rotor Bar Fault Diagnosis,” *IEEE Trans. Instrum. Meas.*, vol. 72, pp. 1–10, 2023, doi: 10.1109/TIM.2023.3303505.

[24] K. Yatsugi, S. E. Pandarakone, Y. Mizuno, and H. Nakamura, “Common Diagnosis Approach to Three-Class Induction Motor Faults Using Stator Current Feature and Support Vector Machine,” *IEEE Access*, vol. 11, pp. 24945–24952, 2023, doi: 10.1109/ACCESS.2023.3254914.

[25] Z. Hosseinpoor, M. M. Arefi, R. Razavi-Far, N. Mozafari, and S. Hazbavi, “Virtual Sensors for Fault Diagnosis: A Case of Induction Motor Broken Rotor Bar,” *IEEE Sens. J.*, vol. 21, no. 4, pp. 5044–5051, Feb. 2021, doi: 10.1109/JSEN.2020.3033754.

[26] M.-Q. Tran, M.-K. Liu, Q.-V. Tran, and T.-K. Nguyen, “Effective Fault Diagnosis Based on Wavelet and Convolutional Attention Neural Network for Induction Motors,” *IEEE Trans. Instrum. Meas.*, vol. 71, pp. 1–13, 2022, doi: 10.1109/TIM.2021.3139706.

[27] M. Z. Ali, M. N. S. K. Shabbir, X. Liang, Y. Zhang, and T. Hu, “Machine Learning-Based Fault Diagnosis for Single- and Multi-Faults in Induction Motors Using Measured Stator Currents and Vibration Signals,” *IEEE Trans. Ind. Appl.*, vol. 55, no. 3, pp. 2378–2391, May 2019, doi: 10.1109/TIA.2019.2895797.

[28] D. Pasqualotto and M. Zigliotto, “Increasing Feasibility of Neural Network-Based Early Fault Detection in Induction Motor Drives,” *IEEE J. Emerg. Sel. Top. Power Electron.*, vol. 10, no. 2, pp. 2042–2051, Apr. 2022, doi: 10.1109/JESTPE.2021.3115170.

[29] A. Mohammad-Alikhani, B. Nahid-Mobarakeh, and M.-F. Hsieh, “One-Dimensional LSTM-Regulated Deep Residual Network for Data-Driven Fault Detection in Electric Machines,” *IEEE Trans. Ind. Electron.*, vol. 71, no. 3, pp. 3083–3092, Mar. 2024, doi: 10.1109/TIE.2023.3265054.

[30] Y. Shu, W. Zhang, X. Song, G. Liu, and Q. Jiang, “DBF-CNN: A Double-Branch Fusion Residual CNN for Diagnosis of Induction Motor Broken Rotor Bar,” *IEEE Trans. Instrum. Meas.*, vol. 72, pp. 1–10, 2023, doi: 10.1109/TIM.2023.3325863.

[31] S. A. Saleh and E. Ozkop, “Phaselet-Based Method for Detecting Electric Faults in 3\phi Induction Motor Drives—Part I: Analysis and Development,” *IEEE Trans. Ind. Appl.*, vol. 53, no. 3, pp. 2976–2987, May 2017, doi: 10.1109/TIA.2016.2608945.

[32] S. A. Saleh and E. Ozkop, “Phaselet-Based Method for Detecting Electric Faults in 3\phi Induction Motor Drives—Part II: Performance Evaluation,” *IEEE Trans. Ind. Appl.*, vol. 53, no. 3, pp. 2988–2996, May 2017, doi: 10.1109/TIA.2016.2608952.

[33] V. Sharma and A. Parey, “Frequency domain averaging based experimental evaluation of gear fault without tachometer for fluctuating speed conditions,” *Mech. Syst. Signal Process.*, vol. 85, pp. 278–295, Feb. 2017, doi: 10.1016/j.ymssp.2016.08.015.

[34] W. D. Mark, H. Lee, R. Patrick, and J. D. Coker, “A simple frequency-domain algorithm for early detection of damaged gear teeth,” *Mech. Syst. Signal Process.*, vol. 24, no. 8, pp. 2807–2823, Nov. 2010, doi: 10.1016/j.ymssp.2010.04.004.

[35] K. Y. Sanliturk and O. Cakar, “Noise elimination from measured frequency response functions,” *Mech. Syst. Signal Process.*, vol. 19, no. 3, pp. 615–631, May 2005, doi: 10.1016/j.ymssp.2004.04.005.

[36] H. Xing and J. Hou, “A Noise Elimination Method for ECG Signals,” in *2009 3rd International Conference on Bioinformatics and Biomedical Engineering*, Jun. 2009, pp. 1–3. doi: 10.1109/ICBBE.2009.5162206.

[37] A. K. Ziarani and A. Konrad, “A nonlinear adaptive method of elimination of power line interference in ECG signals,” *IEEE Trans. Biomed. Eng.*, vol. 49, no. 6, pp. 540–547, Jun. 2002, doi: 10.1109/TBME.2002.1001968.

[38] G. Singh and V. N. A. Naikan, “Detection of half broken rotor bar fault in VFD driven induction motor drive using motor square current MUSIC analysis,” *Mech. Syst. Signal Process.*, vol. 110, pp. 333–348, Sep. 2018, doi: 10.1016/j.ymssp.2018.03.001.

[39] M. H. Nadimi-Shahraki, H. Zamani, Z. Asghari Varzaneh, and S. Mirjalili, “A Systematic Review of the Whale Optimization Algorithm: Theoretical Foundation, Improvements, and Hybridizations,” *Arch. Comput. Methods Eng.*, vol. 30, no. 7, pp. 4113–4159, Sep. 2023, doi: 10.1007/s11831-023-09928-7.

[40] J. Liu, J. Shi, F. Hao, and M. Dai, “A novel enhanced global exploration whale optimization algorithm based on Lévy flights and judgment mechanism for global continuous optimization problems,” *Eng. Comput.*, vol. 39, no. 4, pp. 2433–2461, Aug. 2023, doi: 10.1007/s00366-022-01638-1.

[41] D. Cao, Y. Xu, Z. Yang, H. Dong, and X. Li, “An enhanced whale optimization algorithm with improved dynamic opposite learning and adaptive inertia weight strategy,” *Complex Intell. Syst.*, vol. 9, no. 1, pp. 767–795, Feb. 2023, doi: 10.1007/s40747-022-00827-1.

[42] Y. Sun, T. Yang, and Z. Liu, “A whale optimization algorithm based on quadratic interpolation for high-dimensional global optimization problems,” *Appl. Soft Comput.*, vol. 85, p. 105744, Dec. 2019, doi: 10.1016/j.asoc.2019.105744.

[43] W. Meng, Q. Yang, and Y. Sun, “Guaranteed Performance Control of DFIG Variable-Speed Wind Turbines,” *IEEE Trans. Control Syst. Technol.*, vol. 24, no. 6, pp. 2215–2223, Nov. 2016, doi: 10.1109/TCST.2016.2524531.

[44] R. M. Prasad and M. A. Mulla, "Rotor Position-Sensorless Algorithms for Direct Power Control of Rotor-Tied DFIG," *IEEE Trans. Power Electron.*, vol. 36, no. 6, pp. 6213–6217, Jun. 2021, doi: 10.1109/TPEL.2020.3040705.

[45] W. Gul, Q. Gao, and W. Lenwari, "Optimal Design of a 5-MW Double-Stator Single-Rotor PMSG for Offshore Direct Drive Wind Turbines," *IEEE Trans. Ind. Appl.*, vol. 56, no. 1, pp. 216–225, Jan. 2020, doi: 10.1109/TIA.2019.2949545.

[46] M. F. M. Arani and Y. A.-R. I. Mohamed, "Assessment and Enhancement of a Full-Scale PMSG-Based Wind Power Generator Performance Under Faults," *IEEE Trans. Energy Convers.*, vol. 31, no. 2, pp. 728–739, Jun. 2016, doi: 10.1109/TEC.2016.2526618.

[47] M. E. Zarei, C. V. Nicolás, J. R. Arribas, and D. Ramírez, "Four-Switch Three-Phase Operation of Grid-Side Converter of Doubly Fed Induction Generator With Three Vectors Predictive Direct Power Control Strategy," *IEEE Trans. Ind. Electron.*, vol. 66, no. 10, pp. 7741–7752, Oct. 2019, doi: 10.1109/TIE.2018.2880672.

[48] H. Shao *et al.*, "Stability Enhancement and Direct Speed Control of DFIG Inertia Emulation Control Strategy," *IEEE Access*, vol. 7, pp. 120089–120105, 2019, doi: 10.1109/ACCESS.2019.2937180.

[49] M. N. Uddin, Md. S. Arifin, and N. Rezaei, "A Novel Neuro-Fuzzy Based Direct Power Control of a DFIG Based Wind Farm Incorporated With Distance Protection Scheme and LVRT Capability," *IEEE Trans. Ind. Appl.*, vol. 59, no. 5, pp. 5792–5803, Sep. 2023, doi: 10.1109/TIA.2023.3289441.

[50] M. N. Uddin, Md. S. Arifin, and N. Rezaei, "A Novel Neuro-Fuzzy Based Direct Power Control of a DFIG based Wind Farm Incorporated with Distance Protection Scheme and LVRT Capability," in *2022 IEEE Industry Applications Society Annual Meeting (IAS)*, Oct. 2022, pp. 01–08. doi: 10.1109/IAS54023.2022.9939684.

[51] Md. S. Arifin, M. N. Uddin, and W. Wang, "Neuro-Fuzzy Adaptive Direct Torque and Flux Control of a Grid-Connected DFIG-WECS With Improved Dynamic Performance," *IEEE Trans. Ind. Appl.*, vol. 59, no. 6, pp. 7692–7700, Nov. 2023, doi: 10.1109/TIA.2023.3302844.

[52] Md. S. Arifin, M. N. Uddin, and W. Wang, "Neuro-Fuzzy Adaptive Direct Torque and Flux Control of a Grid Connected DFIG-WECS with Improved Dynamic Performance," in *2022*

IEEE Industry Applications Society Annual Meeting (IAS), Oct. 2022, pp. 1–8. doi: 10.1109/IAS54023.2022.9940061.

[53] M. N. Uddin, N. Rezaei, and Md. S. Arifin, “Hybrid Machine Learning-Based Intelligent Distance Protection and Control Schemes With Fault and Zonal Classification Capabilities for Grid- Connected Wind Farms,” *IEEE Trans. Ind. Appl.*, vol. 59, no. 6, pp. 7328–7340, Nov. 2023, doi: 10.1109/TIA.2023.3302836.

[54] M. N. Uddin, N. Rezaei, and Md. S. Arifin, “Hybrid Machine Learning-based Intelligent Distance Protection and Control Schemes with Fault and Zonal Classification Capabilities for Grid-connected Wind Farms,” in *2022 IEEE Industry Applications Society Annual Meeting (IAS)*, Oct. 2022, pp. 1–8. doi: 10.1109/IAS54023.2022.9939852.

[55] C. E. R. Government of Canada, “CER – Canada Energy Regulator.” Accessed: Nov. 08, 2024. [Online]. Available: https://www.cer-rec.gc.ca/en/index.html

[56] R. Zhu, Z. Chen, X. Wu, and F. Deng, “Virtual Damping Flux-Based LVRT Control for DFIG-Based Wind Turbine,” *IEEE Trans. Energy Convers.*, vol. 30, no. 2, pp. 714–725, Jun. 2015, doi: 10.1109/TEC.2014.2385966.

[57] R. Liu, J. Yao, X. Wang, P. Sun, J. Pei, and J. Hu, “Dynamic Stability Analysis and Improved LVRT Schemes of DFIG-Based Wind Turbines During a Symmetrical Fault in a Weak Grid,” *IEEE Trans. Power Electron.*, vol. 35, no. 1, pp. 303–318, Jan. 2020, doi: 10.1109/TPEL.2019.2911346.

[58] M. Uddin and M. Hafeez, “FLC-Based DTC Scheme to Improve the Dynamic Performance of an IM Drive,” *IEEE Trans. Ind. Appl.*, vol. 48, no. 2, pp. 823–831, Mar. 2012, doi: 10.1109/TIA.2011.2181287.

[59] S. Karad and R. Thakur, “Recent Trends of Control Strategies for Doubly Fed Induction Generator Based Wind Turbine Systems: A Comparative Review,” *Arch. Comput. Methods Eng.*, vol. 28, no. 1, pp. 15–29, Jan. 2021, doi: 10.1007/s11831-019-09367-3.

[60] S. M. A. Cruz, G. D. Marques, P. F. C. Gonçalves, and M. F. Iacchetti, “Predictive Torque and Rotor Flux Control of a DFIG-DC System for Torque Ripple Compensation and Loss Minimization,” *IEEE Trans. Ind. Electron.*, vol. 65, no. 12, pp. 9301–9310, Dec. 2018, doi: 10.1109/TIE.2018.2818667.

[61] W. Ding, J. Li, and J. Yuan, "An Improved Model Predictive Torque Control for Switched Reluctance Motors With Candidate Voltage Vectors Optimization," *IEEE Trans. Ind. Electron.*, vol. 70, no. 5, pp. 4595–4607, May 2023, doi: 10.1109/TIE.2022.3190895.

[62] S. G. Petkar and V. K. Thippiripati, "A Novel Duty-Controlled DTC of a Surface PMSM Drive With Reduced Torque and Flux Ripples," *IEEE Trans. Ind. Electron.*, vol. 70, no. 4, pp. 3373–3383, Apr. 2023, doi: 10.1109/TIE.2022.3181405.

[63] B. D. Lemma and S. Pradabane, "Control of PMSM Drive Using Lookup Table Based Compensated Duty Ratio Optimized Direct Torque Control (DTC)," *IEEE Access*, vol. 11, pp. 19863–19875, 2023, doi: 10.1109/ACCESS.2023.3249111.

[64] B. Shao *et al.*, "Torque Ripple Reduction for Direct Torque Control of Dual Three-Phase PMSM Based on Multiple Virtual Voltage Vectors," *IEEE Trans. Energy Convers.*, vol. 38, no. 1, pp. 296–309, Mar. 2023, doi: 10.1109/TEC.2022.3208784.

[65] W. Deng, J. Tang, and W. Cheng, "An Enhanced Rotating Vector-Based Direct Torque Control for Matrix Converter-Fed PMSM Drives Using Virtual Pulsating Vectors," *CPSS Trans. Power Electron. Appl.*, vol. 8, no. 1, pp. 65–73, Mar. 2023, doi: 10.24295/CPSSTPEA.2023.00007.

[66] P. C. Mavila and R. P. P., "A Virtual Vector Based DTC Scheme With Enhanced Resolution for Dual Inverter Fed Five-Phase IM Drives," *IEEE J. Emerg. Sel. Top. Ind. Electron.*, vol. 4, no. 2, pp. 669–677, Apr. 2023, doi: 10.1109/JESTIE.2022.3215761.

[67] A. K. Peter, J. Mathew, and K. Gopakumar, "A Simplified DTC-SVPWM Scheme for Induction Motor Drives Using a Single PI Controller," *IEEE Trans. Power Electron.*, vol. 38, no. 1, pp. 750–761, Jan. 2023, doi: 10.1109/TPEL.2022.3197362.

[68] W. Wang, C. Liu, H. Zhao, and Z. Song, "Improved Deadbeat-Direct Torque and Flux Control for PMSM With Less Computation and Enhanced Robustness," *IEEE Trans. Ind. Electron.*, vol. 70, no. 3, pp. 2254–2263, Mar. 2023, doi: 10.1109/TIE.2022.3170619.

[69] W. Deng, X. Zhang, and W. Xie, "A Novel Direct Torque Control Strategy of Two-Level Voltage Source Inverters for Eliminating Common-Mode Voltage Spikes Caused by Dead-Time Effect," *IEEE Trans. Power Electron.*, vol. 38, no. 2, pp. 2275–2284, Feb. 2023, doi: 10.1109/TPEL.2022.3209208.

[70] Y. Zhang, S. Zhang, T. Jiang, J. Jiao, and W. Xu, “A Modified Model-Free Predictive Current Control Method Based on an Extended Finite Control Set for DFIGs Applied to a Nonideal Grid,” *IEEE Trans. Ind. Appl.*, vol. 58, no. 2, pp. 2527–2536, Mar. 2022, doi: 10.1109/TIA.2021.3137759.

[71] S. Yan, J. Chen, M. Wang, Y. Yang, and J. M. Rodriguez, “A Survey on Model Predictive Control of DFIGs in Wind Energy Conversion Systems,” *CSEE J. Power Energy Syst.*, vol. 10, no. 3, pp. 1085–1104, May 2024, doi: 10.17775/CSEEJPES.2022.08500.

[72] Z. Rafiee, R. Heydari, M. Rafiee, M. R. Aghamohammadi, J. Rodriguez, and F. Blaabjerg, “Adaptive Model Predictive Control of DFIG-based Wind Farm: A Model-Free Control Approach,” in *2020 IEEE 21st Workshop on Control and Modeling for Power Electronics (COMPEL)*, Nov. 2020, pp. 1–6. doi: 10.1109/COMPEL49091.2020.9265865.

[73] J. Dentler, “Real-time model predictive control of cooperative aerial manipulation,” Ph.D dissertation, University of Luxembourg, Luxembourg, 2018.

[74] Md. S. Arifin and M. N. Uddin, “A Novel Intelligent Power Control Technique for a Type-3 Wind Energy Conversion System with LVRT Capability and Improved Dynamic Performance,” in *2023 IEEE International Conference on Energy Technologies for Future Grids (ETFG)*, Dec. 2023, pp. 1–6. doi: 10.1109/ETFG55873.2023.10408306.

[75] Md. S. Arifin and M. N. Uddin, “A Novel Intelligent Power Control Technique for a Type-3 Wind Energy Conversion System with LVRT Capability and Improved Dynamic Performance,” *IEEE Trans. Ind. Appl.*, pp. 1–14, 2024, doi: 10.1109/TIA.2024.3476461.

[76] Md. S. Arifin and M. N. Uddin, “Dynamic Stability Analysis of a Simplified Neuro-Fuzzy Direct Torque Control Scheme for a Grid-Connected DFIG-WECS with Improved Performance and Reduced Computation,” in *2023 IEEE Industry Applications Society Annual Meeting (IAS)*, USA.

[77] Md. S. Arifin and M. N. Uddin, “Dynamic Stability Analysis of a Simplified Neuro-Fuzzy Direct Torque Control Scheme for a Grid-Connected DFIG-WECS with Improved Performance and Reduced Computation,” *IEEE Trans. Ind. Appl.*, pp. 1–14, 2024, doi: 10.1109/TIA.2024.3444747.

[78] Md. S. Arifin, M. N. Uddin, I. A. Yeo, and N. Rezaei, “A Neuro-Fuzzy Based Power Control of a Type-3 based Wind Energy Conversion Systems with LVRT Capability,” in *2023 IEEE Industry Applications Society Annual Meeting (IAS)*, Oct. 2023, pp. 1–8. doi: 10.1109/IAS54024.2023.10406580.

[79] V. Naik N. and S. P. Singh, “A Novel Interval Type-2 Fuzzy-Based Direct Torque Control of Induction Motor Drive Using Five-Level Diode-Clamped Inverter,” *IEEE Trans. Ind. Electron.*, vol. 68, no. 1, pp. 149–159, Jan. 2021, doi: 10.1109/TIE.2019.2960738.

[80] D. J. S. Oncoy, R. Cardim, M. C. M. Teixeira, F. A. Faria, E. Assunção, and A. Z. N. Lazarini, “New Stabilization Conditions for Fuzzy-Based Sampled-Data Control Systems Using a Fuzzy Lyapunov Functional,” *IEEE Access*, vol. 11, pp. 15390–15403, 2023, doi: 10.1109/ACCESS.2023.3245026.

[81] F. Aymen, N. Mohamed, S. Chayma, C. H. R. Reddy, M. M. Alharthi, and S. S. M. Ghoneim, “An Improved Direct Torque Control Topology of a Double Stator Machine Using the Fuzzy Logic Controller,” *IEEE Access*, vol. 9, pp. 126400–126413, 2021, doi: 10.1109/ACCESS.2021.3110477.

[82] D. Cui and Z. Xiang, “Nonsingular Fixed-Time Fault-Tolerant Fuzzy Control for Switched Uncertain Nonlinear Systems,” *IEEE Trans. Fuzzy Syst.*, vol. 31, no. 1, pp. 174–183, Jan. 2023, doi: 10.1109/TFUZZ.2022.3184048.

[83] W. Ji, J. Qiu, S.-F. Su, and H. Zhang, “Fuzzy Observer-Based Output Feedback Control of Continuous-Time Nonlinear Two-Dimensional Systems,” *IEEE Trans. Fuzzy Syst.*, vol. 31, no. 4, pp. 1391–1400, Apr. 2023, doi: 10.1109/TFUZZ.2022.3201282.

[84] Y. Tan, X. Su, Z. Bing, X. Yang, and A. Knoll, “Reduced Model-Based Fault Detector and Controller Design for Discrete-Time Switching Fuzzy Systems,” *IEEE Trans. Fuzzy Syst.*, vol. 31, no. 2, pp. 669–681, Feb. 2023, doi: 10.1109/TFUZZ.2022.3187195.

[85] S. Puchalapalli and B. Singh, “A Single Input Variable FLC for DFIG-Based WPGS in Standalone Mode,” *IEEE Trans. Sustain. Energy*, vol. 11, no. 2, pp. 595–607, Apr. 2020, doi: 10.1109/TSTE.2019.2898115.

[86] H. Badihi, Y. Zhang, and H. Hong, “A review on application of monitoring, diagnosis, and fault-tolerant control to wind turbines,” in *2013 Conference on Control and Fault-Tolerant Systems (SysTol)*, Oct. 2013, pp. 365–370. doi: 10.1109/SysTol.2013.6693883.

[87] A. Justin and S. Reshma, “Fault tolerant control of wind energy conversion system — Fuzzy approach,” in *2013 Fourth International Conference on Computing, Communications and Networking Technologies (ICCCNT)*, Jul. 2013, pp. 1–6. doi: 10.1109/ICCCNT.2013.6726761.

[88] J.-S. Lee and K.-B. Lee, “Fault tolerance control for outer switches of a 3-level rectifier in wind turbine systems,” in *2015 IEEE Applied Power Electronics Conference and Exposition (APEC)*, Mar. 2015, pp. 1318–1323. doi: 10.1109/APEC.2015.7104518.

[89] P. F. C. Gonçalves, S. M. A. Cruz, and A. M. S. Mendes, “Fault- Tolerant Predictive Control of a Doubly-Fed Induction Generator with Minimal Hardware Requirements,” in *IECON 2018 - 44th Annual Conference of the IEEE Industrial Electronics Society*, Oct. 2018, pp. 3357–3362. doi: 10.1109/IECON.2018.8592825.

[90] G. Chen and X. Cai, “Reconfigurable Control for Fault-Tolerant of Parallel Converters in PMSG Wind Energy Conversion System,” *IEEE Trans. Sustain. Energy*, vol. 10, no. 2, pp. 604–614, Apr. 2019, doi: 10.1109/TSTE.2018.2841018.

[91] N. M. A. Freire and A. J. M. Cardoso, “A Fault-Tolerant PMSG Drive for Wind Turbine Applications With Minimal Increase of the Hardware Requirements,” *IEEE Trans. Ind. Appl.*, vol. 50, no. 3, pp. 2039–2049, May 2014, doi: 10.1109/TIA.2013.2282935.

[92] L. Zhu, Y. Li, A. Chen, W. Cheng, Y. Wang, and S. Ademi, “Research on Direct Power Control for Open-Winding Brushless Doubly-Fed Reluctance Wind Power Generator with Fault-Tolerant Strategy,” in *2019 22nd International Conference on Electrical Machines and Systems (ICEMS)*, Aug. 2019, pp. 1–5. doi: 10.1109/ICEMS.2019.8922192.

[93] T. Jain, J. J. Yamé, and D. Sauter, “A Novel Approach to Real-Time Fault Accommodation in NREL’s 5-MW Wind Turbine Systems,” *IEEE Trans. Sustain. Energy*, vol. 4, no. 4, pp. 1082–1090, Oct. 2013, doi: 10.1109/TSTE.2013.2268615.

[94] X. Feng and R. Patton, “Active fault tolerant control of a wind turbine via T-S fuzzy model predictive control,” in *22nd Mediterranean Conference on Control and Automation*, Jun. 2014, pp. 446–451. doi: 10.1109/MED.2014.6961413.

[95] A. O. Simon, M. Guisser, E. Abdelmounim, M. Aboulfatah, H. Bahri, and L. Azeddine, “Multiple Current Sensor Fault Tolerant Control of DFIG Wind Turbine,” in *2019 International Conference on Wireless Technologies, Embedded and Intelligent Systems (WITS)*, Apr. 2019, pp. 1–7. doi: 10.1109/WITS.2019.8723836.

[96] H. Badihi, Y. Zhang, and H. Hong, “Wind Turbine Fault Diagnosis and Fault-Tolerant Torque Load Control Against Actuator Faults,” *IEEE Trans. Control Syst. Technol.*, vol. 23, no. 4, pp. 1351–1372, Jul. 2015, doi: 10.1109/TCST.2014.2364956.

[97] V. Lešić, M. Vašak, N. Perić, G. Joksimović, and T. M. Wolbank, “Optimal flux magnitude tracking with application to fault-tolerant control of wind turbine generators,” in *2013 European Control Conference (ECC)*, Jul. 2013, pp. 466–471. doi: 10.23919/ECC.2013.6669749.

[98] N. Layadi *et al.*, “Interval type-2 fuzzy adaptive strategy for fault tolerant control based on new faulty model design: Application to DSIM under broken rotor bars fault,” *AMSE J. Model. Meas. Control A*, vol. 91, no. 4, pp. 212–221, 2018.

[99] N. Layadi, S. Zeghlache, A. D. H. Mekki, and F. Berrabah, “Adaptive RBFNN Strategy for Fault Tolerant Control: Application to DSIM under Broken Rotor Bars Fault,” *IJ Intell. Syst. Appl.*, vol. 2, pp. 49–61, 2019.

[100] N. Layadi *et al.*, “Backstepping Fault Tolerant Control for Double Star Induction Machine under Broken Rotor Bars,” *Majlesi J. Electr. Eng.*, vol. 13, no. 3, pp. 59–68, 2019.

[101] I. K. Amin, “Robust control techniques for DFIG driven WECS with improved efficiency,” PhD dissertation, Department of Electrical and computer Engineering, Lakehead University, Thunder Bay, ON, Canada, 2019.

[102] G. Abad, J. Lopez, M. Rodriguez, L. Marroyo, and G. Iwanski, *Doubly fed induction machine: modeling and control for wind energy generation*. John Wiley & Sons, 2011.

[103] B. Wu, Y. Lang, N. Zargari, and S. Kouro, *Power Conversion and Control of Wind Energy Systems*. John Wiley & Sons, 2011.

[104] P. C. Krause, “Analysis of Electric Machinery and Drive Systems,” *IEEE Press Google Sch.*, vol. 2, pp. 203–210, 2002.

[105] M. Kesraoui, N. Korichi, and A. Belkadi, “Maximum power point tracker of wind energy conversion system,” *Renew. Energy*, vol. 36, no. 10, pp. 2655–2662, Oct. 2011, doi: 10.1016/j.renene.2010.04.028.

[106] Y. H. Tabrizi, “Artificial intelligence-based control schemes for robust and sustainable wind energy conversion system,” PhD dissertation, Department of Electrical and computer Engineering, Lakehead University, Thunder Bay, ON, Canada, 2014.

[107] M. Rostami, S. M. Madani, and S. Ademi, “Sensorless Closed-Loop Voltage and Frequency Control of Stand-Alone DFIGs Introducing Direct Flux-Vector Control,” *IEEE Trans. Ind. Electron.*, vol. 67, no. 7, pp. 6078–6088, Jul. 2020, doi: 10.1109/TIE.2019.2955421.

[108] L. H. Hansen *et al.*, “Conceptual survey of generators and power electronics for wind turbines,” 2001.

[109] P. C. Krause and C. H. Thomas, “Simulation of Symmetrical Induction Machinery,” *IEEE Trans. Power Appar. Syst.*, vol. 84, no. 11, pp. 1038–1053, Nov. 1965, doi: 10.1109/TPAS.1965.4766135.

[110] B. Wu and M. Narimani, *High-power converters and AC drives*. John Wiley & Sons, 2017.

[111] C. I. Hubert, *Electric machines*. Prentice Hall, 1990.

[112] M. Mahmud and W. Wang, “An Adaptive EMD Technique for Induction Motor Fault Detection,” *J. Signal Inf. Process.*, vol. 10, no. 4, Art. no. 4, Nov. 2019, doi: 10.4236/jsip.2019.104008.

[113] S. Nandi, H. A. Toliyat, and X. Li, “Condition Monitoring and Fault Diagnosis of Electrical Motors—A Review,” *IEEE Trans. Energy Convers.*, vol. 20, no. 4, pp. 719–729, Dec. 2005, doi: 10.1109/TEC.2005.847955.

[114] Retrieved from the website: https://www.doble.com/wp-content/uploads/induction-motor-rotor-cut-sheet-4.jpg

[115] Y. Xu *et al.*, “Autocorrelated Envelopes for early fault detection of rolling bearings,” *Mech. Syst. Signal Process.*, vol. 146, p. 106990, Jan. 2021, doi: 10.1016/j.ymssp.2020.106990.

[116] J. G. Proakis, *Digital signal processing: principles, algorithms, and applications, 4/E*. Pearson Education India, 2007.

[117] D. Z. Li and W. Wang, “An enhanced GA technique for system training and prognostics,” *Adv. Eng. Softw.*, vol. 42, no. 7, pp. 452–462, Jul. 2011, doi: 10.1016/j.advengsoft.2011.03.014.

[118] M. Zhang, X. Xing, and W. Wang, “Smart Sensor-Based Monitoring Technology for Machinery Fault Detection,” *Sensors*, vol. 24, no. 8, Art. no. 8, Jan. 2024, doi: 10.3390/s24082470.

[119] N. S. Nise, *Control Systems Engineering*. John Wiley & Sons, 2020.

[120] H. Du, M. Li, Y. Xu, and C. Zhou, “An Ensemble Learning Approach for Land Use/Land Cover Classification of Arid Regions for Climate Simulation: A Case Study of Xinjiang, Northwest China,” *IEEE J. Sel. Top. Appl. Earth Obs. Remote Sens.*, vol. 16, pp. 2413–2426, 2023, doi: 10.1109/JSTARS.2023.3247624.

[121] S. Yadav and S. Shukla, “Analysis of k-Fold Cross-Validation over Hold-Out Validation on Colossal Datasets for Quality Classification,” in *2016 IEEE 6th International Conference on Advanced Computing (IACC)*, Feb. 2016, pp. 78–83. doi: 10.1109/IACC.2016.25.

[122] M. M. Abdulghani and K. M. Al-Aubidy, “Design and evaluation of a MIMO ANFIS using MATLAB and V-REP,” in *Proceedings of the 11th International Conference on Advances in Computing, Control, and Telecommunication Technologies, ACT*, 2020.

[123] P. M. Anderson and A. Bose, “Stability Simulation of Wind Turbine Systems,” *IEEE Trans. Power Appar. Syst.*, vol. PAS-102, no. 12, pp. 3791–3795, Dec. 1983, doi: 10.1109/TPAS.1983.317873.

[124] H. K. Khalil, *Control of Nonlinear Systems*. Prentice Hall, New York, NY.

This page is intentionally left blank.